A First Principles Study of Radiation Defects in Semiconductors

Submitted by Byron James Fraser Coomer to the University of Exeter as a thesis for the degree of Doctor of Philosophy in Physics, November 2000.

I certify that all material in this thesis which is not my own work has been identified and that no material is included for which a degree has previously been conferred upon me.

Abstract

Presented in this thesis are the results of computational investigations into radiation defects in silicon, germanium and diamond. The calculations were performed principally using local density functional theory as implemented by the AIMPRO (*Ab Initio* Modelling PROgram) code.

The two most fundamental point defects which occur in crystals – the vacancy and the self-interstitial – are investigated within this thesis. The extraction of an atom from its crystal lattice site results in a vacancy. This defect has been thoroughly investigated in both silicon and diamond. In this thesis we consider the germanium vacancy and its interaction with hydrogen. The addition of an extra atom into a crystal results in an interstitial. If the additional atom is the same as the host crystal atoms then this is called a self-interstitial. This defect and its aggregates are less well understood than the vacancy. We consider self-interstitials defects in the silicon and diamond systems.

Acknowledgements

I would like to thank the School of Physics at Exeter University and EPSRC for providing funding and resources for the duration of my PhD.

Many thanks to Bob Jones without whose help I suspect I wouldn't have made it. Also special thanks to all the members of the AIMPRO group - Jon, Ben, Chris, Caspar, Marcus, Antonio, Sven, Malc, Patrick, Jose, and Stefan. I would like to acknowledge the helpful discussions and communications which I have had with people outside the AIMPRO group, amongst others, Gordon Davies, Stefan Estreicher, Jorg Weber, Daniel Twitchen and Brian-Bech Nielsen.

Also big thanks to all the family, Rosie especially. Finally, I thank Niss, Jess and most of all, Lorraine.

Publications list

1. *Identification of the tetra-interstitial in silicon*, B. J. Coomer, J. P. Goss, R. Jones, S. Öberg, P. R. Briddon, submitted to Solid State Phenomenon.
2. *Self-interstitial aggregation in diamond*, J. P. Goss, B. J. Coomer, R. Jones, S. Öberg, P. R. Briddon, submitted to Physical Review B.
3. *Vacancy-hydrogen complexes in germanium*, B. J. Coomer, P. Leary, M. Budde, B. B. Nielsen, R. Jones, S. Öberg, P. R. Briddon, Materials science and engineering B – Solid-state materials for advanced technology, 1999, Vol.58, No.1-2, pp.36-38.
4. *Interstitial aggregates and a new model for the W-optical center in silicon*, B. J. Coomer, J. P. Goss, R. Jones, S. Öberg, P. R. Briddon, Physica B, **274** 505 (1999).
5. *The divacancy in silicon and diamond*, B. J. Coomer, A. Resende, J. P. Goss, R. Jones, S. Öberg, P. R. Briddon, Physica B, **274** 520 (1999).
6. *The interaction of hydrogen with deep level defects in silicon*, R. Jones, B. J. Coomer, J. P. Goss, B. Hourahine, A. Resende, Solid State Phenomena, **71** 173 (2000).
7. *Small Aggregates of Interstitials and Models for Platelets in Diamond*, J. P. Goss, B. J. Coomer, R. Jones, C. J. Fall, C. D. Latham, P. R. Briddon and S. Öberg To appear in J. Phys.: Cond. Matter (2000).

Others

1. *Models for platelets in diamond* J. P. Goss, R. Jones, B. J. Coomer, C. J. Fall and C. D. Latham , The 51st Diamond conference proceedings, 2000.
2. *Optical Properties of interstitials in diamond* J. P. Goss, R. Jones, B. J. Coomer, P. R. Briddon, The 51st Diamond conference proceedings, 2000.

3. *The tetra-interstitial in silicon*, B. J. Coomer, N. Pinho, J. P. Goss, R. Jones, S. Öberg, P. R. Briddon, ENDEASD conference proceedings, 2000.
4. *The di and tri-interstitial in silicon*, N. Pinho, B. J. Coomer, J. P. Goss, R. Jones, S. Öberg, P. R. Briddon, ENDEASD conference proceedings, 2000.
5. *Interstitial aggregation in diamond*, B. J. Coomer, J. P. Goss, R. Jones, S. Öberg, P. R. Briddon, Diamond conference proceedings, 1999.
6. *Ab-initio calculations of interstitial aggregates in silicon*, B. J. Coomer, A. Resende, J. P. Goss, R. Jones, S. Öberg, P. R. Briddon, ENDEASD conference proceedings, 1999.
7. *The divacancy in diamond*, B. J. Coomer, A. Resende, J. P. Goss, R. Jones, S. Öberg, P. R. Briddon, Diamond conference proceedings, 1998.
8. *Substitutional gold in germanium*, B. J. Coomer, R. Jones, S. Öberg, P. R. Briddon, HPCI conference proceedings, 1997.

Presentations

1. *Platelets in diamond*, The 51th Diamond Conference, Queens College, Cambridge, 7/00.
2. *The tetra-interstitial in silicon*, ENDEASD workshop, Stockholm, Sweden 6/00.
3. *A Pedestrian approach to quantum mechanics*, ENDEASD summerschool, Stockholm, Sweden 6/00.
4. *Interstitials in diamond*, The 50th Diamond Conference, St. Margarets College, Oxford, 7/99.
5. *The W-line in silicon*, ICDS conference, Berkeley, California, 7/99.
6. *The single- and di-interstitial in diamond*, Diamond Workshop, Kings College, Oxford, 6/99.
7. *Divacancy-hydrogen complexes in silicon*, Hydrogen '99, University of Exeter, 4/99.
8. *Contrasting distortions of the divacancies in silicon and diamond*, Institute of Physics CMMP conference, Manchester, 12/98.

9. *Divacancy defects in semiconductors*, Postgraduate Talks, University of Exeter, 9/98.
10. *The divacancy in diamond*, The 49^{th} Diamond Conference, Royal Holloway, 7/98.
11. *Vacancy-hydrogen complexes in germanium*, E-MRS conference, Strasbourg, 6/98.
12. *Substitutional gold in germanium*, HPCI conference, Manchester, 2/98.

Contents

1 Introduction **25**

1.1 Summary of thesis . . . 27

2 Background theory **29**

2.1 Introduction . . . 29

2.2 Initial steps . . . 30

2.2.1 The Born-Oppenheimer approximation . . . 30

2.3 Density functional theory . . . 32

2.3.1 The variational principle . . . 33

2.3.2 The kinetic energy . . . 33

2.3.3 The exchange-correlation energy . . . 34

2.3.4 The Kohn-Sham equations . . . 35

2.3.5 Pseudopotential theory . . . 35

2.4 AIMPRO methodology . . . 38

2.4.1 Expansion of the wavefunction . . . 38

2.4.2 Hartree term . . . 39

2.4.3 The exchange-correlation term . . . 40

2.5 Supercell AIMPRO . . . 47

2.5.1 The supercell approach . . . 47

2.5.2 Supercell methodology . . . 47

2.5.3 Sampling of the Brillouin zone . . . 49

2.5.4 Summary . . . 49

3 Experiment **51**

3.1 Introduction . . . 51

3.2 Electron paramagnetic resonance . . . 51

3.2.1 Introduction 51

3.2.2 Hyperfine interaction 54

3.2.3 The nuclear Zeeman interaction 55

3.2.4 The D-tensor 55

3.2.5 Symmetry assigments 55

3.2.6 Auxiliary techniques 57

3.3 Photoluminescence and absorption 59

3.4 Deep level transient spectroscopy 62

3.5 Local vibrational mode spectroscopy 66

4 Determination of experimental observables 69

4.1 Introduction 69

4.2 Experimental background 69

4.3 Calculations 71

4.4 Structure 71

4.5 Vibrational modes 71

4.6 Migration paths and diffusion barriers 74

4.6.1 Methods 74

4.6.2 Diffusion of C_i 75

4.7 Stress response 75

4.8 Electronic structure 77

4.8.1 Calculation of electrical levels 79

4.9 Summary 81

5 Vacancy-hydrogen defects in germanium 83

5.1 Introduction 83

5.2 Calculation method 85

5.3 Results 86

5.3.1 Structures 86

5.3.2 Vibrational properties 87

5.3.3 Electronic character 87

5.4 Conclusions 91

6 The single interstitial in silicon 93

6.1 Introduction 93

6.2 Background 94
6.3 Method 95
6.4 Results 96
6.5 Conclusions 101

7 The di-interstitial in silicon 105
7.1 Introduction 105
7.2 Background 106
7.3 Method 110
7.4 Results 110
7.5 Conclusions 115

8 The tri-interstitial 117
8.1 Introduction 117
8.2 Background 117
8.3 Method 123
8.4 Results 123
8.5 Conclusions 131

9 The tetra-interstitial in silicon 133
9.1 Introduction 133
9.2 Background 133
9.3 Method 135
9.4 Results 136
9.5 Discussion 137
9.6 Conclusion 142

10 Self-interstitial aggregation in diamond 143
10.1 Introduction 143
10.2 Background 144
10.3 Method 148
10.4 Results 149
    10.4.1 I_1 149
    10.4.2 I_2 149
    10.4.3 I_3 152

10.4.4 I_4 . . . 153
10.4.5 Trends . . . 153
10.4.6 Platelets . . . 156
10.4.7 Conclusions . . . 156

11 Conclusions 159

List of Tables

1.1 Properties of elemental semiconductors. 25

3.1 Point groups of octahedral symmetry listed alongside their corresponding symmetry group. For each point group, the operations are listed. 57

4.1 Bondlengths (Å) of C_i evaluated using cluster and supercell approaches. Also shown for the neutral charge state are the results of *ab initio* calculations of Capaz *et al* [1]. C denotes cluster calculations and S denotes supercell. 72

4.2 LVMs (cm^{-1}) of C_i in silicon calculated using the supercell and cluster method compared with experiment. The isotopic shifts of the LVMs with ^{13}C and ^{14}C are also shown. 73

4.3 Theoretical values (eV) for the activation barrier to diffusion of neutral C_i along two migration paths, labelled 1 and 2 (see Fig. 4.2). 76

4.4 Calculated and experimentally determined B-tensor elements (eV) of the carbon interstitial. 77

4.5 Electrical levels of substitutional gold and the carbon interstitial. The calculated C_i levels are also shown. 81

5.1 Calculated (quasi-harmonic) stretch frequencies and observed (in brackets) $(cm^{-1})^a$ of VH_n defects in germanium. Assignments of experimental absorption lines to VH_2D, VHD_2 are tentative. s, total symmetric; a, total non-symmetric, -IR, infra red inactive. 88

6.1 Energies (eV) relative to the ground state of various charge states of the self-interstitial in silicon as calculated by AIMPRO [2]. The results of Mainwood *et al* [3] are shown in brackets for comparison. 94

6.2 Bondlengths (Å) of the neutral ⟨110⟩ interstitial. Bond labels are those given in Fig. 6.4. 96

7.1 Summary of EPR centres which have been attributed to self-interstitial clusters. 106

7.2 Tabulation of g-values determined from the P6 spectrum in silicon taken from Ref. [4]. The angle, θ and principal axis direction are shown in Fig. 7.1.107

7.3 Calculated electrical levels for I_2 defects, I–III. 112

7.4 Bond lengths of I_2 defects. The bond labels $a - g$ (Å) are explained in Fig. 7.3. 114

7.5 Energies (eV) relative to the lowest energy defect of the charge states of the di-interstitial models in silicon I-III calculated using AIMPRO cluster code. 115

8.1 Distances (Å) between atoms surrounding the divacancy for the relaxed D_{3d} and C_{2h} structures in silicon and diamond. Distances are given with reference to Fig. 8.1. 120

8.2 Calculated bondlengths of I_3 (I) showing convergence of the structure with system size and method employed. Bondlengths are given with reference to Fig. 8.5. For the largest cluster, variation of the bondlengths from the ideal Si–Si bondlength (2.35 Å) are given 127

8.3 Isotopic behaviour of vibrational modes of I_3 in silicon calculated using cluster and supercell method. In each case the vibrational modes frequencies (cm^{-1}) are indicated when (i) all atoms are ^{28}Si and (ii) atom b (Fig. 8.5) is replaced by ^{30}Si. The localisation of each mode on atom a is given in braces. 128

8.4 Energies (eV) relative to the lowest energy defect of the charge states of the tri-interstitial models in silicon I-IV calculated using AIMPRO cluster and supercell codes. 131

9.1 Tabulation of g-values determined from the B3 spectrum in silicon. 134

9.2 Calculated bondlengths of I_4 in three cluster sizes compared with Si$_{196}$ supercell [5] results. Bondlengths l_{1-4} are given with reference to Fig. 9.1. For the largest cluster used the deviation from the ideal Si–Si bondlength (2.35 Å) is given. 136

9.3 Calculated ionisation energies of $\mathrm{C_i}$ and I_4 in clusters of different size. The values in brackets are the donor level positions resulting from each calculation. 137

9.4 Calculated vibrational modes and symmetries for I_4 in silicon. The localisation of the vibrational mode is estimated by calculating the total amplitude squared of the mode on the 14 core atoms as a percentage of the sum of the squares of all the atomic vibrational amplitudes in the cluster. 139

10.1 Total energies (eV) of di-interstitial defects calculated using the cluster code. 150

10.2 Structural and energetical parameters for self-interstitial aggregates in diamond calculated using the supercell method. Bondlengths are given in Å and energies in eV. 154

10.3 The calculated and experimental principal values (GHz), in descending order, and principal directions, $[n_1 n_2 n_3]$, for the spin–spin tensor, D. In each case n_3 is almost parallel to the vector joining the radicals. 154

List of Figures

3.1 Energy level splittings and corresponding EPR signal (below) for a defect with $s = 1/2$. Splitting due to the electronic Zeeman effect and the Hyperfine interaction are indicated. 54

3.2 Characteristic angular dependencies of absorption for the eight symmetry groups distinguishable by EPR. 56

3.3 Mechanism for low-temperature luminescence and absorption. (a) Photoluminescence: Electrons are excited from the ground state into the conduction band where they rapidly relax non-radiatively through the continuum states and defect excited states before photon assisted electron-hole recombination occurs. (b) Absorption: Photon absorption occurs when the photon energy matches the transition energy for excitation. 60

3.4 Configurational coordinate diagram showing absorption and luminescence processes. 61

3.5 Steady state distribution of filled and empty traps in a $p^+ - n$ junction under zero bias (top) and reverse bias $V > V_{junc}$ (bottom). W represents the depletion region and λ is the transition region. 63

3.6 The temperature dependence of the capacitance transient for a given rate window. 65

4.1 Structure of the carbon interstitial in silicon. The lengths of the labelled bonds are given in Table 4.1. 70

4.2 Possible migration paths of C_i. Path 1 has a saddle point for diffusion at the bond-centred site. The saddle point for path 2 has C_2 symmetry. . . . 76

4.3 Total energy differences of the $\mathrm{C_i}$ defect in the supercell for various values of the lattice parameter, a_0. 77

4.4 Directions of B-tensor elements of the carbon interstitial in silicon. 78

4.5 Kohn-Sham levels of the carbon interstitial in silicon. Left: eigenspectrum of a pure 131 atom cluster. Right: spin up and down eigenspectra of the carbon interstitial in three charge states. The valence band edges have been aligned. The highest occupied and lowest unoccupied levels are indicated by filled circles and empty squares respectively. 78

4.6 Isosurface plot of the unpaired wavefunction of C_i^+ (left) and C_i^- (right). . 79

5.1 Vacancy-hydrogen structures in germanium. Reconstructed bonds are indicated by the dashed lines. 85

5.2 Isosurface plots of the gap states of the D_{2d} vacancy in germanium. Positive and negative lobes are coloured red and green. The vacant site is indicated by the ghost atom.Plots (a) and (b) show the two orbitals comprising the e-doublet. Plot (c) is the isosurface of the b_2 orbital. 89

5.3 Splitting of the vacancy t_2 level under the Jahn-teller distortion from T_d to D_{2d} symmetry. The filled and open circles represent the electronic and hole filling respectively of the gap states. 89

5.4 Kohn-Sham eigenvalues of the isolated neutral vacancy and VH complexes in germanium. The bandgap has been scaled to the experimental value. The highest occupied levels are indicated by the filled circles. Doublet levels in the gap are shown by thick lines. 91

5.5 Isosurface plot of the highest occupied orbital of VH_3. 92

6.1 Possible configurations of the isolated self-interstitial in silicon. In each case the atoms lying close to their lattice sites are shaded light grey. (a) ⟨001⟩ split-interstitial. (b) ⟨110⟩ split-interstitial. (c) Tetrahedral interstitial. (d) Hexagonal interstitial. 94

6.2 Charge density contour plot of the ⟨110⟩ split-interstitial in silicon. Filled circles denote atoms lying in the plane. (a) The plane containing the split-interstitial pair and one of the five fold coordinated atoms. (b) The defect mirror plane containing the split-interstitial atoms. 97

6.3 KS eigenvalues ⟨110⟩ interstitial in silicon. The bandgap has been rescaled to the experimental value. The electronic occupation of the highest occupied level is indicated by filled circles. Isosurfaces of the labelled states are plotted in Fig. 6.5. 97

6.4 Schematic showing the bonding of the $\langle 110 \rangle$ split-interstitial. Left: The $\langle 110 \rangle$ split-interstitial. The defect can be reduced to three non-equivalent bonds labelled x, y, z. Right: A Si dimer surrounded by four atoms placed at positions corresponding to the split-interstitial defect. The six dangling bonds are orientated to match the split-interstitial as closely as possible. 98

6.5 KS gap state wavefunctions of the neutral $\langle 110 \rangle$ interstitial in silicon. The three isosurfaces (a), (b) and (c) correspond to the KS eigenvalues shown in Fig. 6.3. 100

6.6 Reorientation path of the $\langle 110 \rangle$ interstitial. The two atoms sharing the site are shown in dark grey. (a) The optimised [110] oriented interstitial. (b) Mid-point structure to reorientation (C_{1h} symmetry) (c)The $[10\bar{1}]$ oriented interstitial. 101

6.7 Electronic character of the tetrahedral self-interstitial Left: KS eigenvalue plot of I^0 at the tetrahedral interstitial site. The electronic filling of the gap states is indicated by the filled (electrons) and unfilled (holes) circles. Right: An isosurface plot of the highest occupied wavefunction (t_2 symmetry) is shown to the right. Each lobe represents a positive or negative sign of one of the component wavefunctions. 102

7.1 Principal directions of the g-tensor of the P6 EPR centre. The values of the tensor elements and angles are given in Table 7.2. 107

7.2 Schematics showing the structures of I_2 defects previously proposed. In each case the atoms lying close to their lattice sites are shaded light grey. Left: The original defect structure proposed for P6 [6]. Middle: Modified structure [4]. Right: Defect structure proposed for P6 by Kim *et al* [7]. . . 108

7.3 Schematics showing the structures of I_2 defects investigated. In each case the atoms lying close to their lattice sites are shaded dark gray. 110

7.4 KS eigenvalue plot of di-interstitial defects and defect-free cluster (left) for comparison. The labels, I-III of the defects refers to Fig. 7.3. 111

7.5 Isosurface plots of the highest occupied (Left) and lowest unoccupied (Right) wavefunctions of I_2^+ in the Kim configuration (I). The defect is shown viewed from roughly [010] in the upper figures and from the [001] direction in the lower figures. 112

7.6 Isosurface plot of the highest occupied wavefunction of I_2^0 II. 113

7.7 Isosurface plots of the highest occupied (Left) and lowest unoccupied wavefunction of I_2^0 III. 113

8.1 (a) Schematic of the ideal divacancy in silicon. The atoms are labelled following the notation used by Watkins and Corbett[8]. (b) The structure of the divacancy is summarised with a view down the principal [111] axis. 120

8.2 The effect of a symmetry lowering pairing distortion to C_{2h} on the one-electron levels of the ideal, D_{3d} divacancy. For clarity, circles indicate the orbitals with finite amplitude on the defect mirror plane (a) The D_{3d} structure. (b) The large pairing, distortion to C_{2h} symmetry. A bond is formed between the two atom pairs b, c, and b′, c′ such that the distances $l_{ac} = l_{ab} > l_{bc}$ and $l_{a'c'} = l_{a'b'} > l_{b'c'}$. 121

8.3 Possible mechanisms for optical transitions associated with point defects. 122

8.4 Structures of I_3 defects considered. In each case the atoms lying close to their lattice sites are shaded dark grey. I: Three atoms placed at bond centered positions surrounding a tetrahedral interstitial site (C_{3v} symmetry). II: Three [001] split-interstitial pairs placed at next nearest neighbor positions (C_2 symmetry). III: A substitutional atom replaced by four atoms (T_d symmetry) [9]. IV: Three atoms arranged as an equilateral triangle surrounding a Si–Si bond center (C_{3v} symmetry) [10]. 124

8.5 Schematic showing the structure of I_3 (I). **Left:** A section from the ideal silicon structure. To form I_3, three atoms are placed in bond centred positions indicated by the filled circles. **Right:** The fully optimised structure of I_3. For clarity, the three bond-centred interstitial atoms are shown in bold. 126

8.6 Contour plot of the charge density in a plane containing the three equivalent atoms at the defect core of the open form of I_3. The contours indicate that the bonds are close in character to the ideal Si-Si covalent bond. 126

8.7 KS eigenvalue plots of I_3 defects in silicon. The pure cluster eigenvalues are shown for comparison. The labels I-IV refer to Fig. 8.4 128

8.8 Isosurface plot of unpaired wavefunction of I_3^+ (II). The C_2 axis of the defect points directly out of the page. 129

8.9 Isosurface plot of the highest occupied state of I_3 (III). The state is of e symmetry and the components of the wavefunction calculated by AIMPRO are shown. Negative and positive regions are shown in red and green respectively. 130

9.1 Schematics showing the structure of the tetra-interstitial in silicon. Left: A section of the silicon structure. To form the defect, four next-nearest neighbor atoms (shown in bold) are replaced by [001] orientated atom pairs. Right: The fully optimized structure of I_4 in silicon. For clarity, the four [001] split interstitial pairs which make up the defect are shown in bold. The reconstructed bonds which link the interstitial pairs are shaded. . . 135

9.2 Schematics showing the unpaired wavefunction of I_4^+. Left: A 3-dimensional schematic of an isosurface of the wavefunction. Dark (light) surfaces indicate positive (negative) regions of the wavefunction. Right: Contour plot of the unpaired wavefunction on the $(1\bar{1}0)$ plane. Contours representing positive (negative) regions are shown by solid (dashed) lines. Atoms lying in the plane are shown as black circles. Double circles indicate that two atoms lie equidistant from the plane along $[1\bar{1}0]$ and $[\bar{1}10]$ 138

9.3 The Kohn-Sham electronic levels of the tetra-interstitial in silicon. The levels are shown for the optimised defect in three different (tetrahedral interstitial site centred) clusters: (a) $\mathrm{Si_{88}H_{64}}$ (b) $\mathrm{Si_{188}H_{120}}$ (c) $\mathrm{Si_{290}H_{144}}$. 139

10.1 The optimised structure of the isolated [001] self-interstitial in diamond. . 145

10.2 The optimised structure of the nearest neighbour form of the di-[001] interstitial in diamond. 146

10.3 The optimised structure of the next-nearest neighbour form of the di-[001] interstitial in diamond. 150

10.4 Calculated diffusion mechanism for the [001] orientated di-interstitial in diamond. The defect migrates through interconversion between the nearest neighbour structure, (a) and the next nearest neighbour structure (d) via structures (b) and (c). The two atoms which move the most during the diffusion step shown are shaded dark grey to aid the eye. 151

10.5 Calculated diffusion barrier for the [001] orientated di-interstitial in diamond. $\alpha = 0$ corresponds to Fig. 10.4 (a) and $\alpha = 1.0$ corresponds to Fig. 10.4 (d). 152

10.6 The optimised structure of the of the tri-[001] interstitial in diamond. . . 152

10.7 The optimised structure of the of the tetra-[001] interstitial in diamond. . 153

10.8 (a)–(e) Interstitial aggregates in diamond. NN denotes nearest-neighbour form, $2NN$ denotes next-nearest-neighbor form. Each interstitial center is summarised in two ways. Upper figure : Schematic indicating the positions of the constituent [001]-split-interstitial pairs on a [110] chain of atoms in the diamond lattice (represented by the jagged line). Lower figure: The relaxed structures of each defect. The open circles represent the interstitial atoms shown in the upper figure and the ringed atoms are those which are three-fold coordinated and possess non-bonding orbitals. Reconstructed bonds are shown by dashed lines. 155

10.9 Pure self-interstitial platelet models. Replacing every atom on a {001} plane by a [001] split-interstitial pair (top left), there are a number of ways of producing a fully reconstructed platelet. Five different simple reconstructions are depicted. IN each case the surrounding lattice has been removed for clarity. Each atom is colored depending on whether it lies in the upper or lower plane to aid the eye. 157

Chapter 1

Introduction

This thesis principally contains the results of calculations of intrinsic defects in semiconductors. The calculations are performed using local density-functional theory (DFT), a well established *ab initio* method used for modelling matter at the atomic scale. The *ab initio* label means that no input is required from experiment, in contrast to quantum mechanical, semi-empirical methods which include data such as ionisation energies and electron affinities. The advances in computing performance and optimisation of the implementations of density-functional theory programs means that systems up to around 1000 atoms can now be considered with this method.

The defects are studied in three materials: diamond, silicon, and germanium. These three elemental crystals all share the diamond structure, each atom being tetrahedrally bonded to four neighbours but the lattice constants of the three materials are quite different (see Table 1.1). The different applications of the materials in industrial and scientific fields give rise to distinct motivations to study the defects in each material.

Whilst intrinsic defects are always present to some degree, their abundance can be greatly enhanced during growth. For example, rapidly grown Si crystals tend to have a

	C	Si	Ge
lattice constant at 300K (Å)	3.567	5.431	5.658
density (kg/m^3)	3515.3	2329.0	5323.4
bulk modulus (GPa)	442.3	97.9	77.2
bandgap at 0K (eV)	5.48	1.17	0.74

Table 1.1: Properties of elemental semiconductors.

larger vacancy (V) concentrations than slow-grown ones. Impurity doping or contamination can also alter the V concentration. The binding of the vacancy with group III impurities inhibits vacancy-interstitial(I) annihilation resulting in a higher concentration of V in *p*-type material than in *n*-type. Processing stages such as ion implantation and surface treatments such as etching and contact deposition are also known to increase the abundance of intrinsic defects. Finally, devices employed in radiation environments suffer degradation due to the creation of critical concentrations of V and I. Although the monovacancy and interstitial are initially the more abundant radiation defects, the dominant centre observed in electron irradiated silicon at room temperature is the divacancy (V_2)[11]. Vacancy aggregates $V_{3,4,5}$ have all been assigned to EPR centres and recent theoretical calculations also suggest that V_6 undergoes substantial reconstruction to form a particularly stable defect which is identified with experiment [12].

The importance of understanding radiation defects in silicon is evidently clear. The motivation to study defects in germanium has recently been strengthened by a surge of interest in using bandgap engineering through SiGe technology. The ability to practice bandgap engineering within the silicon material system has long been recognised by semiconductor device designers as being highly desirable. Such techniques combine the superior device properties of III-V hetero-junction bipolar transistors (HBT's) and the processing maturity of Si technology. In the SiGe HBT, Ge is selectively introduced into the base region of the transistor. The smaller base bandgap of SiGe compared to Si enhances electron injection, producing a higher current gain for the same base doping level compared to a Si device. Thus, the base can be doped more heavily in the SiGe HBT in order to lower the total base resistance. At the same time, using the ultra-high vacuum/chemical vapour deposition (UHV/CVD) growth technique allows the Ge content to be controllably graded across the base to introduce a carrier drift-field and thereby improve the transistor frequency response. In short, in terms of both frequency response and circuit delay, a much faster device is obtained using SiGe.

Interest in diamond has also increased substantially in recent years largely because of the development of diamond thin-film technology. The ability to use chemical vapour deposition methods to grow diamond has important implications for industry. Diamond thin films can be used as a coating layer for surfaces, increasing their resistance to abrasion and, because of the large thermal conductivity of diamond, can allow a rapid dissipation of heat. As diamond is a semiconductor, the strength and high thermal conductivity of diamond may also assist the performance of electronic devices. The major obstacle to this kind of application is the difficulty in producing n-type diamond. One other important potential application of diamond is as a particle detector device. The high radiation hardness of diamond gives it an obvious advantage over the currently used silicon detectors which degrade typically over a few months. Clearly this latter application gives strong motivation to understand radiation damage centres in diamond.

1.1 Summary of thesis

The first three chapters of this thesis are dedicated to providing the background knowledge to the theory, implementation of the theory and to the major experimental techniques important to the calculations.

The theory is first applied to the isolated vacancy in germanium and its complexes with hydrogen. This work concentrates on calculation of observable properties of these defects and was carried out with close links with an experimental group. The characteristics of the vacancy, and the hydrogen complexes are found to be very similar to those observed and calculated previously in silicon.

In subsequent chapters, self-interstitial defects in silicon are studied. Despite the obvious fundamental importance of the single self-interstitial in silicon, one peculiarity of semiconductor defect field is that this defect remains unidentified. The single interstitial is considered in this thesis, partially in the light of a recent claim regarding the observation of the defect.

We then begin the study of self-interstitial aggregation. Whilst it is known that self-interstitials can migrate and complex with each-other to form extended defects observed by TEM, little is known about the primary stages to the formation process. The initial stage, the di-self-interstitial defect, is studied and the properties of some alternative structures are reported. The key aim of the calculations is to provide information which facilitates the identification of the defect structures with experiment. The calculations of the di-interstitial defects show that previous conclusions have been erroneous, and new models are considered.

The tri-interstitial is also considered. Again we report the calculated observable quantities with the aim of identifying one of the models with experiment. It is found that one model of the tri-interstitial satisfies much of the data on an optical centre labelled the W-line. This link is explored.

The structural model considered for the tetra-interstitial defect was devised many years ago. The defect is shown to have properties which give very strong evidence that it exists in silicon, and is observed by electron paramagnetic resonance. The evidence is strong enough for identification.

The final chapter considers self-interstitials in diamond. This area has received substantial attention from experimentalists and theorists in past years and we concentrate on the small aggregates and models for the extended self-interstitial related defects.

Chapter 2

Background theory

2.1 Introduction

Two methods currently exist which model the solid state from first principles, using only the atomic numbers and coordinates as input. Their key difference lies with the property which is used as the variational parameter in order to minimize the system energy. In Hartree-Fock (HF) theory, the electronic wavefunctions take on this role whereas density functional theory (DFT) uses the charge density. The advantages of DFT over HF for modelling semiconductor defects arise from its lower computational demands and better scaling and its inclusion of the electron correlation. In HF on the other hand, the wavefunctions are mathematically meaningful as opposed to DFT where the wavefunctions do not necessarily have physical significance. In practice however, the wavefunctions calculated in DFT often bear a strong resemblance to experiment. Hence DFT is highly suited to calculations of defects in semiconductors where system sizes of up to 1000 atoms can be performed routinely.

This chapter is intended to outline both the theoretical background to density functional theory (Sec. 2.3) and implementation details (Sec. 2.4) specific to AIMPRO (Ab Initio Modelling Program). AIMPRO is a self-consistent local density functional code applied to real-space clusters of atoms. The majority of the results discussed in this thesis have been produced using this method. A new version of AIMPRO has been developed which shares many of the implementations of the cluster code but uses a supercell approach. The methods which are unique to the supercell code will be briefly detailed in Sec. 2.5 along with a general discussion of the supercell approach.

Starting from the consideration of the Schrödinger equation (Sec. 2.2), the major building blocks of the method are outlined. This includes detailing the Born-Oppenheimer and local density approximations (Sec. 2.3), and consideration of the Kohn-Sham equations (Sec. 2.3.4) as well as pseudopotential theory (Sec. 2.3.5).

2.2 Initial steps

The problem is to find the solution to the time-independent many-body Schrödinger equation for a set of atoms.

$$\hat{H}\Psi_i = E_i \Psi_i \tag{2.1}$$

where Ψ_i is the wavefunction of the entire system,

$$\Psi_i = \Psi_i(\mathbf{r}_1, \mathbf{r}_2, \mathbf{r}_3, ..., \mathbf{r}_n, \mathbf{R}_1, \mathbf{R}_2, \mathbf{R}_3, ..., \mathbf{R}_n) = \Psi_i(\mathbf{r}, \mathbf{R}) \tag{2.2}$$

$\mathbf{r}$ represents the spatial and spin coordinates of electrons and $\mathbf{R}$ represents the spatial coordinates of the nuclei. E_i is the energy eigenvalue of the i^{th} state and $\hat{H}$ is the Hamiltonian which may be written[1],

$$\begin{aligned}\hat{H} = \frac{1}{2}\Bigg(-\sum_{i=1} \nabla_i^2 - \sum_{\alpha=1} \frac{m}{M_\alpha} \nabla_\alpha^2 + \frac{1}{2} \sum_{i,j \neq i} \frac{1}{|\mathbf{r}_i - \mathbf{r}_j|} - \sum_{i,\alpha} \frac{Z_\alpha}{|\mathbf{r}_i - \mathbf{R}_\alpha|} \\ + \frac{1}{2} \sum_{\alpha,\beta \neq \alpha} \frac{Z_\alpha Z_\beta}{|\mathbf{R}_\alpha - \mathbf{R}_\beta|} \Bigg)\end{aligned} \tag{2.3}$$

or, using obvious notation,

$$\hat{H} = \hat{T}_e + \hat{T}_i + \hat{V}_{e-e} + \hat{V}_{e-i} + \hat{V}_{i-i} \tag{2.4}$$

For all but the simplest of systems this represents an intractable problem. To obtain a solution, the *Born-Oppenheimer*, or adiabatic approximation is included. This step allows the decoupling of the motions of the electrons and nuclei.

2.2.1 The Born-Oppenheimer approximation

The Born-Oppenheimer approximation utilizes the great difference in the electronic and nuclear masses. Since nuclear motion is much slower than electron motion, the electronic

---

[1] using atomic units i.e. $\hbar = e = m_e = 4\pi\epsilon_0 = 1$ so that 1 a.u.= 0.529 Å

wavefunction can be calculated assuming fixed positions of the nuclei, and nuclear motion can be considered under an averaged distribution of electron density.

$$\Psi_{tot} = \chi(\mathbf{R})\Psi(\mathbf{r},\mathbf{R})\,, \tag{2.5}$$

where Ψ satisfies

$$(\hat{T}_e + \hat{V}_{e-e} + \hat{V}_{e-i} + \hat{V}_{i-i})\Psi = E(R)\Psi \tag{2.6}$$

Now $\chi(\mathbf{R})$ is a modulating function associated only with the nuclear positions, $\mathbf{R} = \{\mathbf{R}_1, \mathbf{R}_2, \mathbf{R}_3, ..., \mathbf{R}_N\}$ and $\Psi(\mathbf{r},\mathbf{R})$ is the solution to the Schrödinger equation. Substituting Eq. 2.5 into the Schrödinger equation, multiplying through by $\Psi^*(\mathbf{r},\mathbf{R})$, and integrating over all space, we get

$$\begin{aligned}\left(-\sum_\alpha \frac{m}{2M_\alpha}\nabla_\alpha^2 + E(\mathbf{R}) + W(\mathbf{R}) - E_T\right)\chi(\mathbf{R}) &= \\ \sum_\alpha \int \Psi^*(\mathbf{r},\mathbf{R})\frac{m}{M_\alpha}\nabla_\alpha\Psi(\mathbf{r},\mathbf{R})\nabla_\alpha\chi(\mathbf{R})d\mathbf{r}\,, \end{aligned}\tag{2.7}$$

The left hand side is the Schrödinger equation for ionic motion in a potential $E + W$ where $E(\mathbf{R})$ is the effective potential arising from all the electrons and nuclei and $W(\mathbf{R})$ is an extra term arising from the correlated motion of electrons with the nuclei. $W(\mathbf{R})$ is defined as,

$$W(\mathbf{R}) = \sum_a \frac{m}{2M_\alpha}\int \Psi^*(\mathbf{r},\mathbf{R})\nabla_a^2\Psi(\mathbf{r},\mathbf{R})d\mathbf{r} \tag{2.8}$$

This term is negligbly small and is omitted.

If Ψ is real and corresponds to a non-degenerate ground state then the term on the right hand side of Eq. 2.7 vanishes. Otherwise it results in only small perturbations, but, in the case of a degenerate, or near degenerate ground state may become important (eg Jahn-Teller effect). Neglecting this term results in decoupling of the electron and ion motions.

Having applied the Born-Oppenheimer approximation, we have,

$$\left(-\sum_\alpha \frac{m}{2M_\alpha}\nabla_\alpha^2 + E(\mathbf{R})\right)\chi(\mathbf{R}) = E_T\chi(\mathbf{R}) \tag{2.9}$$

Expanding the potential energy term $E(\mathbf{R})$ about its minimum gives the ground state structure, and this is the main objective of the calculations. The key problem remaining is the derivation of electronic interaction term in Eq. 2.4. At this stage Hartree-Fock and density functional theory take different approaches. In Hartree-Fock theory, one-electron wavefunctions are constructed as the fundamental variable and are used to uniquely determine the total energy. In density functional theory the electronic charge density is the fundamental variational parameter.

2.3 Density functional theory

In order for the charge density, $n(\mathbf{r})$ to be useful in its role as the variational parameter it must uniquely determine the ground state wavefunction $\Psi(\mathbf{r})$ where the dependence upon R is dropped. The electron density is defined by

$$n(\mathbf{r}_1) = \sum_{\mu} \int \delta(\mathbf{r}_1 - \mathbf{r}_\mu) |\Psi(r)|^2 dr \tag{2.10}$$

The proof of the uniqueness of the charge density now follows. Suppose that two potentials exist which give rise to the same charge density, n. From the variational principle, if Ψ_1 and Ψ_2 are the ground state wavefunctions for two potentials V_1 and V_2 with common charge density n and if $\hat{H}_i \Psi_i = E_i \Psi_i$ then

$$\begin{aligned} E_1 &= \langle \Psi_1 | \hat{H} | \Psi_1 \rangle < \langle \Psi_2 | \hat{H} | \Psi_2 \rangle & (2.11) \\ & E_2 + \langle \Psi_2 | V_1 - V_2 | \Psi_2 \rangle & (2.12) \\ & E_2 + \int (V_1 - V_2) n(r) dr & (2.13) \end{aligned}$$

Equally, we can show the converse

$$E_2 < E_1 + \int (V_2 - V_1) n(r) dr \tag{2.14}$$

adding these two equations together gives

$$E_2 + E_1 < E_1 + E_2 \tag{2.15}$$

This is a contradiction. Therefore the assumption that both V_1 and V_2 lead to the same ground state charge density $n(\mathbf{r})$ is incorrect and so the charge density uniquely defines $V_{\mathrm{e-ion}}$ and hence $\Psi(r)$. For the degenerate case it has also been shown that the 1:1 correspondence between n and Ψ holds.

Since Ψ is a unique functional of n we can solve the Schrödinger equation for Ψ in terms of n. It directly follows that the ground state total energy E is also uniquely determined by n. The significance of this result from a computational standpoint is considerable. Hartree Fock theory minimizes the energy of a system of N electrons using the electronic wavefunctions which depend upon $4N$ variables, the coordinates (x, y, z, spin) of each electron. Since the electronic charge density is simply a function of three variables, x, y and z, the variational procedure is vastly simplified.

2.3.1 The variational principle

The total energy E is a functional of the charge density,

$$E[n] = T[n] + E_{\text{e-ion}}[n] + E_H[n] + E_{xc}[n] + E_{\text{ion-ion}} \tag{2.16}$$

The electron–ion term and Hartree term are readily available as simple functionals of n

$$\begin{aligned} E_{\text{e-ion}}[n] &= -\int n(\mathbf{r}) \sum_a \frac{Z_a}{|\mathbf{r} - \mathbf{R}_a|} d\mathbf{r}, & (2.17) \\ E_H[n] &= \frac{1}{2} \int \frac{n(\mathbf{r}_1) n(\mathbf{r}_2)}{|\mathbf{r}_1 - \mathbf{r}_2|} d\mathbf{r}_1 d\mathbf{r}_2 & (2.18) \end{aligned}$$

The ion–ion term is also easily derived,

$$E_{\text{i-i}} = \frac{1}{2} \int \sum_{a \neq b} \frac{Z_a Z_b}{|\mathbf{R}_a - \mathbf{R}_b|} \tag{2.19}$$

The challenging terms are then the exchange-correlation energy E_{xc} and the kinetic energy term, T.

2.3.2 The kinetic energy

The kinetic energy term is treated through the introduction of a set of orthonormal orbitals as a basis for the charge density,

$$n_s(\mathbf{r}) = \sum_{i=1}^{N} |\psi_i(\mathbf{r})|^2, \tag{2.20}$$

where ψ_i is the wavefunction of the i^{th} occupied state. These Kohn-Sham states are employed solely as a mathematical tool for expanding the charge density and therefore will not in general reflect the one-electron states of the system. This step allows the kinetic energy to be written in terms of the charge density,

$$T = -\frac{1}{2} \sum_{i,s} \int \psi_i^* \nabla^2 \psi_i d\mathbf{r}. \tag{2.21}$$

2.3.3 The exchange-correlation energy

The exchange-correlation energy encompasses the complicated many-body interactions between electrons. Rigorous evaluation of this term is prohibitively computationally demanding and can only be applied to systems containing a few atoms. Density-functional theory approximates the exchange-correlation energy, E_{xc} in terms of the exchange-correlation energy density, ϵ_{xc}:

$$E_{xc}[n] = \int n(\mathbf{r})\epsilon_{xc}(n_\uparrow, n_\downarrow)d\mathbf{r} \tag{2.22}$$

The local density approximation (LDA) replaces the exchange-correlation potential at a point $\mathbf{r}$, charge density, $n(\mathbf{r})$ by that for a homogeneous electron gas with the same charge density, ϵ_{xc}^{hg} :

$$\epsilon_{xc}(\mathbf{r}) = \epsilon_{xc}^{hg}(n(\mathbf{r})) \tag{2.23}$$

The exchange correlation potential for an ideal gas is written

$$\mu_{xc}(\mathbf{r}) = \frac{\delta E_{xc}[n]}{\delta n(\mathbf{r})} = \epsilon_{xc}(n(\mathbf{r})) + n(\mathbf{r})\epsilon'_{xc}(n(\mathbf{r})) \tag{2.24}$$

which is correct in two limiting cases where the kinetic energy term dominates: (a) slowly varying $n(\mathbf{r})$ and (b) high density $n(\mathbf{r})$.

In order to find $\epsilon_{xc}(n(\mathbf{r}))$, valid for realistic electronic densities appropriate to the solid-state a numerical approximation is made to Eq. 2.24. AIMPRO takes the parametrisation of $\epsilon_{xc}(n(\mathbf{r}))$ as calculated exactly using quantum Monte-Carlo methods[13]. For the case of a spin polarised electron case, it is of the form

$$\epsilon_{xc}(\mathbf{r_s}) = \epsilon_x(\mathbf{r_s}) + \epsilon_c(\mathbf{r_s}), \tag{2.25}$$

where

$$\epsilon_x(\mathbf{r_s}) = -\frac{0.4582}{r_s}, \tag{2.26}$$

and

$$\epsilon_c(\mathbf{r_s}) = -0.0843\ [1 + 1.3981\sqrt{(}r_s) + 0.2611\ r_s]^{-1}, \qquad r_s \geq 1 \tag{2.27}$$

$$\epsilon_c(\mathbf{r_s}) = -0.0269 + 0.0155 \ln r_s - 0.0048 r_s + 0.0007 r_s \ln r_s, \qquad r_s \leq 1 \tag{2.28}$$

where r_s is the Wigner-Seitz radius for each electron given by $r_s = (4\pi n/3)^{-1/3}$.

2.3.4 The Kohn-Sham equations

Minimizing the total energy E with respect to n and ensuring the conservation of total spin and number of electrons, we arrive at the Kohn Sham equations:

$$\left\{-\frac{1}{2}\nabla^2 - \sum_a \frac{Z_\alpha}{|r-R_\alpha|} + V^H(r) + V^{xc}_{s,\lambda}(n_\uparrow, n_\downarrow) - E_\lambda\right\}\psi_\lambda(r) = 0 \tag{2.29}$$

$$\int |\psi_\lambda(r)|^2 dr = 1, \tag{2.30}$$

where the spin-polarised exchange-correlation potential is given by

$$V^{xc}_s = \frac{d(n\epsilon_{xc})}{dn_s}. \tag{2.31}$$

Since the Kohn-Sham orbitals ψ_λ are simply used as a tool to produce the correct charge density, they do not necessarily resemble the one-particle states as calculated by Hartree-Fock theory. Similarly, the Kohn-Sham eigenvalues are just the Langrangian multipliers used in the energy minimization and so cannot be identified with the true energy eigenvalues. It has been shown, however that the highest occupied orbital, with fractional occupancy, possesses an eigenvalue equal to the ionisation energy [14]. Furthermore, in practice, a high degree of commonality often does exist between the Kohn-Sham orbitals and those observed experimentally as shown in the next chapter.

2.3.5 Pseudopotential theory

Consideration of all the electrons associated with an atom is computationally demanding and all-electron potentials are usually replaced by *pseudopotentials*. This approximation is appropriate for solid-state systems because the electrons involved in the bonding processes between atoms are a subset of the total number of electrons. In pseudopotential theory, these valence electrons are modelled accurately, whereas the tightly bound core electrons which do not play a significant role in bonding are transformed away. The use of pseudopotentials has several associated advantages:

1. As the number of core electrons increases, the wavefunction orthonormality condition causes the electronic orbitals to become increasingly oscillatory. Use of pseudopotentials allows the exclusion of these rapidly varying core wavefunctions which are difficult to model.

2. The exclusion of the core states results in a large lowering in the magnitude of the total energy. In energetical calculations, where energy differences of less than 0.2 eV are of significance, this situation is desirable as the consequent errors are lowered.
3. The high kinetic energy of core electrons, particularly in large mass atoms means that direct modelling of the core states would have to include relativistic effects. Since the valence electrons retain non-relativistic behaviour this extra demand is not required.

There are several possible methods for constructing pseudopotentials. For example, in calculations where the wavefunctions must be fitted to plane-waves, it is desirable to have pseudopotentials which decay rapidly with wave-vector such as the soft-pseudopotentials of Vanderbilt [15]. In AIMPRO, where Gaussians are employed as the fitting functions, this is not important and the pseudopotentials of Bachelet, Hamann and Schlüter [16] are used. These pseudopotentials have several fundamental properties:

1. The real and pseudo-valence eigenvalues are equal for a chosen prototype atomic configuration,
2. Beyond a chosen core radius r_c the real and pseudo-atomic wavefunction agree exactly,
3. The integrated charge density is the same for both real and pseudo-charge densities for $r > r_c$ (*norm conservation*),
4. The first energy derivatives and logarithmic derivatives of the real and pseudo-wave function agree for $r > r_c$.

2.3.5.1 Generating pseudopotentials

Initially, an all-electron calculation is performed for the atom and the Kohn-Sham equations are solved with the following requirements: (a) choosing a spherically symmetric charge density, the KS levels are labelled by angular momentum l (or $j = l \pm 1/2$ for heavier elements where the Dirac formalism is included) and (b) All orbitals which contribute in a bonding state must be taken into account. This is important,for example, in carbon where the atomic configuration ($1s^2 2s^2 2p^2$) contains no occupied d-orbital whilst in a bonded structure like diamond, the bonding states are constructed through a combination of, in general, s, p and d states. To account for this the $l = 2$ potential is constructed from the ionised configuration $1s^2 2s^{0.75} 2p^1 3d^{0.25}$. The procedure for choosing these configurations minimizes small anomalies in the potential. An all-electron potential, $V^v(r)$ is constructed from the set of KS equations which is singular at $r = 0$. An initial guess at a pseudopotential is made which removes the singularity:

$$V_l(r) = V^\nu(r)\left(1 - f\left(\frac{r}{r_{c,l}}\right)\right) + c_l^\nu f\left(\frac{r}{r_{c,l}}\right). \tag{2.32}$$

where $r_{c,l}$ is the core radius and the function $f(x)$ is chosen so that $f(x)$ tends to 1 as $x \to 0$ and vanishes quickly with increasing x. The core radius $r_{c,l}$ is judiciously chosen to remove the rapidly varying core potential whilst ensuring that no bonding component is lost. Usually, the $r_{c,l}$ is placed midway between outermost node and extremum.

Normalization of the pseudopotential is performed through the creation of a new wavefunction:

$$\omega_{2l}^\nu = \gamma_l^\nu \left\{\omega_{1l}^\nu(r) + \delta_l^\nu r^{l+1} f(r/r_{c,l})\right\} \tag{2.33}$$

where ω_{1l}^ν is the wavefunction corresponding to the potential $V_l(r)$. δ_l^μ and γ_l^μ are normalization constants. Inverting the Schrödinger equation and using the eigenvalues of the all-electron potential, the potential corresponding to the new wavefunction ω_{2l}^ν is found. The final step is to subtract the Hartree and exchange-correlation potential contributions to the pseudopotential as these will be included during the density functional calculation. Whilst the Hartree potential can be subtracted exactly, the calculation of the exchange-correlation potential contribution is approximate. The approximation involves subtracting the exchange-correlation potential due to the all-electron charge density and spin-polarisation [17].

For relativistic atoms, where the all-electron calculation takes account of the Dirac equation, the resulting pseudopotential $V_l^{ps}(r)$ is written

$$V_l^{ps}(r) = \sum_l |l\rangle \left\{V_l(r) + V_l^{so}(r)\mathbf{L}\cdot\mathbf{S}\right\} \langle l| \tag{2.34}$$

and is constructed using the scalar relativistic potential:

$$V_l(r) = \frac{1}{2l+1}\left\{l V_{l-1/2}(r) + (l+1)\, V_{l+1/2}(r)\right\} \tag{2.35}$$

and the spin-orbit potential:

$$V_l^{so}(r) = \frac{2}{2l+1}\left\{lV_{l+1/2}(r) - V_{l-1/2}(r)\right\} \tag{2.36}$$

2.4 AIMPRO methodology

Thus far we have considered the background to DFT and the use of pseudopotentials. There exists a wide range of methods in popular use which enable the implementation of the theory. The various methodologies are characterised to a large extent by the following factors:

- real- (cluster) or k-space (supercell) calculations
- type of basis set functions used
- force calculation method
- form of exchange-correlation potential

In this chapter the methods used in AIMPRO are expounded upon. The first key point is that AIMPRO exists in two forms; cluster and supercell. We consider first the cluster implementation and subsequently examine those methods which are used in the supercell method which are distinct from the cluster implementation.

2.4.1 Expansion of the wavefunction

An expansion of the Kohn-Sham orbitals is made using a set of basis set functions $\phi_i(\mathbf{r} - \mathbf{R_i})$ and spin-functions $\chi_{\pm\frac{1}{2}}(s)$,

$$\Psi_\lambda(r, s) = \chi_{\pm\frac{1}{2}}(s)\sum_i c_i^\lambda \phi_i(\mathbf{r} - \mathbf{R_i}) \tag{2.37}$$

Now the Kohn-Sham orbitals can be written in matrix form, using the c_i^λ. The orbital character is set by employing Gaussian function multiplied by Cartesian polynomial spherical functions:

$$\phi(\mathbf{r} - \mathbf{R_i}) = (x - \mathbf{R_{ix}})^{n_1}(y - \mathbf{R_{iy}})^{n_2}(z - \mathbf{R_{iz}})^{n_3}e^{-a_i(\mathbf{r}-\mathbf{R_i})^2} \tag{2.38}$$

Here, the the orbital angular momentum quantum number is set using n_1, n_2 , n_3. For example, choosing $n_1 = n_2 = n_3 = 0$, we generate an s-orbital.

The charge density $n_s(\mathbf{r})$ is constructed for spin up and spin down orbitals in terms of a density matrix;

$$n_s(\mathbf{r}) = \sum_{i,j} b_{i,j,s}\phi_i(\mathbf{r} - \mathbf{R_i})\phi_j(\mathbf{r} - \mathbf{R_i}) \tag{2.39}$$

$$b_{i,j,s} = \sum_{\lambda_{\mathrm{occ}}} \delta(s, s_\lambda)c_i^\lambda c_j^\lambda \tag{2.40}$$

where the sum is over occupied states. To calculate the terms that make up the total energy, it is necessary to write the terms in the Hamiltonian in terms of the $b_{i,j,s}$ matrix. Two of these terms, the kinetic and pseudopotential energy are easily found analytically:

$$T_{i,j} = -\frac{1}{2}\int \phi_i(\mathbf{r} - \mathbf{R_i})\nabla^2\phi_j(\mathbf{r} - \mathbf{R_i})dr, \tag{2.41}$$

$$V_{i,j} = \int \phi_i(\mathbf{r} - \mathbf{R_a})\sum_a V_a^{\mathrm{ps}}\phi_j(\mathbf{r} - \mathbf{R_j})dr. \tag{2.42}$$

The remaining terms in the total energy, Hartree and exchange-correlation, are evaluated using approximations to the charge density.

2.4.2 Hartree term

The expression for the Hartree energy involves $O(N^4)$ integrals (N is the number of basis functions) rendering it prohibitively time consuming to calculate directly. In order to overcome this problem, the Hartree energy is re-expressed in terms of an approximate charge density $\tilde{n}_s(\mathbf{r})$. This approximation is written as a linear sum of basis functions,

$$\tilde{n}_s(\mathbf{r}) = \sum_k c_{k,s}g_k(\mathbf{r}), \qquad \tilde{n}(\mathbf{r}) = \sum_s \tilde{n}_s(\mathbf{r}) \tag{2.43}$$

The Hartree energy term is now replaced by an approximate Hartree energy $\tilde{E}_H$. The approximate Hartree energy is written so that

$$\tilde{E}_H = \int \frac{n_s(r_1)\tilde{n}_s(r_2)}{|\mathbf{r}_1 - \mathbf{r}_2|} - \frac{1}{2}\int \frac{\tilde{n}_s(r_1)\tilde{n}_s(r_2)}{|\mathbf{r}_1 - \mathbf{r}_2|} \tag{2.44}$$

so that the approximate Hartree energy equal the exact Hartree energy when $\tilde{n} = n$. The error in the Hartree energy is minimized with respect to the fitting function coefficients. The error is given by:

$$E_H - \tilde{E}_H = \frac{1}{2}\int \frac{\{n_s(\mathbf{r}_1) - \tilde{n}_s(\mathbf{r}_1)\}\{n(\mathbf{r}_2 - \tilde{n}_s(\mathbf{r}_1)\}}{|\mathbf{r}_1 - \mathbf{r}_2|} \tag{2.45}$$

Differentiating with respect to the c_k gives:

$$\sum_l G_{kl} c_l = \sum_{ij} t_{ijk} b_{ij}, \tag{2.46}$$

where

$$t_{ijk} = \int \phi(\mathbf{r}_1 - \mathbf{R}_i)\phi_j(\mathbf{r}_1 - \mathbf{R}_j) g_k(\mathbf{r}_2) \frac{1}{|\mathbf{r}_1 - \mathbf{r}_2|} d\mathbf{r}_1 d\mathbf{r}_2 \quad \text{and} \tag{2.47}$$

$$G_{kl} = \int g_k(\mathbf{r}_1) g_l(\mathbf{r}_2) \frac{1}{|\mathbf{r}_1 - \mathbf{r}_2|} d\mathbf{r}_1 d\mathbf{r}_2. \tag{2.48}$$

Atom centred or bond-centred Gaussian functions are used for g_k. The evaluation of t_{ijk} can be simplified (optionally), by choosing a more sophisticated form of g_k:

$$\left\{1 - \frac{2b_k}{3}(\mathbf{r} - \mathbf{R}_k)^2\right\} \exp\left(-b_k(\mathbf{r} - \mathbf{R}_k)^2\right) \tag{2.49}$$

which give rise to a Gaussian potential,

$$\int \frac{g_k(\mathbf{r}_1)}{|\mathbf{r} - \mathbf{r}_1|} d\mathbf{r}_1 = \frac{3b_k}{2\pi} \exp\left(-b_k(\mathbf{r} - \mathbf{R}_k)^2\right) \tag{2.50}$$

Additional pure Gaussian functions are necessary to contribute to the total number of electrons when the integrals of the g_k vanish.

2.4.3 The exchange-correlation term

The exchange-correlation energy is also evaluated from an approximate charge density. The fitting functions are different from those employed to evaluate $\tilde{E}_H$ because error minimization is performed to reduce the error in $\tilde{n}$ at a given $\mathbf{r}$ rather than reducing the error in $n - \tilde{n}$. The exchange-correlation is given by:

$$E_{xc} = \int \epsilon_{xc}(n_\uparrow, n_\downarrow) n d\mathbf{r}, \tag{2.51}$$

$$E_{xc} = \int \epsilon_{xc}(\tilde{n}_\uparrow, \tilde{n}_\downarrow) \tilde{n} d\mathbf{r}, \tag{2.52}$$

Again, the approximate charge density $\tilde{n}_s$ is expanded in a basis of simple Gaussian functions h_k;

$$\tilde{n}_s(\mathbf{r}) = \sum_k d_{k,s} h_k(\mathbf{r}), \tag{2.53}$$

where $d_{k,s}$ are the coefficients used to minimize the error,

$$\int \{n_s(\mathbf{r}) - \tilde{n}_s(\mathbf{r})\}^2 \, d\mathbf{r}, \tag{2.54}$$

which gives

$$\sum_l H_{kl} d_{l,s} = \sum_{ij} u_{ijk} b_{ij,s}, \tag{2.55}$$

where

$$u_{ijk} = \int \phi(\mathbf{r} - \mathbf{R}_i)\phi_j(\mathbf{r} - \mathbf{R}_j)h_k(\mathbf{r}) \quad \text{and} \tag{2.56}$$

$$H_{kl} = \int h_k(\mathbf{r})h_l(\mathbf{r}) \tag{2.57}$$

In the spin averaged case, we drop the spin labels. Now the resulting approximation to the exchange-correlation energy is given by

$$\tilde{E}_{xc} = \sum_k d_k \int h_k(\mathbf{r})\epsilon_{xc}(\tilde{n})dr \tag{2.58}$$

Because Gaussian orbitals have been chosen for h_k this integral is proportional to the average value of the exchange-correlation density ϵ_{xc} under these functions $\langle \epsilon_{xc}(\tilde{n})\rangle_k$:

$$\int h_k(\mathbf{r})\epsilon_{xc}(\tilde{n})d(\mathbf{r}) \propto \langle \epsilon_{xc}(\tilde{n})\rangle_k \tag{2.59}$$

Since $\epsilon_{xc}(\tilde{n})$ is slowly varying with charge density we can approximate $\langle \epsilon_{xc}(\tilde{n})_k\rangle$ by $\epsilon_{xc}(\langle \tilde{n}\rangle_k)$. This step replaces the exact charge density at a point by the value for the homogeneous electron gas with average density $\langle \tilde{n}_k\rangle$:

$$\langle \tilde{n}_k\rangle = \frac{\sum_l d_l \int h_k h_l d\mathbf{r}}{\int h_k d\mathbf{r}} \tag{2.60}$$

This approximation is improved upon by expressing the exchange-correlation density as $\epsilon_{xc}(n) = An^{0.30917}$ and defining a new function $f(s)$,

$$f(s) = ln\left(\frac{\langle \tilde{n}^s\rangle_k}{\langle \tilde{n}\rangle_k^s}\right) \tag{2.61}$$

$f(s)$ is approximated using a limited expansion

$$f(s) = \frac{1}{2}s(s-1)f(2) \tag{2.62}$$

This approximation is one of the largest used in AIMPRO. Since it contributes only a small amount to the total energy, however, the effect of any error is small. $f(2)$ can be found after evaluation of the second moment of $\tilde{n}$:

$$\langle \tilde{n}_k^2 \rangle = \frac{\sum_{lm} d_l \int h_k h_l h_m d\mathbf{r}}{\int h_k d\mathbf{r}} \tag{2.63}$$

leading to the final expression for the exchange-correlation energy:

$$\tilde{E}_{xc} = \sum_k d_k \epsilon_k, \tag{2.64}$$

where

$$\begin{aligned} \epsilon_k &= I_k \epsilon_{xc}(\langle \tilde{n}^2 \rangle_k) e^{f_k} && (2.65) \\ f_k &= \frac{1}{2}s(s-1)ln\left(\frac{\langle \tilde{n} \rangle_k}{\langle \tilde{n} \rangle_k}\right) && (2.66) \\ I_k &= \int h_k(\mathbf{r}) d\mathbf{r} && (2.67) \end{aligned}$$

A similar expression has been derived for the spin polarised case [18].

2.4.3.1 The eigenvalue equation

Combining all the terms we arrive at the total energy:

$$E = \sum_{ij} \left\{ T_{ij} + V_{ij}^{ps} \right\} b_{ij} + \tilde{E}_H + \tilde{E}_{xc} + E_{\text{ion-ion}} \tag{2.68}$$

where i and j label the coefficients of the basis orbitals. The total energy is now minimized with respect to the orthonormal set of wavefunctions $\psi_\lambda(r)$, subject to the constraint

$$\sum c_i^\lambda c_j^\lambda S_{ij} = \delta_{\lambda\mu}, \tag{2.69}$$

where S_{ij} is the overlap matrix. This is achieved through the introduction of Lagrange multipliers E_λ:

$$\sum_{ij\lambda} c_i^\lambda \left\{ T_{ij} + V_{ij}^{p,s} - E_\lambda S_{ij} \right\} c_j^\lambda + \tilde{E}_H + \tilde{E}_{xc}^H + E_{\text{ion-ion}} \tag{2.70}$$

Differentiating this with respect to c_i^λ we arrive at the KS equations:

$$\sum_i \left\{ T_{ij} + V_{ij}^{ps} + V_{ij}^{H} + V_{ij,s\lambda}^{xc} - E_\lambda S_{ij} \right\} c_j^\lambda = 0 \tag{2.71}$$

where the exchange-correlation and Hartree potentials are introduced by

$$\frac{\partial \tilde{E}_H}{\partial c_i^\lambda} = \sum_j V_{ij}^H c_j^\lambda, \qquad V_{ij}^H = \sum_{kl} G_{kl} c_l \frac{\partial c_k}{\partial b_{ij}} \tag{2.72}$$

$$\frac{\partial \tilde{E}_{xc}}{\partial c_i^\lambda} = \sum_j V_{ij,s_\lambda}^{xc} c_j^\lambda, \qquad V_{ij,s}^{xc} = \sum_k \left\{ \epsilon_{k,s} + \sum_l d_{l,s} \frac{\partial \epsilon_{l,s}}{\partial d_{k,s}} \right\} \frac{\partial d_{k,s}}{\partial b_{ij,s}} \tag{2.73}$$

Using Eqs. 2.46 and 2.55 we get

$$\sum_l G_{kl} \frac{\partial c_l}{\partial b_{ij}} = t_{ijk} \qquad \sum_l H_{kl} \frac{\partial d_{l,s}}{\partial b_{ij,s}} = u_{ij,s} \tag{2.74}$$

We can now rewrite Eq. 2.71 in generalized matrix form:

$$\sum_j \left(H_{ij} - ES_{ij} \right) c_j = 0, \qquad or \qquad (H - ES)\, c = 0 \tag{2.75}$$

The overlap matrix S is transfered by a Choleski decomposition, i.e. $S = U^t U$, where U is upper triangular matrix, followed by inversion of matrix, U. The problem is then converted into a standard eigenvalue one by defining $Uc = d$ and $(U^{-1})^t H U^{-1} = V$:

$$(V - E)d = 0 \tag{2.76}$$

The eigenvalues are evaluated using the standard Householder method with an inverse iteration procedure used to find the eigenvectors for the occupied and lowest unoccupied states.

2.4.3.2 Electronic self-consistency

The redistribution of charge between atoms is enabled through a self-consistent cycle. To achieve self-consistency the charge density generated by an external potential must be equal to the charge density that generated that potential within some tolerance. The initial guess at the charge density is often taken to be that of the neutral atom.

To begin the process, the initial charge density coefficients c_k^i and $d_{k,s}^i$ are used as input to the KS equations. A density matrix $b_{ij,s}$ is generated with output charge density coefficients say, c_k^{out}, $d_{k,s}^{\text{out}}$. A weighted average of the input and output charge densities then provides the new input coefficients,

$$c'_k = c_k + w(c_k^{\text{out}} - c_k), \qquad d'_{k,s} + w(d_{k,s}^{\text{out}} - d_{k,s}) \tag{2.77}$$

This process for obtaining the output charge density is denoted by the non-linear operation, $c_k^{\text{out}} = L_k(c_k^{\text{in}})$. The output charge density which is generated from an input weighted average can be written

$$c_k'^{\text{out}} = L_k((c_k^{\text{in}} + w(c_k^{\text{out}} - c_k^{\text{in}}) \tag{2.78}$$

For small w this expression can be expanded in a Taylor series:

$$\begin{aligned} c_k'^{\text{out}} &= L_k(c_k^{\text{in}}) + w \sum_l D_{kl}(c_{kl}^{\text{in}} - c_{kl}) && (2.79) \\ &= c_k^{\text{out}} + w \sum_l D_{kl}(c_{kl}^{\text{in}} - c_{kl}) && (2.80) \end{aligned}$$

where

$$D_{kl} = \frac{\partial L_k}{\partial c_l} \tag{2.81}$$

for self-consistency, we require $c_k'^{\text{out}} = c_k'^{\text{in}}$ or

$$c_k^{\text{in}} + w(c_k^{\text{out}} - c_k^{\text{in}}) = c_k^{\text{out}} + w \sum_l D_{kl}(c_{kl}^{\text{out}} + c_{kl}^{\text{in}}) \tag{2.82}$$

giving

$$(w^{-1} - 1)(c_k^{\text{in}} + c_k^{\text{out}}) = \sum_l D_{kl}(c_{kl}^{\text{out}} + c_{kl}^{\text{in}}) \tag{2.83}$$

A small trial value for w, say w_1 must be chosen. The output charge density is then given by,

$$c_{1k}'^{\text{out}} = c_k^{\text{out}} + w_1 \sum_l D_{kl}(c_l^{\text{out}} - c_l). \tag{2.84}$$

or

$$\sum_l D_{kl}(c_l^{\text{out}} - c_l) = \frac{c_{1k}'^{\text{out}} - c_k^{\text{out}}}{w_1} \tag{2.85}$$

Comparing Eqs. 2.83 and 2.85, a value for w can be selected which minimizes

$$\sum_k e_k g_k(\mathbf{r}) \tag{2.86}$$

where e_k is the difference between Eqs. 2.83 and 2.85,

$$\frac{(1-w)(c_k - c_k^{\text{out}})}{w} - \frac{(c_k'^{\text{out}} - c_k^{\text{out}})}{w_1} \tag{2.87}$$

In practice, the charge density self-consistent cycle converges exponentially. The tolerance for the self-consistent condition is set to be around 10^{-5} au.

Problems can occur during the self-consistency cycle due to level crossing. When two electronic levels, one occupied, the other unoccupied, become close in energy or degenerate, *charge sloshing* can occur. This happens when, in the subsequent self-consistency cycle, the filling of these two states is swapped. The consequence is that the Hubbard term raises the energy of the now filled level so that in the next cycle the level ordering reverts back to the original state. If this *charge sloshing* process continues convergence of the charge density is never achieved.

This problem can be overcome through the implementation of a *finite temperature*. The electronic filling is determined through the use of Fermi statistics so that partial filling of the highest occupied states occurs.

The energy to be minimized is the free energy F,

$$F = E + k_B T \sum_{\lambda} \{ f_\lambda \ln f_\lambda + (1 - f_\lambda) \ln (1 - f_\lambda) \} - \mu \left\{ \sum_{\lambda} f_\lambda - N \right\} \tag{2.88}$$

where the energy levels E_λ are occupied by f_λ electrons, μ is the chemical potential and N is the total number of electrons. The minimization of Eq. 2.88 with respect to the chemical potential gives:

$$f_\lambda = \frac{1}{e^{(E_\lambda - \mu)/k_B T} + 1} \qquad \text{and} \qquad \sum_{\lambda} f_\lambda = N \tag{2.89}$$

The density-matrix must be put in general form,

$$b_{ij,s} = \sum_{\lambda} \delta(s, s_\lambda) f_\lambda c_i^\lambda c_j^\lambda. \tag{2.90}$$

A finite temperature is applied only when optimizing defect structures when level crossing may occur or the defect has partial filled degenerate levels. Care must be taken when the defect is Jahn-Teller active as the driving force for the Jahn-Teller distortion can be removed by smearing the electronic filling. Where used in this thesis, the finite temperature is set to $k_B T = 0.04$ eV.

2.4.3.3 Evaluation of forces

When self-consistency is achieved, the forces acting on each atom in the system must be calculated so that the atom positions can be shifted accordingly. The forces are calculated from the gradient of the free energy F with respect to displacement. The force acting on atom a in the direction l is

$$f_{la} = -\frac{\partial F}{\partial R_{la}} \tag{2.91}$$

Inserting this into Eq. 2.70, the forces are found analytically by calculating the change in energy for a displacement, ΔR_{la},

$$\Delta E = \sum_{ij} \Delta \left\{ T_{ij} + V_{ij}^{ps} \right\} + \sum_{ij} \left\{ T_{ij} + V_{ij}^{ps} \right\} \Delta b_{ij} + \Delta \tilde{E}_H + \Delta \tilde{E}_{xc} + \Delta \tilde{E}_{\mathrm{ion-ion}} \tag{2.92}$$

where

$$\begin{aligned} \Delta \tilde{E}_H &= \sum_{kl} c_k G_{kl} \Delta c_l + \frac{1}{2} \sum_{kl} c_k c_l \Delta_{kl} && (2.93) \\ \Delta \tilde{E}_{xc} &= \sum_{k,s} \epsilon_{k,s} \Delta d_{k,s} + \frac{1}{2} \sum_{k,s} \Delta \epsilon_{k,s} && (2.94) \end{aligned}$$

Algebraic manipulation of these equations eliminates Δc_l and $\Delta d_{l,s}$ leaving terms in $\Delta S_{ij}, \Delta G_{kl}, \Delta H_{kl}$ and $\Delta \epsilon_{k,s}$. The latter term depends upon $\Delta \langle \tilde{n}_s \rangle_k$ and $\Delta \langle \tilde{n}_s^2 \rangle_k$ which can be found using Eq. 2.60 and Eq. 2.63. The pseudopotential term depends upon the atomic positions through $V_a^{ps}(\mathbf{r} - \mathbf{R}_a)$. This term is found by integrating by parts replacing terms with $\Delta\phi$:

$$\begin{aligned} &\int \phi_i(\mathbf{r} - \mathbf{R}_i) \Delta V_a^{ps}(\mathbf{r} - \mathbf{R}_a) \phi_j(\mathbf{r} - \mathbf{R}_a) dr = && (2.95) \\ &\int \left\{ \phi_j(\mathbf{r} - \mathbf{R}_j) \Delta \phi_i(\mathbf{r} - \mathbf{R}_a) + \phi_i(\mathbf{r} - \mathbf{R}_a) \Delta \phi_j(\mathbf{r} - \mathbf{R}_a) \right\} V_a^{ps}(\mathbf{r} - \mathbf{R}_a) dr && (2.96) \end{aligned}$$

2.4.3.4 Conjugate gradient optimization

Since the forces on all the atoms are known the atoms can be moved iteratively to find the lowest energy structure. There are several methods that could be employed to achieve this, the simplest being *steepest descent*. AIMPRO employs the *conjugate gradient* algorithm which uses knowledge of previous search directions combined with the latest forces to set the direction to move the atoms.

If the force on atom a is f'_{la} acting in direction l then the atom is moved along the conjugate direction d'_{la} giving the new location

$$R'_{la} = R_{la} + \omega d'_{la} \tag{2.97}$$

where ω is chosen to minimize the free energy via a cubic or quadratic interpolation scheme. The new search direction is a combination of the new forces f'_{la} as well as the previous forces f_{la} and search direction d_{la}:

$$d'_{la} = f'_{la} = -\frac{\sum_{la} f'_{la}\,(f'_{la} - f_{la})}{\sum_{la} f^2_{la}} d_{la} \tag{2.98}$$

For the first iteration the atoms are moved in the directions of the forces. The use of conjugate gradient mechanism results in quadratic convergence. The most serious drawback of any such simple method is that there is no guarantee of locating the global system minimum. In practice this means that the initial atomic positions must be 'close enough' to the global minimum for the geometric ground state to be found. Exactly how close depends strongly upon the defect and it is often necessary to try a number of different initial structures and compare their optimized energies to find the global minimum.

2.5 Supercell AIMPRO

2.5.1 The supercell approach

The supercell approach models periodic systems of atoms. The boundary conditions imposed ensure a periodic charge density which constrains the Kohn-Sham orbitals to satisfy Bloch's theorem. Whilst this approach is clearly more suited to the modelling of a pure crystal, the relative merits of the cluster and supercell approaches when modelling point defects are less clear.

One major problem with the cluster method is the potential for a strong defect-surface interaction. Whilst this can be minimised by employing large clusters, it is often difficult to measure the magnitude of the interaction. This problem is clearly overcome in a supercell, but here, consideration of the interactions between defects in neighbouring unit-cells becomes important. Even relatively localised defect states may become spuriously dispersed as a result of defect-defect interactions.

2.5.2 Supercell methodology

The usual approach adopted within supercell formalisms is to choose plane-wave fitting functions for both the Kohn-Sham orbitals and the electronic charge-density. This choice is natural because of the inherent periodicity of the system. The Kohn-Sham orbitals at a point, **k** in the Brillouin zone are thus expanded:

$$\psi_{n\mathbf{k}(\mathbf{r})} = \sum_{\mathbf{G}} c_{n\mathbf{k}}(\mathbf{G}) \exp\left[i(\mathbf{k}+\mathbf{G})\cdot\mathbf{r}\right] \tag{2.99}$$

The orthogonality condition for plane waves with different **G** ensures that no instabilities arise through near-linear dependencies in the basis sets. The plane-wave expansion also has the advantage that there is only one parameter (the maximum $|G|$ value) which can be varied, enabling transparency. Another advantage of plane-waves over Gaussian type fitting functions is that they are complete and non-biased (charge is free to move unrestricted throughout the entire unit cell). The number of plane waves which are used in the fitting is determined by the cut-off energy $E_{\rm cut}$ (usually all plane waves with $G^2/2 < E_{\rm cut}$ are included).

In contrast to most supercell methods, in supercell AIMPRO, the Kohn-Sham wavefunctions are expanded in a basis set of Gaussian functions. Despite the drawbacks outlined above, the choice of localised fitting functions has some advantages over plane-waves. For 'problem' atoms with rapidly varying wavefunctions such as oxygen, a large number of plane waves per atom are needed to ensure good description leading to high computational demands. The expansion using Gaussian functions, on the other hand, is very efficient, and is only weakly dependent upon atom type. When atoms which have rapidly varying pseudo-wavefunctions are present as defects, extra fitting functions may be used strategically. It is because of the strong rôle of problem atoms such as hydrogen, carbon and oxygen as defect in semiconductors that the Kohn-Sham states are expanded using Gaussians in supercell AIMPRO. One drawback of the flexibility concomitant with a localised fitting basis is that the sensitivity of a defect to a number of parameters (the number of functions, exponent values, locations of function centres) must be checked.

The basis consists of Cartesian Bloch-Gaussian orbitals $B_{n,\mathbf{k}}(\mathbf{r})$ which involve a sum of Gaussian orbitals ϕ_i over lattice vectors $\mathbf{R}_L$:

$$B_{n,\mathbf{k}}(\mathbf{r}) = \frac{1}{\sqrt{N}} \sum_{L} e^{n\mathbf{k}\cdot\mathbf{R}_L} \phi_i(\mathbf{r} - \mathbf{R}_i - \mathbf{R}_L) \tag{2.100}$$

as in the cluster version, these basis functions are placed at nuclear sites and at bond-centred positions within the unit cell.

2.5.3 Sampling of the Brillouin zone

Under periodic boundary conditions, the Kohn-Sham orbitals are evaluated at a point, $\mathbf{k}$ within the Brillouin zone. The charge density is given by

$$n(\mathbf{r}) = \sum_{n\mathbf{k}} f_{n\mathbf{k}} |B_{n\mathbf{k}}(\mathbf{r})|^2 \tag{2.101}$$

where the sum is over all bands and allowed k-points in the Brillouin zone. $f_{n\mathbf{k}}$ denotes the occupancy of band n at the k-point $\mathbf{k}$. As there are an infinite number of k-points, the charge density is sampled at a small set of carefully chosen *special* k-points. In practice, this approach gives a good approximation to the exact charge density. The special points lie within the irreducible Brillouin zone i.e. the smallest part of the Brillouin zone which unfolds into the whole zone, when the symmetry operations of the system are employed. In AIMPRO, we employ the method of Monkhorst and Pack [19] which chooses a set of equally spaced $\mathbf{k}$-points.

The calculation of the different terms in the total energy may be performed either in real space or Fourier space, whichever is more efficient. In supercell AIMPRO the matrix elements of the kinetic energy and the pseudopotentials are calculated in real space while the Hartree and exchange-correlation energies are found from a Fourier space expansion of the charge density and exchange-correlation terms respectively. In supercell AIMPRO the exchange-correlation parametrisation is chosen to be that of Perdew-Wang [20]. This parametrisation is similar to that of Perdew and Zunger [21] which is employed in the cluster approach but the functional form of the parametrisation ensures no discontinuities in the derivative. Such discontinuities give rise to errors in the Fourier transform of the exchange-correlation term. The forces are calculated by analytically differentiating the total energy with respect to the atomic positions and a conjugate gradient method is used to calculate the search directions following the first iteration.

2.5.4 Summary

This thesis includes the results of calculations from both the cluster and supercell versions of AIMPRO. Whilst the supercell method is often the method of choice, there are good reasons for using the cluster approach. Firstly, the computational demands are lower enabling the routine modelling of larger numbers of atoms within the cluster approach. It is also apparent that cluster modelling of vacancy defects reproduces the experimentally observed bond reconstructions [22, 23] not found using the supercell method [24]. In the subsequent chapter we shall also see that the cluster method may be used to calculate electrical level positions to a reasonable accuracy. One final advantage of the cluster method is that the confinement of the electronic wavefunctions to the region of the cluster results in a widening of the bandgap compared with the pure DFT bandgap. This is advantageous particularly in the case of germanium, where supercell calculations give zero bandgap but the cluster calculation give bandgaps of around 2 eV.

Chapter 3

Experiment

3.1 Introduction

Several experimental techniques are employed in the study of point defects in semiconductors. Throughout this thesis the results of cluster and supercell calculations are compared to experimental data resulting principally from four defect characterisation techniques: electron paramagnetic resonance (EPR), photoluminescence (PL), deep level transient spectroscopy (DLTS) and local vibrational mode spectroscopy (LVMS). Each method allows the measurement of a subset of observables which together quantify the electrical, vibrational, magnetic, optical and geometric properties of a defect. The aim of this chapter is to briefly outline the theoretical background to these methods.

3.2 Electron paramagnetic resonance

3.2.1 Introduction

An electron occupying an orbit has a magnetic dipole moment comprising of orbital and spin contributions. The orbital component arises simply because the system constitutes a current loop. The orbital dipole moment is,

$$\boldsymbol{\mu}_L = -g_L \mu_B \mathbf{L} \tag{3.1}$$

where $g_L = 1$ and μ_B is the Bohr magneton ($eh/2mc$). $\mathbf{L}$ is the orbital angular momentum.

The intrinsic spin of the electron leads to the second contribution,

$$\boldsymbol{\mu}_s = g_s \mu_B \mathbf{S} \tag{3.2}$$

where $g_s = 2.0023$ and $\mathbf{S}$ is the spin.

In silicon, the electrons of each atom are divided into the core electrons (configuration $1s^2 2s^2 2p^6$) and the valence electrons, which take part in bonding. In the atomic configuration, the valence electrons have a configuration $3s^2 3p^2$. As an array of atoms are brought together to form the Si crystal the 3s and 3p states broaden and overlap forming 'sp^3' states. The linear combination of the s with the p_x, p_y and p_z states results in the tetragonal hybrid orbitals. In silicon, carbon and germanium, these occupied orbitals overlap filled orbitals with four neighbouring atoms forming bonds, each bond occupied by a pair of electrons with opposite spins.

It is clear then that the perfect crystals of Si, C and Ge possess no dipole moment: The orbital contribution is said to be 'quenched' as the electrons are confined to highly directional bonds and hence no orbital dipole moment is induced. Since the spins are all paired, the spin 'up' contribution to the dipole exactly cancel with the spin 'down' contribution.

Any defects introduced into the crystal may be accompanied by unpaired electrons. Disruption of the crystal through the creation of intrinsic or extrinsic defects may introduce defect orbitals with energy higher than the valence band edge. In such cases, depending upon the Fermi level position, the orbital may be occupied by unpaired electrons.

The application of a magnetic field to a sample causes the Zeeman splitting of states occupied by unpaired electrons. Defects which posses non-zero spins are termed paramagnetic provided they are in sufficiently low concentrations to prevent any interactions between them. In an EPR experiment, transitions are induced between the Zeeman split levels. The sample is placed inside a microwave cavity with a variable applied magnetic field. Resonance is detected when the microwave frequency matches the Zeeman energy.

The electronic Zeeman interaction is given by

$$\mathscr{H}_{Ze} = -\boldsymbol{\mu} \cdot \mathbf{B}$$

where the magnetic moment, in principle, possesses components due to both the electron spin $\mathbf{S}$ and the orbital momentum $\mathbf{L}$.

$$\boldsymbol{\mu} = -g_s \mu_B \mathbf{S} + g_L \mu_B \mathbf{L}$$

In practice, the orbital angular momentum is quenched for most defects in solids because of the highly varying potential produced by neighboring atoms, and so the electron spin term dominates. The spin-orbit interaction ($\lambda \mathbf{L}\cdot\mathbf{S}$) however can introduce the orbital angular momentum back into the problem. These effects are included by writing

$$\boldsymbol{\mu} = -\mu_B \mathbf{S}\cdot\mathbf{g}$$

where **g** is a symmetric tensor

$$\mathbf{g} = 2.0023 + \Delta\mathbf{g}$$

so that $\Delta\mathbf{g}$ is the angular momentum contribution induced through the spin-orbit interaction. This departure of **g** from the free electron value depends on the orientation of the applied magnetic field. The Hamiltonian now becomes

$$\mathscr{H} = -\mu_B \mathbf{S}\cdot\mathbf{g}\cdot\mathbf{B}$$

The shifts in energy are then given by the values of the azimuthal spin quantum number m_s: $-S, -(S-1), ..., S$,

$$E(m_s) = g\mu_B B m_s,$$

This is shown in Fig. 3.2 for the simple case of $S = 1/2$. In an EPR experiment, the sample is illuminated with radiation of frequency ν, which is fixed by the microwave cavity dimensions, and the magnitude of the Zeeman splitting is varied by sweeping the intensity of the applied field. At resonance, we have

$$B = \frac{h\nu_0}{g\mu_B}$$

In equilibrium, the population ratio N_2/N_1 of the two states will be found by the Boltzmann factor $N_2/N_1 = \exp(-\Delta E/kT)$, where $N_1 + N_2 = N$. When the applied field is adjusted so that resonance occurs the net absorption of radiation tends to equalize the populations as the transition probabilities of the two possible transitions are equal.

Evidently, when the populations are equalized, there is no net power loss, and resonance cannot be detected. Two factors, however prevent the resonance saturation condition. Spontaneous emission will tend to increase the population of the lower level although at the low frequencies involved, the rate is negligible. Secondly, the process of spin-lattice relaxation, which involves the energy transfer of the excited electron to the lattice. This process occurs exponentially with time and the rate increases with the sample temperature.

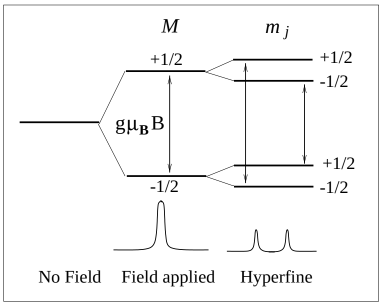

Figure 3.1: Energy level splittings and corresponding EPR signal (below) for a defect with $s = 1/2$. Splitting due to the electronic Zeeman effect and the Hyperfine interaction are indicated.

3.2.2 Hyperfine interaction

Thus far we have included only the interaction of the electron spin with the applied field. Since nuclear spins have associated magnetic moments, they give rise to local fields which may also interact with the unpaired electron. The total magnetic field is then

$$\mathbf{B_{tot}} = \mathbf{B} + \mathbf{B_{loc}}$$

The unpaired electron may interact with a local field due to a number of nuclei j

$$\mu_B \mathbf{g} \cdot \mathbf{B_{loc}} = \sum_j \mathbf{A}_j \mathbf{I}_j \quad ,$$

where the tensor $\mathbf{A}_j$ contains the magnitude, position and angular dependence of the dipole associated with each nucleus j at a point defined by the average position of the unpaired electron. Including both local and applied field terms, the Zeeman interaction is given by

$$\mathscr{H} = \mu_B \mathbf{S} \cdot \mathbf{g} \cdot \mathbf{B} + \sum_j \mathbf{S} \cdot \mathbf{A}_j \cdot \mathbf{I}_j \quad ,$$

The allowed energy states arising from this are determined by the possible combinations of the electronic azimuthal spin quantum number (M) and the nuclear azimuthal spin quantum number (m_j),

$$E(M, m_j) \cong \left(g\mu_B B + \sum_j A_j m_j \right) M \quad ,$$

so that the resonance condition is now given by

$$B = \frac{1}{g\mu_B} \left(h\nu_0 - \sum_j A_j m_j \right) .$$

3.2.3 The nuclear Zeeman interaction

The nuclear Zeeman term in the Hamiltonian takes account of the interaction between the nuclear magnetic moment **I** of nuclei with unpaired spins and the applied magnetic field:

$$H_{Zn} = g_n \beta_n \mathbf{H} \cdot \mathbf{I} \tag{3.3}$$

The energy splittings arising from this interaction are

$$\Delta E_{Zn} = -g_n \beta_n |\mathbf{H}| m_i \tag{3.4}$$

This term is usually the least important in the Hamiltonian and can be extremely complex due to the superposition of several nuclear spins with applied field.

3.2.4 The D-tensor

If a defect has spin greater than 1/2 there is an extra term in the Hamiltonian which can reveal important information about a defect. This is of the form

$$\mathbf{S} \cdot \mathbf{D} \cdot \mathbf{S} \tag{3.5}$$

D arises primarily from spin-spin and spin-orbit interactions between the unpaired electrons. Taking the simple example of a defect which possess two unpaired electrons, occupying orbitals which are well separated, the spin-spin term is a dipole-dipole interaction between the two spins averaged over their spatial distribution. The **D**-tensor reflects the symmetry of the defect and can be interpreted to obtain a value for the average spin-spin separation.

3.2.5 Symmetry assigments

The most fundamental information that EPR can determine is the defect symmetry. Rotation of the applied magnetic field with respect to the crystallographic axes allows the angular dependence of **g** to be mapped. The characteristic angular dependencies of the **g**-tensor for all symmetry groups are shown in Fig 3.2. Note that not all *point group* symmetries are distinguishable using this method as the technique cannot distinguish inversion symmetry.

In materials with the diamond structure (Octahedral symmetry) there are several basic symmetry operations: Using all possible combinations of these operations, we find

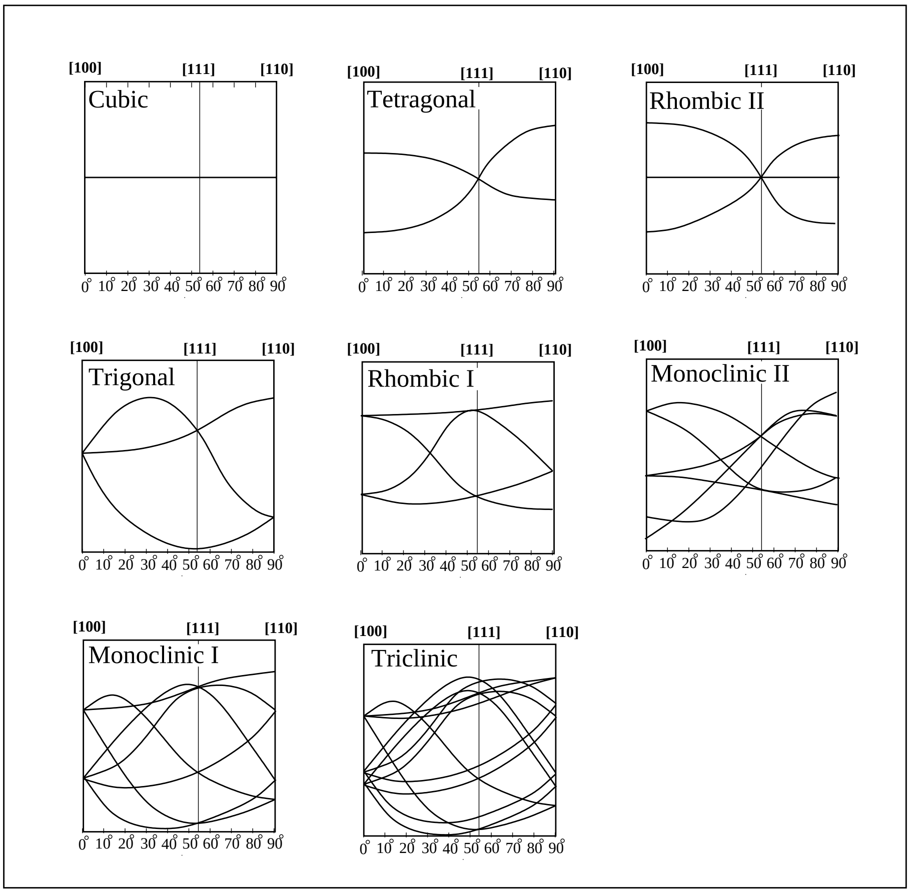

Cubic

Tetragonal

Rhombic II

Trigonal

Rhombic I

Monoclinic II

Monoclinic I

Triclinic

Figure 3.2: Characteristic angular dependencies of absorption for the eight symmetry groups distinguishable by EPR.

that there are 13 symmetry point groups that can exist within the diamond structure. These are listed in table 3.1 along with their component symmetry operations. These symmetry operations are:

- E – the identity transformation
- NC_m – rotation; N is the number of axes m denotes the angle of rotation $2\pi/n$
- σ_v – reflection about plane containing the principal symmetry axis
- σ_h – reflection about plane which is orthogonal to the principal symmetry axis
- NS_m – improper rotational axis (rotation and reflection) N is the number of axes, m denotes the angle of rotation, $2\pi/m$
- i-inversion

Symmetry group	Point group (Order)	Operations
Cubic	$T_d(24)$	E, $8C_3$, $3C_2$, $6S_4$, $6\sigma_d$
Trigonal	$D_{3d}(12)$	E, $2C_3$, $3C_2$, i, $2S_6$, $3\sigma_d$
	$C_{3v}(6)$	E, C_3, $3\sigma_v$
	$C_3(3)$	E, C_3, C_3^2
Tetragonal	$D_{2d}(8)$	E, $2S_4$, C_2, $2C_2'$, $2\sigma_d$
	$S_4(4)$	E, S_4, C_2, S_4^3
Rhombic II	$D_2(4)$	E, C_2, C_2', C_2''
Rhombic I	$C_{2v}(4)$	E, C_2, σ_v, σ_v'
Monoclinic II	$C_2(2)$	E, C_2
Monoclinic I	$C_{2h}(4)$	E, C_2, i, σ_h
	$C_{1h}(2)$	E, σ_h
Triclinic	$C_i(2)$	E, i
	$C_1(1)$	i

Table 3.1: Point groups of octahedral symmetry listed alongside their corresponding symmetry group. For each point group, the operations are listed.

3.2.6 Auxiliary techniques

Whilst the bare EPR method gives valuable information concerning the symmetry and unpaired wavefunction interaction with nuclei, a further source of complementary information may be gleaned through the application of auxiliary methods.

3.2.6.1 The application of stress

Through the use of uniaxial stress, further details of the energies of defects can be found. An important characteristic of an anisotropic defect is the stress or piezospectroscopic tensor [25]. The change in the total energy, E_i of a defect with crystallographic orientation labelled i within a strained crystal is given by

$$\Delta E = Tr\mathbf{B} \cdot \epsilon_{\mathbf{i}}$$

where $\mathbf{B}$ is a traceless stress tensor and ϵ is a tensor representing the strain. In the absence of any imposed stress, an anisotropic defect will exist in a number of degenerate orientations within the crystal. Each orientation will be populated equally. The application of uniaxial stress breaks the orientational degeneracy so that a subset of the possible orientations becomes energetically favourable. After equilibrium is reached, their relative energies can be deduced through the Boltzmann distribution

$$\frac{n_i}{n_j} = \exp\left[(\Delta E_j - \Delta E_i)/kT\right]$$

In EPR the individual defect orientation is monitored through the relative signal amplitudes. Stress is applied at some judicious temperature which allows easy reorientation without enabling the defect to diffuse through the lattice. After equilibrium is reached the sample temperature is reduced and the quenched in alignment is measured after the removal of stress. In the case of a high symmetry defect i.e., D_{2d} the B-tensor may be deduced by the application of stress along a single crystallographic direction. For low symmetry defects the process must be repeated with applied stress along a different direction in order to evaluate all the B-tensor elements.

The activation energy for reorientation can be extracted through study of the recovery of the unstressed orientational distribution as a function of temperature and time. The reorientation kinetics are given for a first order process by

$$n_j(t) - n_{j\mathrm{eq}} = [n_j(0) - n_{j\mathrm{eq}}] \exp\left(\frac{-t}{\tau}\right) \tag{3.6}$$

where $n_{j\mathrm{eq}}$ is the equilibrium value of n_j. Evaluation of the time constant τ allows the reorientation energy to be extracted from

$$\tau^{-1} = \nu_0 \exp\left(\frac{-U}{kT}\right) \tag{3.7}$$

where ν_0 is the attempt frequency.

3.2.6.2 Annealing experiments

It is particularly important in the case of irradiation defects to understand the annealing conditions necessary for observation. Not only does this information allow the distinction between primary and secondary irradiation products but can be used to support correlations with other defects.

Some defects undergo radical transitions as the temperature is varied. Vacancy defects, for example are known to reconstruct bonds resulting in a lower symmetry than ideal. At the sample temperature is raised however the EPR spectrum undergoes thermal broadening and narrowing until the spectrum reveals a higher symmetry. The apparent high symmetry is resultant from the rapid reorientation of the defect between orientations.

The changes observed in the spectrum reflect the relative frequency of the measurement and the thermally activated jumps of the defect.

3.2.6.3 Summary and other points

From the **g**-tensor anisotropy several quantities may be determined - defect symmetry, stress response tensor (**B**), reorientation kinetics and also the barrier to migration. The hyperfine interaction reveals information concerning the character (s or p-like) of the unpaired spin and the nuclei on which the unpaired electron density is localised. In particular the number of nuclei in each 'shell' where the shell refers to a system of equivalent nuclei can be found along with the proportion of the unpaired electron which is localised upon each nucleus. In cases where the unpaired spin is rather delocalised, the hyperfine interaction parameters may be unresolvable by EPR. In these cases electron double nuclear resonance (ENDOR) can be used.

It is also possible to determine the position of defect electrical levels to some extent in irradiated samples. For example, in boron doped silicon (10^{16} cm^{-3}), the Fermi level is pinned to the boron acceptor level which lies at $\mathrm{E}_v + 0.04$ eV. Heavy irradiation of this material brings the Fermi-level to around mid-gap. This phenomenon is due to the introduction of vacancies and interstitials which possess deep levels. If the irradiated sample is slowly annealed, much of the radiation damage is removed as interstitial–vacancy recombination occurs accompanied by recovery of the substitutional boron. As the Fermi-level position moves down towards the boron shallow acceptor level it crosses the electrical levels of some well characterised defect traps. Since these level positions are known, the approximate position of the Fermi-level can be tracked. When the spectrum of interest appears its level position can therefore be approximated.

3.3 Photoluminescence and absorption

Optical spectroscopy is a highly sensitive method used in defect characterisation being able to detect defect with concentrations as low as $\approx 10^{-12}$cm^{-3}.

An ideally pure semiconductor, with band gap energy, E_g will allow transmission of radiation with frequency $h\nu > E_g$. For other frequencies, the radiation will be absorbed in promoting electrons from the valence band to the conduction band. In practice, the presence of defects introduces electronic levels into the forbidden gap, which selectively absorb light with sub-band gap energy. A photoluminescence experiment involves the creation

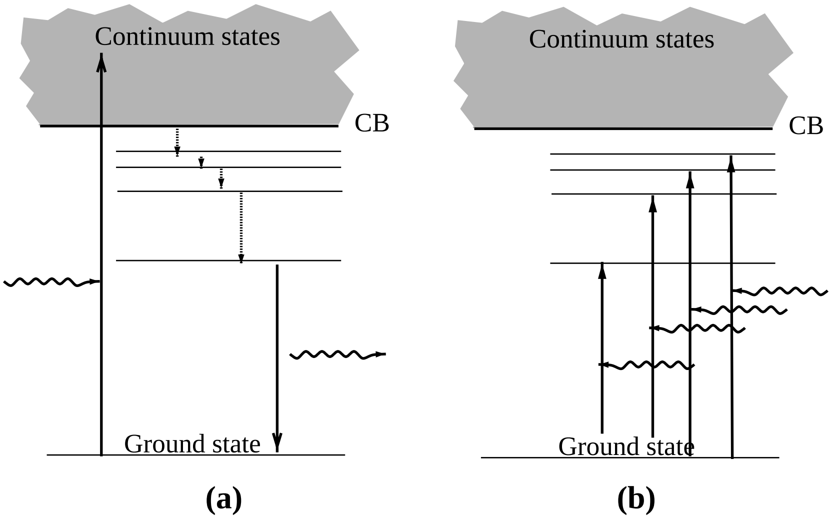

Figure 3.3: Mechanism for low-temperature luminescence and absorption. (a) Photoluminescence: Electrons are excited from the ground state into the conduction band where they rapidly relax non-radiatively through the continuum states and defect excited states before photon assisted electron-hole recombination occurs. (b) Absorption: Photon absorption occurs when the photon energy matches the transition energy for excitation.

of electron-hole pairs by illuminating the sample with above band-gap light (Fig 3.3(a)). The electrons undergo rapid thermalisation by radiative, or more probably, non-radiative mechanisms and relax into defect excited states. Electron-hole recombination then occurs resulting in the emission of a photon with energy equal to the energy difference between the excited and ground states. Because of the non-radiative relaxation of the electron to the lower excited states, photoluminescence is usually insensitive to excited states of higher energy. Absorption on the other hand detects these transitions provided that they are symmetry allowed. In an absorption experiment (Fig 3.3(b)), the sample is illuminated with a continuum of optical frequencies, and the transmitted spectrum is recorded. This relative simplicity of the processes involved in absorption allows the concentration of the luminescent centers to be measured. Since the photoluminescent signal is observed only following complex processes dependent upon temperature, capture cross-sections and electron phonon coupling, it is not usually possible to determine the defect concentration.

Other effects can be explained with reference to a configurational coordinate diagram (Fig 3.4). The ground state of a defect in charge state n possesses configurational coordinate Q. The adiabatic approximation gives the vibrational energy of the ground state:

$$E_g = (n + \frac{1}{2})\hbar\nu_g$$

where n is a quantum number and ν_g is some vibrational mode associated with the defect.

The excited state minimum possesses a different configurational coordinate reflecting the modified many-body wavefunction. Other excited states would be represented by additional parabolae. These are excluded for simplicity. The vibrational energies of the excited state are

$$E_e = (n + \frac{1}{2})\hbar\nu_e + E_0$$

The electron is first excited from the ground state into the excited state (A → B) before the lattice can respond (Frank-Condon principle). Subsequent lattice vibrations allow the excited state to reach its energy minimum (B → C). Here luminescence occurs (C → D). A second process of thermalisation allows the original ground state to be reached (D → A). The difference in energy between E_{abs} and E_{pl} is known as the *Stokes shift* and is related to the number of phonons involved in the process.

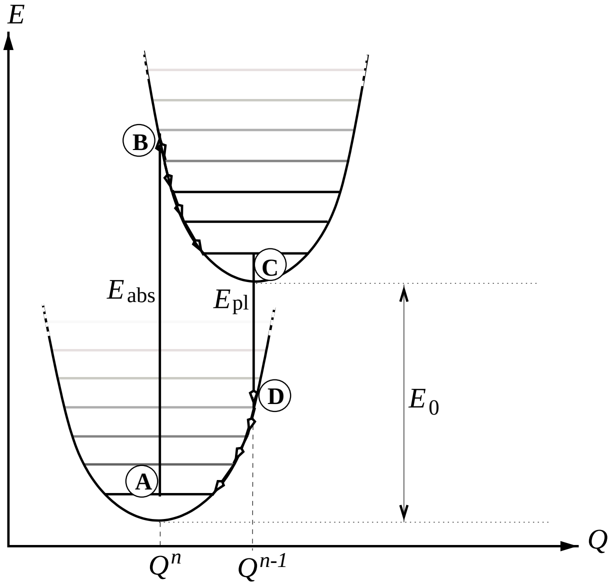

Figure 3.4: Configurational coordinate diagram showing absorption and luminescence processes.

The *zero-phonon* transition is observed when the overlap between the initial state ψ_i and final state ψ_f is large enough. The transition is disallowed, however, if the initial and final states do not satisfy the symmetry requirements set by the selection rules. This states that the product of the irreproducible representations Γ of the ground state, excited state and dipole operator must contain the totally symmetric irreducible representation Γ_{Symm}:

$$\Gamma_{GS} \otimes \Gamma_p \otimes \Gamma_{XS} \otimes \supset \Gamma_{Symm}$$

If a defect possesses localised vibrational modes, the zero-phonon line ZPL may be accompanied by phonon replicas which reflect the LVM structure. Important information can be determined concerning the identity of a luminescence center through the examination of local mode replicas. Isotopic shifts, for example, can relay important information as to the constituent atoms or bonding nature of the defect. Only a subset of the local modes may be observed as replicas to the ZPL either because they couple weakly to the transition or they are symmetry disallowed by the selection rules. The transition probability is proportional to the square of the matrix element:

$$\langle \psi_f \chi_0 | z | \psi_i \chi_1 \rangle$$

The selection rules are applied as for the simple dipole transition but now include the irreducible representation of the vibrational mode Γ_{LVM}:

$$\Gamma_{GS} \otimes \Gamma_p \otimes \Gamma_{XS} \otimes \Gamma_{LVM} \supset \Gamma_{Symm}$$

If the LVM is of A symmetry (i.e. is totally symmetric) then it can, in principle, couple to any dipole transition.

3.4 Deep level transient spectroscopy

A defect level lying in the bandgap with energy > 0.1 eV from either band edge is termed 'deep'. A deep trap of concentration N_T has a capture rate for electrons and holes, c_1, c_2 and an emission rate for electrons and holes e_1, e_2. The capture rate depends upon the defect capture cross section, the density of free carriers and the mean thermal velocity,

$$c_{i,n} = \sigma n_{i,c} \langle \nu^{\mathrm{th}} \rangle \tag{3.8}$$

where $i = 1, 2$ corresponding to electrons and holes respectively. The thermal emission rates are governed by Boltzmann statistics,

$$e_{i,n} = \sigma_{\mathrm{app}} N_D \langle \nu^{th} \rangle e^{\frac{-E_T}{kT}} \tag{3.9}$$

where σ_{app} is the apparent capture cross section and N_D is the effective density of states in the appropriate carrier band. E_T is the activation energy for the emission process. The steady state electron occupation of the trap is given by,

$$n_1 = \frac{c_1}{c_1 + c_2} N_T \qquad \text{and} \qquad n_1 = \frac{e_1}{e_1 + e_2} N_T \tag{3.10}$$

with a similar expression for the hole occupation.

DLTS studies allow determination of the electrical properties of deep level electron or hole traps with concentrations as low as 10^{12}cm^{-3}. By probing the space-charge variation of a Schottky barrier or $p - n$ diode with time and temperature, accurate measurements of the defect trap activation energy E_T, capture cross section σ and defect concentration N_T are made. Whilst the technique provides valuable information concerning the electrical nature of a defect, the bare DLTS experiment reveals no structural or composition information, making trap identification difficult.

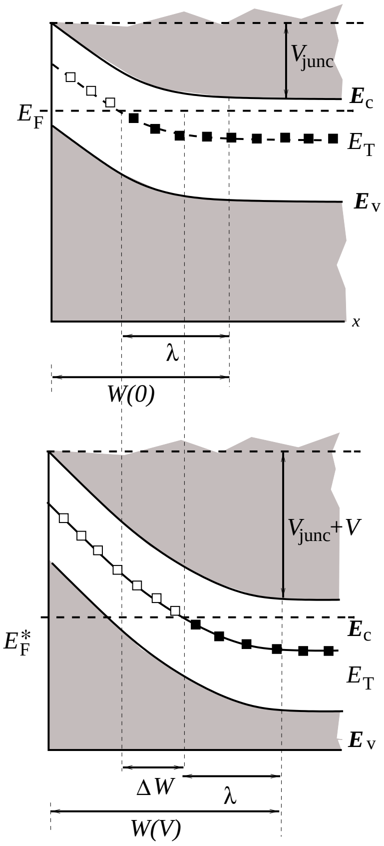

Figure 3.5: Steady state distribution of filled and empty traps in a $p^+ - n$ junction under zero bias (top) and reverse bias $V > V_{junc}$ (bottom). W represents the depletion region and λ is the transition region.

The energy level diagram of a $p^+ - n$ junction is shown in Fig 3.5. With no applied bias an equilibrium potential difference V_{junc} exists due to the diffusion of electron (holes) from the n to p type regions. A zone which is depleted of mobile charge carriers (labelled W in Fig. 3.5) exists straddling the interface.

When a reverse bias is applied the observable traps lie in the depletion region and the capture rate is zero. The trap occupation then depends only upon the thermal emission of carriers. The depletion region is flooded with carriers by a biasing pulse of the appropriate sign. Following an injection pulse of carriers the traps are rapidly filled and subsequently release carriers. The changing occupation of the traps during equilibration gives rise to a capacitance transient ΔC which can be detected. The decay of the capacitance transient is exponential:

$$\begin{aligned} \Delta C(t) &= C_2 - C(t) && (3.11) \\ &= \Delta C(0) e^{-t/\tau} && (3.12) \end{aligned}$$

where τ is the lifetime of the electron or hole in the trap $\frac{1}{\tau} = e_{i,n}$

Standard DLTS uses a rate window in which the transient is measured. Following the injection pulse the transient is measured at times t_1 and t_2. Since the transient is temperature dependent, both the sample temperature and the rate window is varied during the experiment. The variation of $C(t_1) - C(t_2)$ with temperature is measured as shown in Fig 3.6. The first step is to define a normalised signal $S(T)$ with respect to $\Delta C(0)$ – the change in capacitance due to a pulse at $T = 0$.

$$S(T) = [C(t_1) - C(t_2)]/\Delta C(0) \tag{3.13}$$

If the transients are assumed to be exponential this can be written,

$$S(t) = [\exp(-t_1/\tau)] - [\exp(-t_1/\tau)] = \exp(-t_1/\tau)[1 - \exp(-\Delta t\tau)] \tag{3.14}$$

where $\Delta t = t_2 - t_1$. The maximum in $C(t_1) - C(t_2)$ is given by

$$\frac{dS(T)}{d\tau} = 0 \rightarrow \tau_{\text{max}} = (t_1 - t_2)[\ln\left(\frac{t_1}{t_2}\right)]^{-1} \tag{3.15}$$

Hence the position of the maximum is dependent upon the rate window.

The trap concentration N_T can be estimated from the height of the capacitance transient. For the estimation to be valid the trap concentration must be much smaller than the donor/acceptor density. The capacitance of the $p-n$ junction when a bias V is applied is given as,

$$C_1 = A\left[\frac{\epsilon_r \epsilon_0 e}{2(V + V_{\text{junc}})}\right]^{1/2} \sqrt{N_D} \tag{3.16}$$

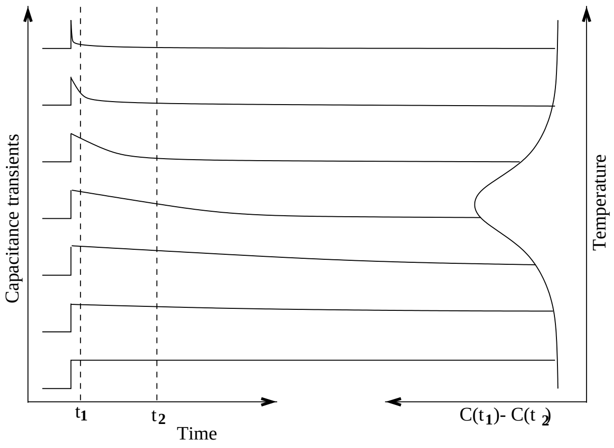

Figure 3.6: The temperature dependence of the capacitance transient for a given rate window.

where V_{junc} is the potential difference across the junction for no applied bias. Considering small changes in the capacitance, clearly we have

$$\frac{dC_1}{C_1} = \frac{1}{2}\frac{dN_D}{N_D} \tag{3.17}$$

Associating dC_1 with $\Delta C(0)$ and dN_D with N_T, this expression allows the approximation of the trap concentration,

$$N_T = \frac{2\Delta C(0) N_D}{C_1}. \tag{3.18}$$

By varying the temperature and measuring the thermal emission rate of the trap, the position of the level in the gap can be estimated (Eq. 3.9). The method employed does not take the temperature dependence of the density of states ($N_d \propto T^{3/2}$) and the thermal velocity of the carriers ($v \propto T^{1/2}$). An Arrhenious plot is generated of the form

$$ln\left(\frac{e_i}{T^2}\right) \quad \text{v} \quad \frac{1000}{T} \tag{3.19}$$

The trap activation energy can then be determined from

$$ln\left(\frac{e_i}{T^2}\right) = \chi - \frac{E_T}{kT} \tag{3.20}$$

where χ is a constant related to the capture cross section. Quoted values of the trap energy often include this χ term giving systematic errors of around 0.01-0.04 eV. The method is generally accurate to within a few percent.

3.5 Local vibrational mode spectroscopy

The introduction of a point defect into the pure crystal modifies the normal modes of vibration in one of two ways: (i) The modification occurs within the bulk modes and these modified vibrations couple strongly to the lattice and hence are highly delocalised (ii) New modes with frequencies greater than the maximum lattice frequency ($\omega_{\max}$) appear. Because these high frequency vibrations are not supported by the pure crystal they are localised upon the defect. Such modes are labelled *local vibrational modes* (LVMs).

For impurity defects, the type of normal mode that is introduced depends upon the impurity mass relative to the host atom mass and the strength of the force constants involved in bonding the impurity into the lattice. Carbon is a good example of an impurity which introduces localised vibrational modes into the phonon spectrum of Si. Carbon is an atom with 3/7 the mass of Si which makes a bond with Si which is ~ 40 % stronger than the Si–Si bond strength.

For intrinsic defects the situation is similar. It is well known that the dangling bonds associated with vacancy defect interact across the vacancy to form weak "reconstructed" bonds. The resulting tensile strain in the surrounding lattice weakens the nearby Si-Si bonds and so no vibrations can arise above $\omega_{\max}$. If an extra Si is introduced into the lattice however, this will induce compressive strain leading to strengthened bonds and hence supporting vibrations with frequencies greater than $\omega_{\max}$.

The local modes of a defect can be classified in terms of their symmetry. The normal coordinate Q_Γ describes the atomic motion of the atoms involved in each mode Γ. The highest possible LVM symmetry is the point group symmetry of the defect and these modes are labelled A (breathing) modes. The symmetry of a mode depends upon which of the symmetry operations of the defect point group are broken during the vibrational cycle.

At low temperatures, before any transition occurs the defect is in a total-symmetric ground state Ψ_i. Immediately after the transition the state is labelled Ψ_f. Ψ_f is an excited state with symmetry Γ. The probability of a photon coupling to a phonon as given by the electric-dipole approximation is proportional to,

$$|\langle\Psi_i|\mathbf{P}|\Psi_f\rangle|^2 \tag{3.21}$$

where P is coupling of the electric polarization vector of the incident radiation with the electric dipole moment of the final state.

The local vibrational mode is therefore infra-red active only when it induces an electric dipole. If the dipole moment of the equilibrium position is labelled P_e then the induced dipole for small displacements U along a normal coordinate is written,

$$P = P_e + \left(\frac{dP}{dU}\right)_e U + \left(\frac{d^2P}{dU^2}\right)_e \frac{U^2}{2} + ... \tag{3.22}$$

Thus Eq. 3.21 shows that the equilibrium dipole P_e does not couple to the vibrational states. For a single phonon process the coupling intensity is proportional to $[\left(\frac{dP}{dU}\right)_e]^2$. This means that the apparent charge $\mu = \left(\frac{dP}{dU}\right)_e$ can be deduced experimentally.

The integrated absorption for a local vibrational mode is given by

$$I = \int \alpha(\omega) d\omega = \frac{2\pi^2 \rho \eta^2}{ncM} \tag{3.23}$$

where M and ρ are the mass and concentration of the defect.

Chapter 4

Determination of experimental observables

4.1 Introduction

This chapter is intended to summarise and explain the calculation methods employed later in the thesis. The majority of the methods can be explained through the use of a special case study – the carbon interstitial (C_i) in silicon. This defect is particularly unusual because it has been characterised by the four main experimental techniques applied to point defects: EPR, DLTS, IR and PL. It has also been well investigated by theory and in some cases the results of the AIMPRO calculations are compared with other theoretical calculations.

4.2 Experimental background

Carbon exists as an impurity in Si with a concentration rarely below 10^{14} cm^{-3}. The importance of C has ensured that C related defects have received much attention from both experimentalists and theorists.

Substitutional carbon, C_s was first identified in silicon in the 1960's [26, 27] when it was shown to be responsible for a LVM at 607 cm^{-1}. Irradiation of silicon produces self-interstitials (Si_i) which migrate rapidly and bind to substitutional carbon to form the C_i complex. The first identification of C_i was made using infra-red spectroscopy [28]. Two local vibrational modes are observed at 960 and 936 cm^{-1} which anneal in just as the 607 cm^{-1} mode, due to C_s, disappears. Later work [29] correlated an EPR spectrum observed in irradiated *p*-type Si labelled G12 with the LVMs at 960 and 936 cm^{-1}. G12 has C_{2v} symmetry with the principal axis along $\langle 001 \rangle$. The hyperfine interaction of the unpaired spin showed that it possessed p-like character with 36% localisation on a unique carbon atom. The spectrum was identified with the positive charge state of the carbon interstitial, $\mathrm{C_i^+}$. Stress alignment studies were performed to extract the B tensor and the reorientation barrier, evaluated at 0.88 eV. Isochronal annealing of G12 showed that heating the sample to 65 °C for 30 minutes removes the spectrum. This annealing temperature is consistent with that of the LVMs and also of a hole trap at E_v+0.28 eV observed in DLTS [30].

More recently, studies [31] of irradiated n-type material correlated the L6 EPR spectrum (C_{2v} symmetry) with an acceptor level measured by DLTS at E_c-0.10 eV. The L6 centre has similar B tensor, annealing range and reorientation barrier (0.77 eV) to G12. In contrast to the G12 EPR centre, no hyperfine splitting due to the presence of C or Si isotopes was observed. The lack of observable hyperfine interaction could be explained if the wavefunction is relatively delocalised and has a small overlap with the carbon atom.

Photoluminescence experiments also detect a signal arising from $\mathrm{C_i}$ [32, 33]. The 856 meV line also has C_{2v} symmetry and corresponds to the neutral charge state of the defect. The activation energy [33] to migration was found to be 0.87 eV, similar to that found for the charged species.

Through consideration of the EPR symmetry and unpaired wavefunction the structure of $\mathrm{C_i}$ has been shown to exist in a $\langle 001 \rangle$ split configuration with a C and Si atom sharing a lattice site. Unambiguous confirmation that the neutral species also possesses this structure came from uniaxial stress measurements of the PL line [32] and the 902 and 931 cm^{-1} LVMs [34].

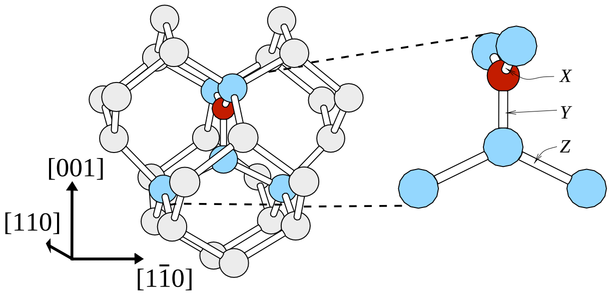

Figure 4.1: Structure of the carbon interstitial in silicon. The lengths of the labelled bonds are given in Table 4.1.

4.3 Calculations

We analyse the C_i defect using both cluster-based (AIMPRO [35]) and supercell methods. Two clusters were employed with configuration $C_1Si_{70}H_{60}$ and $C_1Si_{181}H_{116}$ and one supercell, configuration C_1Si_{64}. The vibrational modes are calculated using the supercell and are compared with previous AIMPRO calculations which used a $C_1Si_{35}H_{36}$ cluster. [2].

In the clusters, the wave-function fitting basis consists of independent s and p Gaussian orbitals with four different exponents, placed at each Si site. A fixed linear combination of two Gaussian orbitals are sited on the terminating H atoms. In addition, s and p orbitals are placed at each Si–Si bond centre to ensure good description of the Kohn-Sham states. The charge density is fitted with four independent Gaussian functions with different widths on each Si atom and three on the terminating H atoms. One extra Gaussian function is placed at each Si–Si bond centre. In the supercell, the wave-function fitting method is the same as that for the cluster. The charge density is fitted with a plane-wave basis using a cut-off energy of 40 a.u.

4.4 Structure

The optimised structure of the neutral defect is shown in Fig. 4.1. C_i was optimised in all three charge states and the bond lengths at the defect core are given in Table 4.1. There is a small dependence of the structure of C_i with charge state. Most of the calculated values from different methods agree to within $\sim 3\%$. The small differences between the bondlengths calculated in the small and large clusters/supercells demonstrate that the calculated structures are reasonably converged with respect to the system size.

4.5 Vibrational modes

The calculation of vibrational modes can provide quite accurate and valuable information for comparison with experiment. In Chapter 5, for example, a number of vibrational modes arising from vacancy-hydrogen defects in germanium are calculated using the cluster method and compared with experiment. The theoretical data can give considerable help to an experimentalist in identifying hydrogen-related peaks in the infra-red.

The vibrational modes for C_i have been evaluated here using the supercell method [36] and the results of previous cluster calculations [2] are also given. The first step is to optimise the defect cluster or supercell until the forces are zero. The energy-double

		Method (No. of Si atoms)				
Charge state	Bond	C (35) [2]	C (70)	C (181)	S (32) [1]	S (64)
-	X	-	1.83	1.79	-	1.78
	Y	-	1.75	1.77	-	1.74
	Z	-	2.26	2.24	-	2.26
0	X	1.82	1.88	1.82	1.80	1.80
	Y	1.73	1.70	1.71	1.77	1.73
	Z	2.30	2.29	2.25	2.22	2.26
+	X	-	1.93	1.86	-	1.78
	Y	-	1.74	1.77	-	1.74
	Z	-	2.28	2.26	-	2.25

Table 4.1: Bondlengths (Å) of C_i evaluated using cluster and supercell approaches. Also shown for the neutral charge state are the results of *ab initio* calculations of Capaz *et al* [1]. C denotes cluster calculations and S denotes supercell.

derivatives of each atom in the system must now be found. This involves moving each atom, along axis l by a distance ϵ (usually chosen to be 0.025 a.u.), recalculating the self-consistent charge density, and finding the new forces. Say, atom A is displaced along l. Atom B now feels a force along direction m of $f^+_{m,B}(l,A)$. Atom A is then moved a distance $-\epsilon$ along l from its equilibrium position and a new force $f^-_{m,B}(l,A)$ is found. The three points are used to determine the energy second derivatives to second order in ϵ:

$$D_{l,A,m,B} = \frac{f^+_{m,B}(l,A) - f^-_{m,B}(l,A)}{2\epsilon} \tag{4.1}$$

Diagonalisation of the complete dynamical matrix allows the eigenvalues of the vibrational modes to be determined. Since the displacement, ϵ is finite, this method includes some contribution from all even powers of ϵ not just the quadratic term and so some anharmonicity is included. For this reason the calculated frequencies are termed *quasi-harmonic*.

In practise it is not necessary to calculate the energy double derivatives for all the atoms within the system. Only those atoms close to the defect core lie in a potential well which is significantly different from that of a bulk atom. For bulk-like atoms away from the core then, the Musgrave-Pople valence-force potential [37] can be used.

From the optimised $\mathrm{C_i}$ in the 64 atom supercell, the energy double derivatives were calculated explicitly for the six atoms in the defect core (see Fig. 4.1). Using the Musgrave-Pople potential to simulate the potential energy surface for the remaining bulk-like atoms of the supercell the vibrational modes are calculated. Three modes are calculated to lie above the Raman frequency with frequencies 554 and 936, 960 cm^{-1}.

	B_1			A_1		
	^{12}C	^{13}C	^{14}C	^{12}C	^{13}C	^{14}C
Experiment (77 K)	930	26	49	921	29	54
Supercell	960	31	58	936	27	50
Cluster	867	28	52	922	28	52

Table 4.2: LVMs (cm^{-1}) of $\mathrm{C_i}$ in silicon calculated using the supercell and cluster method compared with experiment. The isotopic shifts of the LVMs with ^{13}C and ^{14}C are also shown.

The two higher modes have symmetry B_1 and A_1. The B_1 mode involves a swinging motion of the carbon atom between the two equivalent Si atom to which it is bonded. The A_1 mode consists of stretching motion of bond Y (see Fig. 4.1). The mode symmetries confirm the experimental assignments and the frequencies are within 3% of the experimental values (Table 4.2). The isotopic shifts of both modes upon replacement of the carbon atom with ^{13}C and ^{14}C have also been evaluated by experiment. The calculated values are also found to agree well with experiment.

Calculations employing a cluster with configuration $\mathrm{C_1Si_{35}H_{36}}$ give reasonable results. The A_1 mode is calculated to have a frequency and isotopic shifts very close to experiment. The calculated frequency of the B_1 mode however is about 7% lower than that observed so that it lies below the A_1 mode. The isotopic shifts of this mode are found to agree well.

These calculated values are quite typical of AIMPRO results. Vibrational mode frequencies calculated using the cluster method may differ by as much as 10% from experiment but the isotopic shifts are usually found to agree well. The supercell approach generally results in slightly more accurate determination of vibrational frequencies.

4.6 Migration paths and diffusion barriers

4.6.1 Methods

In order to calculate a migration path three techniques are employed which allow the user to constrain the system in order to force the defect away from its ground state configuration. The different methods are applied to systems of differing complexity.

For a simple diffusion process where the saddle point position for the diffusion step is known one can take advantage of point group symmetry. Take for example VH in silicon. In this case there are four Si atoms surrounding a vacant site. Two of the unsatisfied bonds reconstruct, one is saturated by the H atom leaving a single dangling bond remaining. At some finite temperature the H atom gains enough thermal energy to hop over to the dangling bond. This diffusion step has a saddle point corresponding to the configuration where the H atom is sited intermediate between two dangling bond atoms. The symmetry of this configuration is C_{2v}. The diffusion barrier may be calculated by taking the difference between the total energies of the optimised ground state and the optimised saddle point. Optimisation of the saddle point is made possible by constraining the symmetry to C_{2v}.

A more sophisticated way to find the migration barrier is necessary for those cases where the saddle point is unknown. The first of these is the *orthogonal relaxation* method. The vector displacement of all equivalent atoms from the initial atomic configuration, $\mathbf{R}_i^1$ to the final structures $\mathbf{R}_i^2$ of the diffusion path is found, $\mathbf{v}_i = \mathbf{R}_i^1 - \mathbf{R}_i^2$. All atoms are shifted by a fraction α along vector $\mathbf{v}_i$. From this positions the atoms are allowed to relax from these intermediate positions *only in directions orthogonal to* $\mathbf{v}_i$. Stepping α from 0 to 1 allows the diffusion path and energy to be mapped.

The third method uses a constraint on the relative bond lengths between specified atoms. For each constraint imposed, three atoms are included, say atom A, B and C. The relative bond lengths between atoms A and B ($|\mathbf{R}_A - \mathbf{R}_B|$) and atoms A and C ($|\mathbf{R}_A - \mathbf{R}_C|$) are constrained such that,

$$x = |\mathbf{R}_A - \mathbf{R}_B|^2 - |\mathbf{R}_A - \mathbf{R}_C|^2 = \mathit{constant} \tag{4.2}$$

This method is typically used when atom A is the diffusing atom, breaking a bond with atom B and subsequently making a bond with atom C during the diffusion. For more complex diffusion paths, a number of bondlength constraints may be applied.

4.6.2 Diffusion of $\mathrm{C_i}$

The migration barrier has been found experimentally to be 0.87-0.88 eV irrespective of charge state. The determination of a reorientation barrier for the L6 and G12 defect with a similar energy (0.78 eV) suggests that the migration path and reorientation occur simultaneously.

Previous calculations [1] have determined the activation energies for two diffusion paths indicated in Fig. 4.2. At the midpoint of diffusion path 1, the diffusing C atom lies at a bond-centred position. The complete diffusion step results in a 180° reorientation of the defect. The energy barrier to diffusion along this path has been calculated to be 2.5 eV using a 32 atom supercell [1] and 1.1 eV using a $C_1Si_{35}H_{36}$ cluster [2]. Path 2 is markedly different from path 1 with a midpoint configuration which has C_2 symmetry. This path explains the small difference between the observed reorientation and diffusion barrier as the defect principal axis reorients during each diffusion step. Capaz *et al* calculated the barrier to migration along this path to be 0.51 eV, in reasonable agreement with experiment but the cluster results gave a value of 1.1 eV.

The different calculations give quite different results. It is often the case that the cluster method overestimates diffusion barriers whilst the supercell approach tends to underestimate barriers. Calculations of oxygen diffusion clearly follow this trend [38]. Recent results [39] for the diffusion of isolated oxygen in silicon give values of 2.2 and 2.8 eV using supercell and cluster AIMPRO respectively (cf Exp: 2.53 eV).

4.7 Stress response

The stress response tensor (B) of a defect, described in Chapter 3 is calculated using the supercell approach in the following way. The defect is first optimised in a number of supercells with different lattice parameters, typically within 0.2 – 0.4 % of the ideal lattice parameter. The total energies of the supercell are fitted to a parabola to find the equilibrium lattice constant shown in Fig. 4.3 for the C_i defect. In this case we find the equilibrium lattice expansion to be 0.33%. This expansion lies at the higher end of those found for oxygen related defects [39] and but is expected for the $\mathrm{C_i}$ where the extra atom is incorporated into the lattice forming strong bonds with its neighbours. From this equilibrium volume, a uniaxial strain or shear is applied. The number of different stresses or shears which need to be applied in order to evaluate all the tensor elements depends upon the defect symmetry. In the case of the $\mathrm{C_i}$ with C_{2v} symmetry, the strain must be

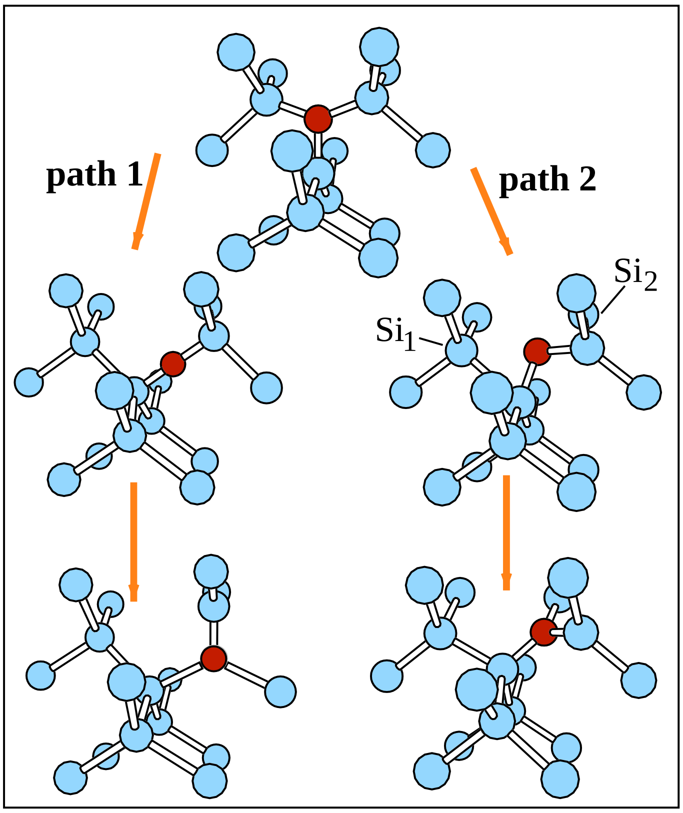

Figure 4.2: Possible migration paths of C_i. Path 1 has a saddle point for diffusion at the bond-centred site. The saddle point for path 2 has C_2 symmetry.

applied along two separate directions.

Path	Supercell (Capaz *et al*) [1]	Cluster AIMPRO) [2]
1	2.5	1.10
2	0.51	1.10

Table 4.3: Theoretical values (eV) for the activation barrier to diffusion of neutral $\mathrm{C_i}$ along two migration paths, labelled 1 and 2 (see Fig. 4.2).

The B-tensor was calculated for the neutral charge state of $\mathrm{C_i}$. It is compared with the experimental values extracted from the stress response of the G12 and L6 EPR centres in Table **??**. In general we would expect the stress response of a defect to depend upon the charge state. The experimental values of the positive and negative charge states of $\mathrm{C_i}$ however, show that the stress response is quite insensitive to charge state. The directions of the tensor elements are shown in Fig. 4.4. The principal element of the B-tensor,

B_3 has a negative sign reflecting the tensile nature of the defect along its principal axis. The B_1 tensor element is much larger than B_2. Since B_1 lies along the axis containing a large component of the two equivalent C–Si bonds it is probable that this reflects the sensitivity of these bonds to compression. The calculated values of the principal tensor elements shown in Table 4.4 are accurate to around 20%. This is typical of the accuracy of these calculations.

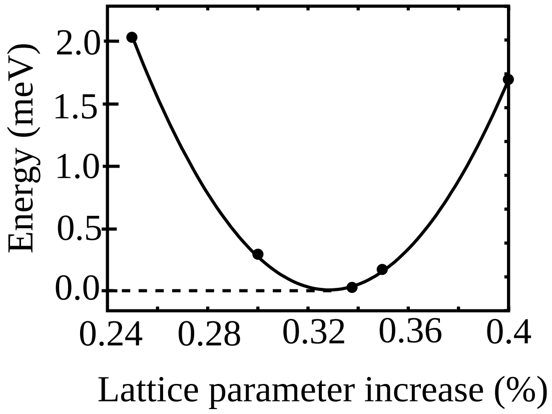

Figure 4.3: Total energy differences of the C_i defect in the supercell for various values of the lattice parameter, a_0.

element	Calc(0)	L6(-)	G12(+)
B_1	9.0	7.4	7.3
B_2	0.9	-0.2	0.3
B_3	-9.6	-7.2	-7.6

Table 4.4: Calculated and experimentally determined B-tensor elements (eV) of the carbon interstitial.

4.8 Electronic structure

The Kohn-Sham eigenvalue spectrum for the three charge states of C_i is shown in Fig. 4.5. The neutral defect possesses two deep one-electron levels which arise from the two p-orbitals in the defect, one associated with the three-fold coordinated C atom, the other with the three-fold coordinated Si atom. The lower of the two levels arises from the

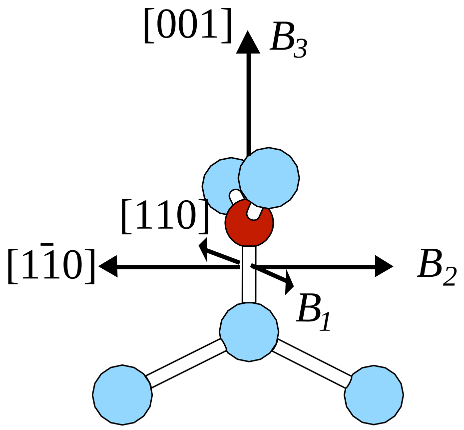

Figure 4.4: Directions of B-tensor elements of the carbon interstitial in silicon.

carbon orbital reflecting the higher electronegativity of C than Si. The addition or extraction of one electron from the neutral defect results in a shift of the Kohn-Sham levels. The electronic wavefunction corresponding to the unpaired spins of $\mathrm{C_i^-}$ and $\mathrm{C_i^+}$ can be compared with the data extracted from the hyperfine satellites of the EPR centres L6 and G12.

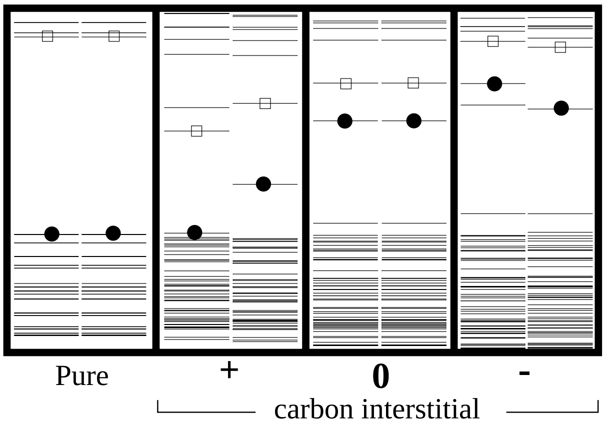

Figure 4.5: Kohn-Sham levels of the carbon interstitial in silicon. Left: eigenspectrum of a pure 131 atom cluster. Right: spin up and down eigenspectra of the carbon interstitial in three charge states. The valence band edges have been aligned. The highest occupied and lowest unoccupied levels are indicated by filled circles and empty squares respectively.

The electronic distribution of the unpaired electron in both the positive and negative charge states is shown in Fig. 4.6. Clearly, the experimental evidence that the unpaired electrons in each charge state occupy different orbitals is reproduced. The two orbitals possess B_1 and B_2 symmetry. Performing a Mulliken analysis calculation allows the

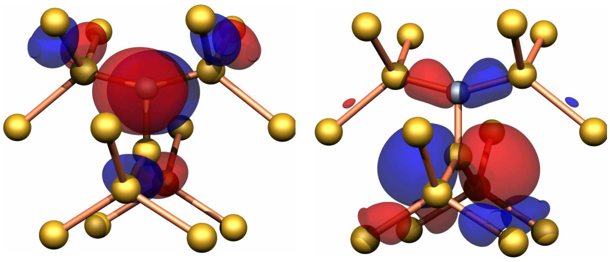

Figure 4.6: Isosurface plot of the unpaired wavefunction of $\mathrm{C_i^+}$ (left) and $\mathrm{C_i^-}$ (right).

calculated Kohn-Sham wavefunction to be compared with the results of EPR experiments. This approach characterises the wavefunction by estimating the amount of a wavefunction accounted for by each Gaussian fitting function. In this way the localisation on each atom (and bond-centred function, if applicable) is estimated and also the $s:p$ character of the wavefunction can be estimated. For the case of $\mathrm{C_i^+}$ around 30% of the spin is localised on the C atom in good agreement with experiment (36%). This wavefunction at the C atom is purely p-like. The unresolved hyperfine interaction of the unpaired electron of $\mathrm{C_i^+}$ (G12) with 6 - 8 Si atoms is consistent with the calculations which show up to $\sim 4\%$ amplitude on second shell atom sites. In the negative charge state the calculation shows 30% of the unpaired wavefunction is localised in a p-orbital on the unique Si atom. The Mulliken analysis shows that the remaining portion of the unpaired spin is slightly more delocalised than for the positive charge state. The more distributed nature of the unpaired spin for the negative charge state may explain the lack of observed hyperfine splitting with ^{13}C or ^{29}Si in outer shells in the L6 EPR spectrum. However, from the calculated localisation we would expect to observe hyperfine interaction with the unique Si nucleus in the negative charge state and so it is unclear why this is not observed.

4.8.1 Calculation of electrical levels

The method used in this thesis to estimate the positions of the donor/acceptor levels includes an empirical correction. This technique involves a cluster calculation of the energy required to add electrons to (electron affinity) or extract electrons from (ionisation energy) a defect. This energy is then compared with that for a defect with *known* electrical levels. The method has been used to characterise the electronic structures of transition-metal hydrogen complexes in Si [40] resulting in errors of around 0.2 eV.

The electrical levels of a defect correspond to the positions of the Fermi-energy at which a charge state change occurs. The trap type is characterised in terms of the defect charge state when the trap is filled and when it is emptied. Hence a simple donor level is denoted (0/+) and the acceptor levels is denoted (-/0).

The donor level is defined as the energy difference of the defect when a hole is promoted to the defect level from the valence band, E_v

$$E_{\text{tot}}[E_d(0), E_v(h)] - E_{\text{tot}}[E_d(h), E_v(o)] \tag{4.3}$$

The acceptor level is defined similarly. It is the difference in energy of the defect (a) when an additional electron is inserted into the conduction band at E_c electron and (b) when this electron occupies the lowest empty defect level:

$$E_{\text{tot}}[E_d(e), E_c(0)] - E_{\text{tot}}[E_d(0), E_c(e)] \tag{4.4}$$

Alternatively, the donor level is the difference between the ionisation energy of the defect and that of bulk Si. In cases where the defect wavefunction is enclosed by the cluster and does not interact with the cluster surface the ionisation energy can, in principle, be calculated. The cluster method, however, cannot be used to compute the ionisation energy of bulk Si because the valence electron wavefunctions are delocalised and interact with the surface. The method employed in this thesis circumvents this problem by including an empirical correction. The ionisation energy, I of two defects, say defect A and defect B is calculated. A is the defect for which we wish to evaluate the donor level and defect B is a defect with a known donor level position, $E(0/+)_B$. The position of the donor level of defect A can be easily evaluated,

$$E(0/+)_B = E(0/+)_A + I_B - I_A \tag{4.5}$$

The acceptor level is found in a similar fashion, this time using the difference in electron affinities to determine the difference in acceptor level positions.

Defect B should ideally be a well characterised defect, with well characterised levels. Additionally, the defect structure should be relatively insensitive to calculation details making routine calculation unproblematic. We usually take the carbon interstitial as the marker defect as it possesses both an acceptor and a donor level and fulfils the above criteria. For the purposes of demonstration we calculate here the $\mathrm{C_i}$ donor and acceptor levels using substitutional gold as the marker defect. The Au_s defect possesses a donor and acceptor level at $\mathrm{E}_v + 0.35$ and $\mathrm{E}_c - 0.56$eV respectively [41, 42, 43]. The calculated and experimental electrical levels are within 0.2 eV of each other (see Table 4.5).

	(0/+)	(-/0)
Au_s	Exp: $\mathrm{E}_v + 0.35$	Exp: $\mathrm{E}_c - 0.56$
C_i	Exp: $\mathrm{E}_v + 0.28$	Exp: $\mathrm{E}_c - 0.1$
C_i	Calc: $\mathrm{E}_v + 0.42$	Calc: $\mathrm{E}_c - 0.01$

Table 4.5: Electrical levels of substitutional gold and the carbon interstitial. The calculated C_i levels are also shown.

4.9 Summary

In summary, the cluster and supercell calculations can be used to predict a number of observables. Using the carbon interstitial as a case study, the structural, electronic and vibrational characteristics of the defect have been calculated and compared with experiment. Good accuracy is achieved for the calculation of vibrational modes. The stress response tensor is calculated to be within $\sim 20\%$ of the values determined from EPR stress studies. A semi-empirical method is employed to find the electrical levels of defects. This has been demonstrated to give an accuracy of around ±0.2 eV [40]. The Kohn-Sham wavefunction can often be used, together with Mulliken analysis of the wavefunction localisation and *s*:*p* ratio in order to compare the calculation results with hyperfine data associated with paramagnetic defects.

Chapter 5

Vacancy-hydrogen defects in germanium

5.1 Introduction

This chapter concerns the investigation of the isolated vacancy in germanium and its complexes with hydrogen. This work follows extensive studies into the same problem in silicon. We first briefly review the situation in silicon and then consider the germanium problem.

The introduction of hydrogen to silicon is difficult to avoid. Common device processing and operation stages inevitably allow H into samples [44]. The demonstration of the passivating effects of H on shallow acceptors in both Si [45, 46] and Ge [47] marked the beginning of a rapid development of our knowledge of H defects in Si. However, although deep centres such as the vacancy are strong traps for hydrogen [48, 49, 50] only relatively recently has the detailed interaction of H with the vacancy been studied.

The structure and vibrational properties of vacancy-hydrogen complexes in silicon have been systematically investigated by several experimental methods. VH_n $(n = 1, 2, 3, 4)$ complexes in Si have been studied using optical detection of magnetic resonance (ODMR) [51], EPR [52, 53] and IR [54, 50]. The systematic IR and EPR investigations of the complexes of hydrogen with native defects in silicon have provided conclusive identifications of many fundamental centres. Using isotopic substitution and annealing techniques the IR signals corresponding to Si-H stretch modes of H_2^* [55], VH_2, VH_3, VH_4 and $\mathrm{V}_2\mathrm{H}_6$ have been assigned [56]. The assignment of two stretch modes at 2191 and 2166 cm^{-1} was initially made to VH_3 [57, 58]. However, further annealing studies by the same group [59] show that the EPR signal corresponding to VH_3 anneals out at $\sim$ 500 K, the temperature at which the 2191 and 2166 cm^{-1} LVMs first appear. Moreover, these IR lines show a greater thermal stability than those attributed to VH_4. Therefore these stretch modes were reassigned to V_2H_6. Another pair of stretch modes at 2185 and 2155 cm^{-1} have since been ascribed to VH_3 [60]. Theoretical investigations of mono-vacancy-hydrogen complexes in silicon have employed CNDDO [61], tight-binding theory [62, 10], Hartree Fock [10] and density functional theory (DFT) [63, 48, 64].

The extraction of an atom from a crystal with the diamond structure results in a defect with T_d symmetry with four dangling bond orbitals. In silicon, it is well known that the vacancy undergoes a strong Jahn-Teller distortion effected by the reconstruction of the dangling bonds. The reconstructed bonds give rise to deep levels which, when occupied by unpaired electrons, give rise to centres visible by EPR. As hydrogen atoms are added to the vacancy, they break the reconstructions and bond to the Si atoms (see Fig. 5.1). When four H atoms are present, all the dangling bonds are eliminated and the defect possesses no gap states.

Variation of temperature reveals that VH in Si undergoes a change in symmetry above $\sim$ 60K [53] from C_{1h} to C_{3v}. The explanation for the symmetry change is that the reconstruction across the vacancy reorients rapidly between pairs of atoms. This thermally activated reorientation is consistent with a similar effect observed in the silicon divacancy, V_2 [11] between 40 and 100 K. The VH EPR signal broadens and disappears above 200 K indicating a further increase in symmetry possibly due to rapid reorientation of the H atom around the vacancy, before the defect anneals out.

Until recently, the situation in germanium has been less clear. Hydrogen forms covalent bonds with Ge with a strength of 3.6 eV [65] in molecular compounds compared with a Ge-Ge dissociation energy of 1.93 eV [66]. In comparison with silicon systems (3.92 [65] and 2.32 eV [66] respectively) then we would expect largely similar behaviour. However, some of the few available comparisons of H in Si and Ge suggest otherwise. For example, whilst the passivation of shallow centres by H in silicon is almost complete, in germanium the passivation is only partial [44]. The motivation for the study of the passivation of deep centres in germanium is clearly strong particularly with the recent interest in $Si_{1-x}Ge_x$ technology.

Only one systematic study of VH_n in Ge has been performed to date [67, 56]. Float-zone refined Si was implanted with protons or deuterons at low temperature (30 K). The spectra were measured at various temperatures from 77 K up to around 500 K. The use

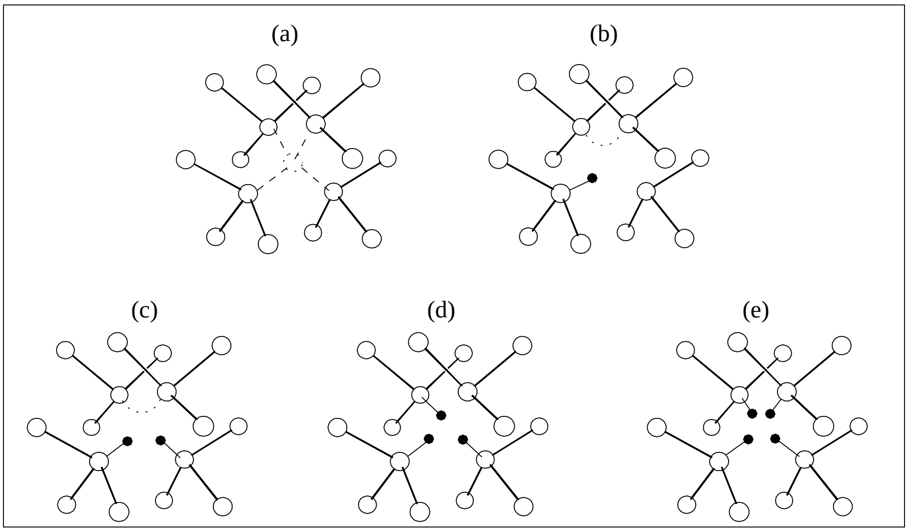

Figure 5.1: Vacancy-hydrogen structures in germanium. Reconstructed bonds are indicated by the dashed lines.

of the hydrogen isotope substantially assists the identifications of IR absorption peaks with defects. In particular, the isotopic splittings can reveal the number of equivalent hydrogens involved in the vibrations.

The relative frequencies of the vibrational stretch modes of the VH_n, $n = 2, 4$ and V_2H_6 defects in germanium were observed to be very similar to those identified in silicon with a constant factor mapping stretch frequencies onto their counterparts in Ge. The vibrational modes for VH have not yet been observed. There has been some doubt as to the assignment of the stretch modes to V_2H_6. It is uncertain whether these modes arise from VH_3 or V_2H_6. As found in silicon, the annealing data demonstrates that these modes arise from a defect which is thermally more stable than VH_4 supporting their identification with V_2H_6 [56].

5.2 Calculation method

The calculations were performed using tetrahedral clusters with configuration $Ge_{70}H_{60+n}$. The basis set consisted of N s, p orbitals on the germanium and hydrogen atoms. The charge density on each atom was fitted to M Gaussian functions. The values for N and M were C(4,4) and H(2,3). Extra Gaussian functions were placed at bond centered sites of Ge–Ge bonds and also on Ge–H bonds at the defect core. Two exponents were used to fit the charge density at the bond centred sites and one exponent to fit the wavefunction.

In order to induce the reconstruction of dangling bonds expected for V, VH, VH_2 a pre-relaxation was employed. This entailed moving the atoms to be paired towards each other from their ideal lattice sites and subsequently moving the surrounding atoms to restore all bondlengths to normal. All the atoms in the cluster were then optimised. The inclusion of surface relaxation allows a strong reconstruction of the vacancy dangling bonds. This is because the tensile strain which arises at the core due to reconstruction is somewhat relieved by movement of the surface atoms during relaxation. To calculate the vibrational modes, the energy second derivatives were found for the four Ge atoms at the defect core and the H atoms in the vacancy.

5.3 Results

We now consider the structural, vibrational and electronic properties of the vacancy and vacancy hydrogen complexes separately.

5.3.1 Structures

The isolated neutral vacancy in germanium was optimised to obtain a measure of the strength of bond reconstruction. The defect was relaxed from a structure with strongly reconstructed bonds (2.50 Å) with symmetry constrained to D_{2d}. The optimised structure has reconstructed bondlengths of 2.83 Å (cf. bulk Ge–Ge value of 2.45 Å). Initial conditions involving a reconstructed bond of 3.24 Å gave rise to a reconstructed bond length of 2.81 Å demonstrating that the final reconstructed bond length is not highly sensitive to the initial atomic positions.

Neutral VH possesses C_{1h} symmetry with a reconstructed bond length of 2.78 Å. The region of high electron density repels the H atom so that the Ge-H bond moves 5.6° out of the [111] axis. The Ge-H bond was found to be 1.541 Å (cf 1.52 Å in molecular GeH_4). The optimised VH_2 defect has C_{2v} symmetry with a reconstructed bondlength of 2.79 Å. The effect of the additional H atom in the defect results in a slight shortening of the Ge-H bond to 1.531 Å. VH_3 was assumed to have C_{3v} symmetry. The defect then has three equivalent atoms each with a Ge-H bondlength of 1.536 Å. The angle made between the Ge-H bond and the $\langle 111 \rangle$ directions was 4.8°. VH_4 has four equivalent Ge-H bonds (T_d symmetry) of length 1.526 Å. The Ge atoms move away from their positions in the relaxed ideal vacancy by 0.32 Å giving an increase in volume of 64% over the ideal vacancy.

5.3.2 Vibrational properties

Table 5.1 compares the calculated quasi-harmonic vibrational frequencies of vacancy-hydrogen-deuterium complexes with those determined experimentally [56]. The calculated modes consistently overestimate the LVMs by between 4 and 8%. The reason for the overestimate lies partly in the neglect of anharmonic terms. The effect of anharmonicity has been tested for VH complexes in silicon by finding the energy necessary to displace the atoms in each normal coordinate and then solving the Schrödinger equation for the oscillator using the shooting method [68]. The resultant symmetric frequency of VH_2 was found to increase by only 2 cm^{-1}. The asymmetric stretch frequency however was found to increase by 47 cm^{-1} reducing the splitting of the modes to 4 cm^{-1}. The difference is proposed to arise from the neglect of coupling effects between stretch and wag modes in the theoretical treatment.

Also calculated were the vibrational modes for both VH_3^- and neutral V_2H_6. The effect of the addition of an electron to VH_3^0 was to shorten all the Ge-H bonds by 0.7% resulting in modest increases in the frequencies of the E and A symmetry vibrational modes by 6 and 25 cm^{-1} respectively. V_2H_6 was found to have the shortest Ge–H bondlength of all the vacancy-hydrogen defect at 1.520 Å. Two stretch modes of A_{2u} and A_{1g} symmetry were found at 2131 and 2129 cm^{-1}. Two doublet E_u and E_g modes lie at 2128 and 2120 cm^{-1}. The A_{1g} and E_u modes are IR inactive. The frequencies of the active modes (2131 and 2128 cm^{-1}) correspond reasonably to those identifies with V_2H_6 (2025 and 2015 cm^{-1}). The splitting between the IR active modes is then only 3 cm^{-1}. This is substantially smaller than the splitting of the VH_3 symmetric and non-symmetric modes (31 cm^{-1})

5.3.3 Electronic character

5.3.3.1 The germanium vacancy

The ideal (T_d symmetry) vacancy possess one gap state with symmetry t_2 and is occupied by two electrons in the neutral charge state (see Fig 5.3). The electronic structure of the vacancy in silicon is now well understood through the use of a linear combination of atomic orbitals (LCAO) model. The three dangling bond orbitals labelled *a*-*d* give

	VH	VD			
	2107 (?)	1435 (?)			
	VH$_2$	VHD	VD$_2$		
s	2102(1993)	2090(?)	1495(1444)		
		1486(1437)			
a	2078(1980)		1478(1433)		
	VH$_3$	VH$_2$D	VHD$_2$	VD$_3$	
s	2098(?)	2088(?)	2077(?)	1491(?)	
		1477(?)	1484(?)		
a	2067(?)	2067(?)	1471(?)	1471(?)	
	VH$_4$	VH$_3$D	VH$_2$D$_2$	VHD$_3$	VD$_4$
s	2187 (-IR)	2168(2084)	2149(2080)	2128(2075)	
a	2107(2062)	2107(2062 or 2066)	2107(2066)		
			1499(1489)		
s		1511(1491)	1524(1499)	1539	1554 (-IR)

Table 5.1: Calculated (quasi-harmonic) stretch frequencies and observed (in brackets) (cm^{-1})^a of VH$_n$ defects in germanium. Assignments of experimental absorption lines to VH$_2$D, VHD$_2$ are tentative. s, total symmetric; a, total non-symmetric, -IR, infra red inactive.

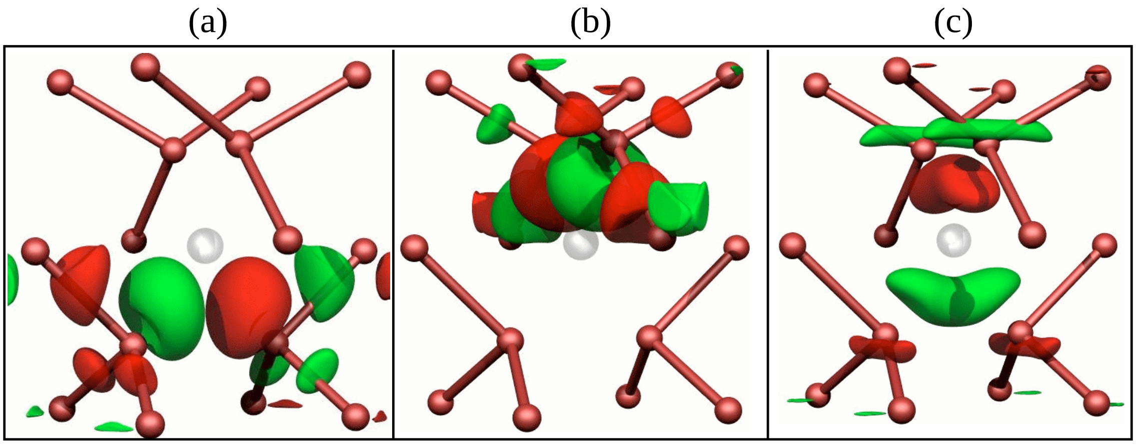

Figure 5.2: Isosurface plots of the gap states of the D_{2d} vacancy in germanium. Positive and negative lobes are coloured red and green. The vacant site is indicated by the ghost atom.Plots (a) and (b) show the two orbitals comprising the *e*-doublet. Plot (c) is the isosurface of the b_2 orbital.

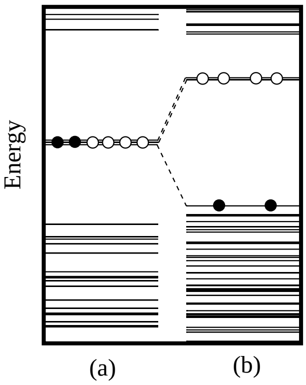

Figure 5.3: Splitting of the vacancy t_2 level under the Jahn-teller distortion from T_d to D_{2d} symmetry. The filled and open circles represent the electronic and hole filling respectively of the gap states.

rise two a number of states through their linear combinations. There are three linearly independent combinations which are degenerate:

$$\left.\begin{array}{ccccccc} a & + & b & - & c & - & d \\ a & - & b & + & c & - & d \\ a & - & b & - & c & + & d \end{array}\right\} \psi_{t_2}$$

These constitute a t_2 triplet state. The remaining linearly independent combination is a total symmetric a_1 singlet state:

$$a + b + c + d \qquad \psi_{a_1}$$

These states are plotted in Fig. 5.2.

The KS levels of the ideal germanium vacancy show that the a_1 state lies buried in the valence band, and the t_2 state is that which appears in the bandgap. In the neutral charge state the triplet is partially filled and undergoes a Jahn-Teller distortion to a lower symmetry. The reconstruction of dangling bonds reduces the symmetry to D_{2d}. Labelling the paired atoms a,b and c,d the t_2 orbital splits because the combination $(a+b)-(c+d)$ becomes inequivalent to the other two combinations, $(a+c)-(b+d)$ and $(a+d)-(b+c)$, splitting the t_2 levels into a b_2 and an e state. This is shown in Fig 5.3 where the b_2 state lies just above the valence band edge and the doublet state lies above mid-gap.

5.3.3.2 VH complexes

As in silicon the Kohn-Sham levels demonstrate the passivating effects of hydrogen on the deep dangling-bond levels. The e doublet is split into two singlet states by the addition of a single H to the vacancy. The lower singlet is filled for VH_2^0 leaving a singlet state in the band gap. This state become partially occupied for VH_3. The unpaired wavefunction of VH_3^0 is plotted in Fig 5.5. Passivation of the vacancy is complete upon the addition of four H atoms. The KS spectra for VH defects are shown in Fig. 5.4.

The acceptor and donor levels have been calculated using the method described in Chapter 4. The marker approach is probably less applicable in germanium because of the smaller bandgap and lack of a marker defect that is very well characterised. The chosen marker defect is substitutional gold. This defect can exist in five charge states in germanium and has three acceptor levels and a donor level. The single donor and acceptor levels of Au_s lie at E_v+0.04 and E_v+0.15 eV respectively [69].

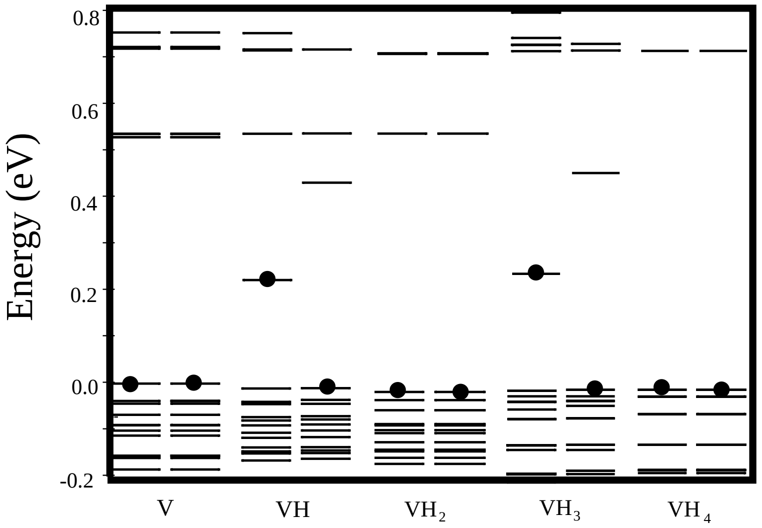

Figure 5.4: Kohn-Sham eigenvalues of the isolated neutral vacancy and VH complexes in germanium. The bandgap has been scaled to the experimental value. The highest occupied levels are indicated by the filled circles. Doublet levels in the gap are shown by thick lines.

The ionisation energies of VH, VH_2 and VH_3 were calculated to be within 0.02 eV of the Au_s ionisation energy. Given the expected error, this places the donor levels for each of the defects close to the valence band edge, possibly in the valence band. The electron affinities were also found to be similar for VH, VH_2 and VH_3, 0.1 eV higher in energy than that calculated for Au. This places the single acceptor levels in the lower half of the bandgap, close to the valence band edge.

5.4 Conclusions

The isolated vacancy was found to undergo a strong Jahn-Teller distortion to form reconstructed bonds 16% longer than the bulk Ge-Ge bondlength. There gap states are of e and b_2 symmetry which can be understood well from a simple LCAO model. The addition of H to the vacancy acts to remove the gap states resulting a fully passive VH_4 defect.

The vibrational mode frequencies calculated are within 8% of those observed. This error is similar to that found for calculations of VH_n modes in Si. The calculated frequencies of the local modes of VH_2, VH_4 and V_2H_6 support the assignments of the observed IR modes [56].

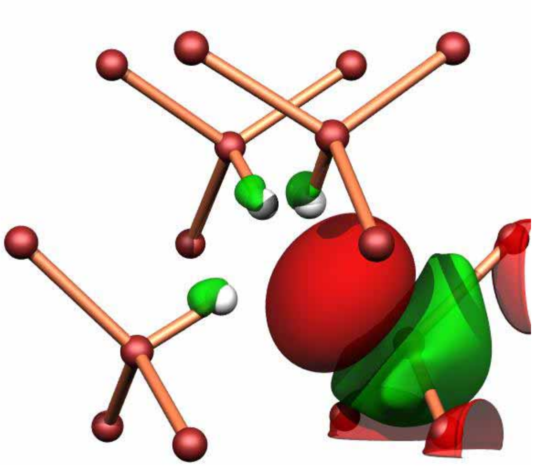

Figure 5.5: Isosurface plot of the highest occupied orbital of VH_3.

Chapter 6

The single interstitial in silicon

6.1 Introduction

Self-interstitials are present in all semiconductors to some degree. Vacancies and interstitials may be grown in, or created through some lattice damaging process so that their concentration may exceed 10^{19} cm^{-3}. The vacancy is one of the most well characterised defects in silicon observed through EPR in its positive and negative charges and modelled successfully using *ab initio* cluster theory [22]. The self-interstitial, however, remains elusive and has only definitely been observed indirectly through its interaction with impurities [29].

The present knowledge of the isolated self-interstitial is largely based on theory, which has predicted the ground state structures of each charge state and suggested possible migration mechanisms of the defect. Some of the configurations of the self-interstitial which have been considered are shown in Fig. 6.1. They are the: (a) $\langle 001 \rangle$ split-interstitial (D_{2d} symmetry) (b) $\langle 110 \rangle$ split-interstitial (C_{2v} symmetry) (c) tetrahedral interstitial (T_d symmetry) and (d) the hexagonal interstitial (D_{3d} symmetry). Also considered previously by theoreticians is the bond-centred interstitial. Each of these defects could conceivably distort to a lower symmetry as has been discussed previously [2, 70].

The majority of the theoretical investigations have concluded that the ground state of the neutral interstitial, I_1^0 is the $\langle 110 \rangle$ split-interstitial [71, 72, 73, 3]. Previous work using AIMPRO agrees with this result [2] and shows that the $\langle 001 \rangle$ split-interstitial is unstable. The energies obtained by AIMPRO [2] are compared with the results of Mainwood *et al* [3] in Table 6.1. There are quite large differences in the energies calculated but, in agreement with others, both methods predict the $\langle 110 \rangle$ split-interstitial to be lowest in energy for the neutral and negative charge states.

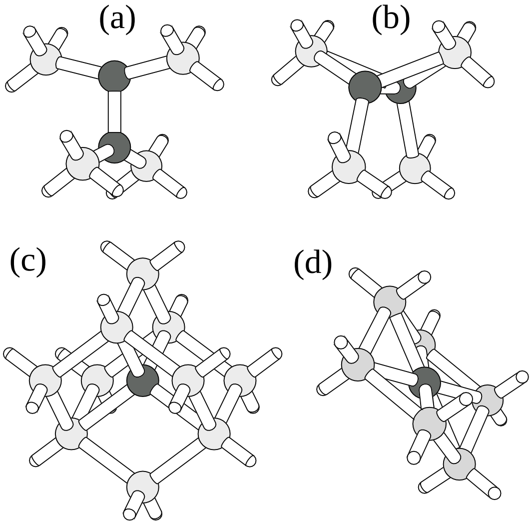

Figure 6.1: Possible configurations of the isolated self-interstitial in silicon. In each case the atoms lying close to their lattice sites are shaded light grey. (a) ⟨001⟩ split-interstitial. (b) ⟨110⟩ split-interstitial. (c) Tetrahedral interstitial. (d) Hexagonal interstitial.

Configuration	2+	+	0	-
⟨110⟩	1.99 (1.5)	0.72 (0.0)	0.00 (0.0)	0.00 (0.0)
BC	0.92 (3.5)	0.99 (2.1)	1.19 (2.0)	1.42 (1.3)
Hex	1.02 (0.0)	0.29 (0.2)	0.02 (2.6)	0.52 (0.5)
T_d	0.00 (0.4)	0.00 (0.5)	0.45 (2.3)	0.79 (1.8)

Table 6.1: Energies (eV) relative to the ground state of various charge states of the self-interstitial in silicon as calculated by AIMPRO [2]. The results of Mainwood *et al* [3] are shown in brackets for comparison.

6.2 Background

Recently, Mukashev *et al* claimed to have observed the isolated self-interstitial directly by DLTS and EPR [74]. The two spectra are labelled E1 and AA12 respectively.

The E1 DLTS level lies at $E_c - 0.39$ eV and is observed in *p*-type Si by minority carrier spectroscopy following irradiation [74]. E1 occurs in both Czochralski and float-zone Si and appears not to depend on the acceptor impurity type suggesting that the defect is intrinsic. The E1 spectrum can be eliminated by minority carrier injection at 77 K. Mukashev *et al* demonstrate that under minority carrier injection conditions, the annealing rate of E1 correlates strongly with the appearance of the C_i DLTS level, H3. These observations suggest that the defect is a primary intrinsic radiation product.

The isotropic EPR spectrum AA12 [74] is observed in high-purity irradiated Si. The hyperfine structure due to a ^{29}Si at a unique site was resolved. This hyperfine satellite is isotropic, and corresponds to a few percent of the unpaired wavefunction localised at the unique site. Unresolved hfs due to a ^{29}Si at 4–6 equivalent sites was also observed. The AA12 spectrum is observed only following a burst of bandgap light. This implies that the defect forms in a diamagnetic state and is observed by EPR when an electron or hole is trapped following illumination. Mukashev *et al* reports that the recharging kinetics places the level position $\sim$ 40 K from either E_v or E_c [74]. AA12 anneals out in the region 280–350 K.

Mukashev *et al* conclude that E1 is the double donor level of the single interstitial and AA12 corresponds to the single positive charge state of the interstitial. He argues that the single interstitial exists in the 2+ charge state, lying at the T_d site. This location for the 2+ charge state is supported by *ab initio* calculations [2, 75]. Illumination causes the defect to trap an electron so that the defect has +1 charge and is observed by EPR.

In this chapter, we briefly examine the properties of just two isolated interstitial defects, namely the $\langle 110 \rangle$ split-interstitial and the tetrahedral interstitial. The former defect is chosen as it is well established by theory to be the most stable form of I^0. Furthermore, the five-fold coordination is examined in detail because the over-coordinated bonding appears to be a feature of small interstitial aggregates in Si (see Chapter 8). This characteristic is of special interest as it may allow the possibility of low energy reorientation and diffusion. We consider the reorientation of the $\langle 110 \rangle$ split-interstitial as a prototype in the understanding of the diffusion of overcoordinated Si interstitials. The isolated tetrahedral interstitial is studied in the light of the assignment of the isolated self-interstitial at the T_d site to EPR and DLTS signals [76] seen in irradiated Si.

6.3 Method

The single interstitial defects are analysed using the cluster and supercell approaches. The defect is positioned at the centre of a cluster of crystalline silicon with configuration $Si_{182}H_{116}$ or $Si_{185}H_{120}$. These clusters are centred at the substitutional and tetrahedral sites respectively. The relevant cluster for each defect is chosen to be that in which the defect lies at the center of the cluster, thereby maintaining the correct symmetry point group. The wavefunction fitting basis consists of independent s and p Gaussian orbitals with four different exponents, placed at each Si site. A fixed linear combination of two Gaussian orbitals are sited on the terminating H atoms. In addition, s and p orbitals are placed at each Si–Si bond centre to ensure good description of the Kohn-Sham states. The charge density is fitted with four independent Gaussian functions with different widths on each Si atom and three on the terminating H atoms. One extra Gaussian function is placed at each Si–Si bond centre. The positions of all bulk atoms are optimised. Electrical levels are calculated using the method described in Chapter 4. The ⟨110⟩ interstitial was also optimised in a 64+1 atom supercell with cut-off energy of 80 Rydbergs.

6.4 Results

The isolated neutral ⟨110⟩ interstitial was optimised with C_{2v} symmetry in both a cluster and supercell. The bondlengths of the relaxed defect are given in Table. 6.2 and the labelling scheme is shown in Fig. 6.4 (Left). In both cluster and supercell calculations, we find that the bonds labelled x, which connect the five-fold coordinated atoms to the central split-interstitial, are extended relative to the ideal Si–Si bondlength (2.35 Å). The other bonds are compressed.

Bond	Cluster	Supercell
x	2.454	2.429
y	2.264	2.241
z	2.246	2.243

Table 6.2: Bondlengths (Å) of the neutral ⟨110⟩ interstitial. Bond labels are those given in Fig. 6.4.

The isolated neutral ⟨110⟩ interstitial gives rise to three singlet KS states deep within the bandgap as shown in Fig. 6.3. Two gap states, close in energy, are fully occupied in the neutral charge state. Wavefunction plots of the three deep states are shown in Fig. 6.3. The orbitals labelled (a), (b) and (c) in Fig. 6.3 have symmetries a_2, a_1 and b_1 respectively. All three orbitals are largely localised of the atoms which make up the split-interstitial pair itself whilst some component exists on the five-fold coordinated atoms.

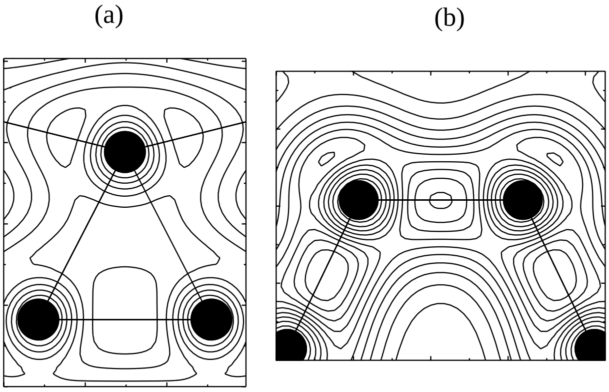

Figure 6.2: Charge density contour plot of the ⟨110⟩ split-interstitial in silicon. Filled circles denote atoms lying in the plane. (a) The plane containing the split-interstitial pair and one of the five fold coordinated atoms. (b) The defect mirror plane containing the split-interstitial atoms.

The charge density around the atoms in the defect is shown in Fig. 6.2. This demonstrates that the bonds which connect the five-fold coordinated atoms to the central split-interstitial consist are weak, with low, quite widely spread charge density across them. This contrasts to the strong bonds made between the atoms which lie in a defect mirror plane (Fig. 6.2 (b)).

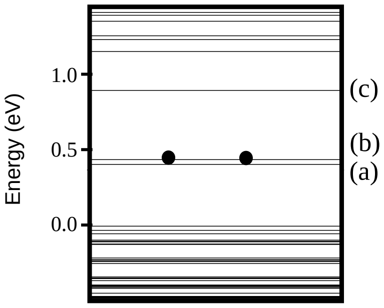

Figure 6.3: KS eigenvalues ⟨110⟩ interstitial in silicon. The bandgap has been rescaled to the experimental value. The electronic occupation of the highest occupied level is indicated by filled circles. Isosurfaces of the labelled states are plotted in Fig. 6.5.

The electronic structure of the ⟨110⟩ split-interstitial can be explained by consideration of a simple atomic orbital picture. This technique has been applied to understand the electronic levels of the isolated vacancy and divacancy [77, 8]. We also considered this picture in Chapter 5 for the Ge-vacancy. For these vacancy defects, the use of a linear combination of atomic orbitals (LCAO) scheme is evidently suitable as structures of these defects produces simple three fold-coordinated atoms whose bonds are roughly at tetrahedral angles. Each threefold atom then has a sp^3-like dangling bond orbital which is well approximated by an atomic orbital picture. For the $\langle 110 \rangle$ split-interstitial the picture is not so simple. It is not immediately obvious how to choose an appropriate set of atomic orbitals.

One way to begin is shown in Fig. 6.4. Here, the $\langle 110 \rangle$ defect is shown alongside a schematic of a Si dimer molecule. The dangling bonds of the dimer have been arranged to match those of the interstitial and extra atoms are placed around the dimer corresponding to the second shell of the $\langle 110 \rangle$ defect. The picture is simplified in this way because we can associate the Si–Si dimer bond with the $\langle 110 \rangle$ central bond of the self-interstitial defect. Having done that, it is reasonable to identify two of the remaining dangling bonds with the covalent bonds y. This is credible as in the relaxed structure of the $\langle 110 \rangle$ split-interstitial, bonds y and z have bondlengths close to ideal and the angle between them is 116°, quite close to the tetrahedral angle (109.5°). If this picture is correct then four dangling bond orbitals labelled a-d in Fig. 6.4 remain unsatisfied.

The dangling bond orbitals of the dimer, a, b, c, d, along with those of the second shell atoms, e, f can now be used to understand the electronic structure of the self-interstitial, explaining the existence of three gap states:

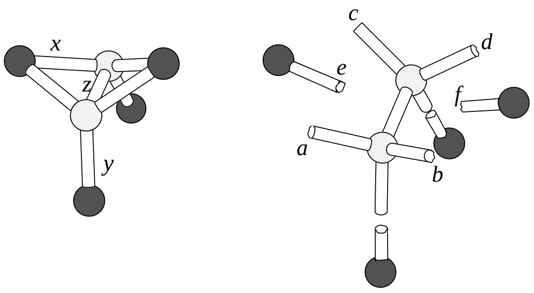

Figure 6.4: Schematic showing the bonding of the $\langle 110 \rangle$ split-interstitial. Left: The $\langle 110 \rangle$ split-interstitial. The defect can be reduced to three non-equivalent bonds labelled x, y, z. Right: A Si dimer surrounded by four atoms placed at positions corresponding to the split-interstitial defect. The six dangling bonds are orientated to match the split-interstitial as closely as possible.

We can construct four linearly independent combinations of the atomic orbitals a, b,

c and d: There are three linearly independent non-symmetric combinations,

$$\left.\begin{array}{llllllll} \text{(i)} & a & + & b & - & c & - & d \\ \text{(ii)} & a & - & b & + & c & - & d \\ \text{(iii)} & a & - & b & - & c & + & d \end{array}\right\}$$

and the total symmetric state,

$$\begin{array}{llllllll} \text{(iv)} & a & + & b & + & c & + & d \end{array}$$

Taking each of these linear combinations (i)–(iv) in turn, the gap states of the $\langle 110 \rangle$ split-interstitial can be understood.

First, consider the combinations $(a + b)$ and $(a - b)$. Atomic orbital a is of the form $(s, p_x, p_y, p_z) = (1, 1, 1, 1)$ and orbital b is of the form $(s, p_x, p_y, p_z) = (1, 1, -1, -1)$. Adding the two states gives $(s, p_x, p_y, p_z) = (2, 2, 0, 0)$, an *sp* lobe which points along the average direction of a and b. Subtracting the two states gives $(s, p_x, p_y, p_z) = (0, 0, 2, 2)$, a p-like lobe, orthogonal to $(a + b)$.

Combination (i) then, written $(a + b) - (c + d)$ comprises of a pair of *sp* orbitals, $(a + b)$ and $(c + d)$ lying antiparallel with respect to each-other on each atom. This linear combination can be identified with the lowest gap-state shown in Fig. 6.5(a). The linear combination (iv), $(a + b) + (c + d)$, corresponds to these *sp* orbitals lying parallel. This can be identified with Fig. 6.5(b). The non-symmetric combination, (iii) written $(a - b) - (c - d)$ comprises of two p orbitals lying antiparallel. This linear combination gives rise to the highest gap-state Fig. 6.5(c). The remaining linear combination, (ii) can be written $(a - b) + (c - d)$. This can be visualised as a pair of parallel p orbitals on each atom. These two p orbitals form a π bond which in turn forms a bonding state with the dangling bonds labelled e and f in Fig. 6.4. The state corresponding to this combination lies buried in the valence band.

The reorientation of the $\langle 110 \rangle$ interstitial was performed using the orthogonal relaxation method described in Chapter 4. The relaxed coordinates of a [110] oriented interstitial and a $[10\bar{1}]$ oriented interstitial were used for the initial and final positions of the vector v_i. The resulting diffusion path and barrier is indicated in Fig. 6.6. The mid-point structure to the reorientation process has C_{1h} symmetry and constitutes a local minimum in energy. The barrier is calculated to be less than 0.1 eV. If the attempt frequency for the process is taken to be 10^{13} Hz, this barrier corresponds to a temperature of just 30 K.

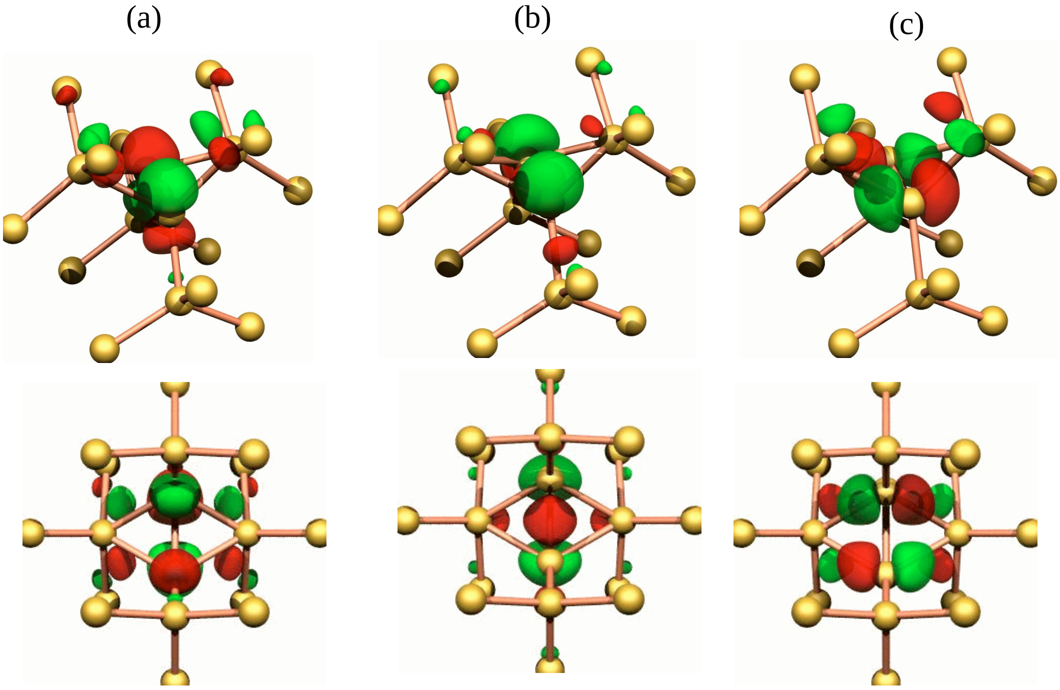

Figure 6.5: KS gap state wavefunctions of the neutral ⟨110⟩ interstitial in silicon. The three isosurfaces (a), (b) and (c) correspond to the KS eigenvalues shown in Fig. 6.3.

We now consider the tetrahedral self-interstitial in relation to the assignment of this defect to the AA12 and E1 centres. The defect was optimised in the neutral charge state with symmetry confined to T_d. The presence of the extra atom has only a small effect on the positions of the surrounding atoms, shifting them by less than 0.1 Å away from the defect centre.

The self-interstitial at the tetrahedral interstitial site gives rise to four states within the bandgap as shown in Fig. 6.7 (Left). Three empty levels lie in the upper half of the bandgap with symmetries t_2 and e. The two doublet e-levels are approximately degenerate, and lie $\sim$ 0.1 eV above the triplet state. The filled level is of a_1 symmetry and lies within $\sim$ 0.1 eV of the valence band edge.

In the neutral charge state the highest occupied level is of t_2 symmetry. In both the neutral and positive charge states then, there will be a Jahn-Teller distortion to a lower symmetry. If the distortion from T_d symmetry is small, allowing thermally activated reorientation between close-by minima, then the observed symmetry would be T_d. In this case, the *effective* unpaired electronic wavefunction would be the average of a number of equivalent states. For the small distortion we expect this effective averaged wavefunction to possess the character of the t_2 state.

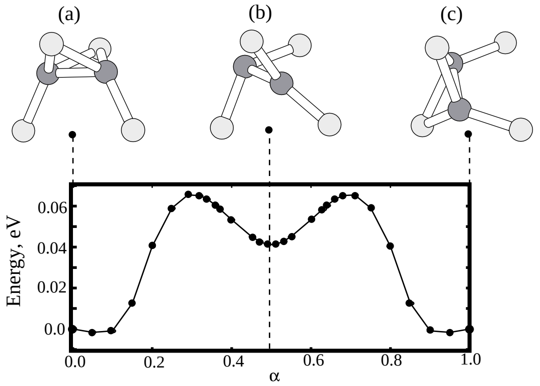

Figure 6.6: Reorientation path of the ⟨110⟩ interstitial. The two atoms sharing the site are shown in dark grey. (a) The optimised [110] oriented interstitial. (b) Mid-point structure to reorientation (C_{1h} symmetry) (c)The [$10\bar{1}$] oriented interstitial.

The t_2 wavefunction isosurface is plotted in Fig. 6.7 (Right). Clearly the wavefunction is largely localised upon the central atom. Mulliken analysis shows that 24% of the wavefunction is localised upon the central atom. This component of the wavefunction is purely *p* like and given the T_d symmetry of the defect, this will not result in an overall hyperfine interaction with the central nucleus. However, it is possible that the $\sim$ 16% of the wavefunction accounted for at the neighbouring sites will overlap the unique atom resulting in the hyperfine satellite observed.

Mukashev *et al* place the $(+/++)$ level at $E_c - 0.39$ eV. Calculation of the double donor level of the T_d interstitial was performed in two clusters. The marker defect was chosen to be substitutional sulphur dimer, 2S_s. This defect possesses a double donor level close to the E1 level at $E_c - 0.37$ eV. The assignment of this level is said to be in no doubt [78]. The calculation of the double ionisation energies of the T_d interstitial and the 2S_s centre places the second donor level of I_1 at $E_c - 0.20$ eV, within 0.2 eV of the level found by Mukashev *et al.*

6.5 Conclusions

Consideration of the isolated ⟨110⟩ split-interstitial has given an insight into the bonding arrangement of "overcoordinated" structures. The gap-states of the ⟨110⟩ split-interstitial appear complex but, remarkably, can be understood by consideration of a simple LCAO picture. The defect can be compared to a Si–Si dimer introduced into a vacancy in the crystal lattice. Two of the six dangling bonds of the dimer form normal covalent bonds

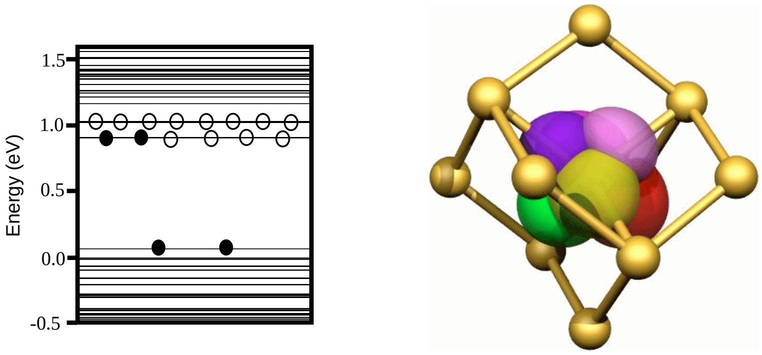

Figure 6.7: Electronic character of the tetrahedral self-interstitial Left: KS eigenvalue plot of I^0 at the tetrahedral interstitial site. The electronic filling of the gap states is indicated by the filled (electrons) and unfilled (holes) circles. Right: An isosurface plot of the highest occupied wavefunction (t_2 symmetry) is shown to the right. Each lobe represents a positive or negative sign of one of the component wavefunctions.

leaving four dangling bond orbitals. Treating these as atomic orbitals and finding their linearly independent combinations we generate four states. Three of these states can be identified with those calculated for the $\langle 110 \rangle$ split-interstitial to lie within the band gap. The remaining combination leads to a bonding state which lies in the valence band. This latter state corresponds to a bonding combination of the π bond (which arises from parallel p orbitals on the two central atoms) with the 'dangling bonds' of the two adjacent 'lattice' atoms. The calculation of the charge density distribution shows that this 'five-fold' bond is relatively weak with a substantially lower charge density than a bulk Si–Si bond.

The reorientation of the $\langle 110 \rangle$ split-interstitial has been considered. The reorientation path involves only the making and breaking of the weak five-fold bonds. This provides an explanation as to the low calculated reorientation barrier of the interstitial. This mechanism may also be applicable to the small multi-interstitials resulting in low reorientation and diffusion barriers. One important consequence of the low reorientation barrier is that, if the defect were observed by, for example EPR, it is likely that the effective symmetry of the centre would be T_d at temperatures higher than ~ 100 K.

The properties of the tetrahedral interstitial were calculated in order to assess the assignment of the AA12 EPR centre and E1 DLTS signal to the defect. The calculated unpaired wavefunction of the positively charged defect can be interpreted as reasonably consistent with the hyperfine analysis. The experiment shows that there is a small isotropic interaction with a ^{29}Si at a unique site. The presence of hyperfine satellite could be explained by the unpaired wavefunction in the surrounding cage interacting with the central nucleus.

One potential problem with the assignment of AA12 to the single positively charged self-interstitial is the report of a unique site. Whilst this is immediately expected from the model, in the positive charge state, the tetrahedral interstitial must move off-site through the Jahn-Teller effect. If the assignment is correct, then the observed centre corresponds to an *effective* T_d symmetry which results from a dynamic jumping of the atom between equivalent sites close to the tetrahedral site.

The calculation of the double donor level gives a value of around $E_c - 0.20$ eV. This value is within the error of the method of the proposed level ($E_c - 0.39$ eV). Thus these calculations generally support the assignments of Mukashev *et al* [76]. Evidently, however, further experimental and theoretical work is necessary to assess the nature of the Jahn-Teller distortion from T_d symmetry in the positive charge state.

Chapter 7

The di-interstitial in silicon

7.1 Introduction

While reliable experimental assignments in Si have been made for the first six multi-vacancy defects, V_n, for $n \leqslant 6$ [11, 79, 12], less progress has been made in identifying multi-interstitials, I_n. This is in spite of the importance of these centres in both nucleating extended defects such as the {311} rod-like defect [5] and Frank partials [80] and in their relation to the transient enhanced diffusion (TED) of boron [81]. In this, and the subsequent two chapters, the results of investigations into I_n, ($n = 2$ to 4) defects in silicon are reported.

Several experimental observed spectra have been classed as small interstitial aggregates [74, 82, 83, 84, 85] although, to date, none of the spectra are conclusively identified with specific defect structures. A summary of the EPR spectra that have been attributed to self-interstitial clusters is given in Table 7.1. The natures of the P6 and B3 spectra are discussed in detail in this, and the following chapters. These two centres have been extremely well characterised with information available on hyperfine structure and energetics as well as the symmetry and annealing ranges. The other two centres, A5 and NL51 are both spin 1 defects. Whilst the spin-spin interaction (D) tensors for these defects have been determined, there is little further information that can be used to firmly identify them with defect structures. These centers will not be discussed further.

The lack of conclusive experimental information on small aggregates of the self-interstitial has spurred a great interest in theoretical modelling studies so that several candidate structures of I_n for n from 1 to 4 have been published [86, 10, 9, 87]. With the exception of I_2 [87] and I_4 [88], however, there is no strong experimental evidence supporting any of these structures. In the case of I_2, the situation is complex and close analysis of the available data uncovers serious inconsistencies between experiment and theory. In this chapter we address these issues, and provide theoretical data on other candidate structures for I_2.

Label	Ref.	Symmetry	Spin	Annealing range	g-values
P6	[82]	C_2 (D_2)	1/2	–170°C	$g_1 = 2.0010$, $g_2 = 2.0040$, $g_3 = 2.0062$
A5	[83]	D_{2d}	1	–190°C	$g_\perp = 2.0064$, $g_{\|\|} = 2.0066$
B3	[84]	D_{2d}	1/2	170 – 450°C	$g_\perp = 2.0159$, $g_{\|\|} = 2.0051$
NL51	[85]	D_{2d}	1	$\sim 200 - 500$°C	$g_\perp = 2.0071$, $g_{\|\|} = 2.0007$

Table 7.1: Summary of EPR centres which have been attributed to self-interstitial clusters.

7.2 Background

In 1976, one EPR spectrum was been assigned to a self-interstitial defect. The P6 EPR centre is observed directly following proton or Si ion implantation of silicon and survives annealing up to 170°C. P6 is characterised by an unusual temperature dependent g-tensor. At low temperature ($\sim$ 200 K) the centre possesses "monoclinic II" symmetry with the symmetry axis parallel to $\langle 001 \rangle$ (see Table 7.2 and Fig. 7.1). As the temperature is raised, the spectrum broadens until, at $\sim$ 300 K, it represents an effective "rhombic type II" symmetry. These symmetry groups are two of the eight symmetry groups distinguishable by EPR and, in general, do not uniquely define the point group symmetry of a defect. In materials with the diamond structure however, these two particular symmetry groups do uniquely identify the point group symmetry to be C_2 and D_2 respectively (see Table 3.1). It is crucial therefore that any model for the P6 centre must take account of these symmetries.

Analysis of the hyperfine interaction has provided valuable information about the defect structure. The authors report two hyperfine satellites (hfs), labelled A and B, on the high field side of the main resonance signal at low temperature. The hyperfine structure is analysed in the standard way: If the unpaired electron wavefunction consists of a $3s$, $3p$ hybridised orbital, we can write

$$\Psi_{uwf} = \sum_i \eta_i \left(\alpha_i \chi_i^{3s} + \beta_i \chi_i^{3p} \right) \tag{7.1}$$

g	A(A) (cm^{-1})	A(B) (cm^{-1})
$g_1 = 2.0010$	$\mathrm{A}_1 = 34 \times 10^{-4}$	$A = 24.3 \times 10^{-4}$
$g_2 = 2.0040$	$\mathrm{A}_2 = 43 \times 10^{-4}$	
$g_3 = 2.0062$	$\mathrm{A}_3 = 58 \times 10^{-4}$	
$\theta = 17°$	$\theta_A = 5°$	

Table 7.2: Tabulation of g-values determined from the P6 spectrum in silicon taken from Ref. [4]. The angle, θ and principal axis direction are shown in Fig. 7.1.

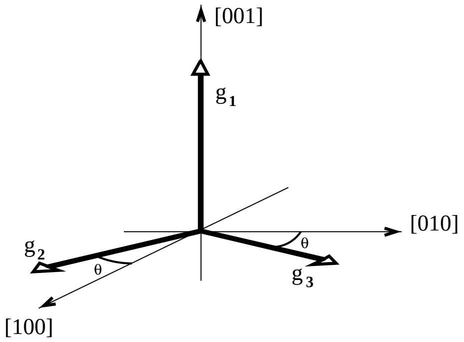

Figure 7.1: Principal directions of the g-tensor of the P6 EPR centre. The values of the tensor elements and angles are given in Table 7.2.

with $\alpha_i^2 + \beta_i^2 = 1$ and $\sum_i \eta_i^2 = 1$. η_i refers to the fraction of the total unpaired wavefunction at nuclear site i, and α_i^2 and β_i^2 are the fractions of the s and p components of the wavefunction respectively at site i. The hfs parameters for a system with axial symmetry are taken from Ref. [89]:

$$A_{||}^i = a_i + (2 - \frac{3}{2}\Delta g_\perp) b_i \tag{7.2}$$

$$A_\perp^i = a_i - (1 - \frac{13}{4}\Delta g_\perp) b_i \tag{7.3}$$

where

$$a_i = \frac{8}{3}\pi g_0 g_N \mu_B \mu_N \alpha_i^2 \eta_i^2 |\chi_{3s}(0)|_i^2$$

$$b_i = \frac{2}{5}\pi g_0 g_N \mu_B \mu_N \beta_i^2 \eta_i^2 \langle r_{3p}^{-3} \rangle_i$$

with $g_N = -1.1106$, $|\chi_{3s}(0)|^2 = 31.5 \times 10^{24}$ cm^{-3} and $\langle r_{3p}^{-3} \rangle = 16.1 \times 10^{24}$ cm^{-3} for ^{29}Si. The three parameters, α_i^2, β_i and η_i are then determined using Eqns. 7.1 – 7.3.

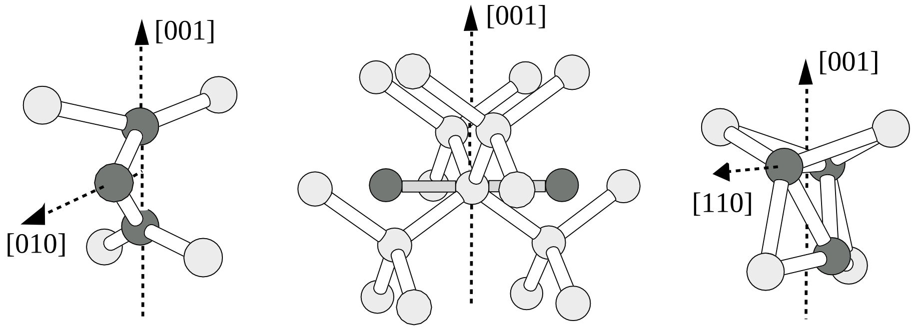

Figure 7.2: Schematics showing the structures of I_2 defects previously proposed. In each case the atoms lying close to their lattice sites are shaded light grey. Left: The original defect structure proposed for P6 [6]. Middle: Modified structure [4]. Right: Defect structure proposed for P6 by Kim *et al* [7].

Using this approach the unpaired wavefunction is found to have 86% p character with 23% of the wavefunction localised at a single, unique site labelled A. A total of 3.4% of the unpaired wavefunction is localised on the two equivalent sites labelled B. These value were reported in the original article reporting the discovery of the P6 centre. In a later paper by the same first named author [90], the localisation of the resonant wavefunction on sites A and B were reported to be 30% and 14% respectively. The reason behind the difference in these values is unclear. It is also reported in the second paper that the high temperature symmetry is D_{2d} although the original paper clearly reports D_2 symmetry.

The energetics of the P6 defect were studied in detail. The thermally activated rapid reorientation from one C_2 configuration to another equivalent C_2 results in the effective $D_{2(d)}$ symmetry observed at higher temperature. By measuring the linewidth of the central EPR peak as a function of temperature, the barrier to this reorientation process was measured to be $\Delta = 0.15$ eV with a frequency factor, $\tau^{-1} \sim 10^9\text{sec}^{-1}$. Above ~ 200 K the defect has D_2 symmetry with the principal axis lying along a $\langle 001 \rangle$ direction. The application of stress at high temperature reveals the energy necessary to reorient the principal axis of the P6 defect to be $0.6(\pm 0.2)$ eV.

The rather detailed information arising from the hyperfine tensor, combined with the defect symmetry at low and high temperatures prompted the original authors to present a structural model for P6. The defect was proposed to be the positive charge state of two interstitials adjacent to a substitutional atom along $\langle 001 \rangle$ axis. This structure is shown in Fig. 7.2 (Left). The high-temperature symmetry results from the rotation of the central atom around the [001] axis shown in Fig. 7.2. Later, the first named author of the original paper, proposed a modification of the structure [90] which explains better the behaviour of the hyperfine satellites during the $C_2 \rightarrow D_2$ transition and the stress results. The new structure is similar to that proposed previously with the modification that the central atom is fixed closer to the substitutional site and the two Si atoms are pushed further away along $\langle 001 \rangle$. This gives a structure with D_{2d} symmetry. The C_2 symmetry is obtained by rotating the three atom dumbbell about [001] by a few degrees.

Recently, theory has been applied to I_2 resulting in the assignment of a different structure than proposed previously for P6 [87]. Shown in Fig. 7.2 (Right), the defect presented by Kim *et al* is constructed by replacing a substitutional atom with three atoms. Two atoms are positioned as a [110] split-interstitial and the third is placed along [001]. Optimisation of this structure allows the third to move along $[1\bar{1}0]$ resulting in a defect with C_{1h} symmetry. Interestingly, this defect structure has arisen independently from molecular dynamics simulations of interstitial aggregation. The 'Kim' defect is demonstrated to possess an unpaired wavefunction which accounts well for the hyperfine measurements. Specifically, the unpaired electron is calculated to be localised mainly on a unique atom and also upon two equivalent atoms. The main drawback of the assignment is that the ground state of the proposed defect possess C_{1h} symmetry and this is irreconcilable with the C_2 symmetry of the P6 centre. Given that this is irrefutable evidence that the observed structure is different from the proposed Kim model, three possibilities exist:

(a) The di-interstitial structure which corresponds to P6 has not yet been found,
(b) P6 is not a di-interstitial but another self-interstitial aggregate,
(c) P6 is not interstitial related at all.

The first possibility seems unlikely given the wealth of experimental evidence which puts severe restrictions on structures which can be considered. In fact, given the hyperfine measurements, symmetry requirements, and low energy reorientation barrier (which implies a rather compact defect) only models which are perturbations of those proposed by Lee *et al* (Fig. 7.2 (left and centre)) appear to be reasonably consistent. To date, however, no first principles calculation has reported the existence of a (meta-)stable structure of this form. If P6 is not a di-interstitial there is a possibility that a tri-interstitial or other small aggregate may be responsible. In the next chapter we consider this possibility. The suggestion that P6 is not purely interstitial related but involves either vacancies or impurities is not easy to support. Vacancy defects are well known to have a {110} planar symmetry clearly at odds with monoclinic II symmetry of P6. Furthermore, the application of stress to the P6 defect gives a value for the degree of alignment at equilibrium of $n_\perp/n_{||} = 17$, an order of magnitude greater than found in vacancy associated defects [77, 83, 79]. The fact that the defect is present in quite high concentrations (10^{16} cm^{-3}) in zone-refined intrinsic Si and the lack of any observed hyperfine interaction with impurity isotopes of C, O or H strongly supports the assignment of P6 with an intrinsic defect.

7.3 Method

The di-interstitial defects are analysed using the cluster-based (AIMPRO [35]) approach. The defect is positioned at the centre of a cluster of crystalline silicon with configuration $Si_{183}H_{116}$. The wave-function fitting basis consists of independent s and p Gaussian orbitals with four different exponents, placed at each Si site. A fixed linear combination of two Gaussian orbitals are sited on the terminating H atoms. In addition, s and p orbitals are placed at each Si–Si bond centre to ensure good description of the Kohn-Sham states. The charge density is fitted with four independent Gaussian functions with different widths on each Si atom and three on the terminating H atoms. One extra Gaussian function is placed at each Si–Si bond centre. The positions of all bulk atoms are optimised.

7.4 Results

We now consider the results of calculations of three di-interstitial structures. The results of the calculations on each structure I–III (shown in Fig. 7.3) is presented separately.

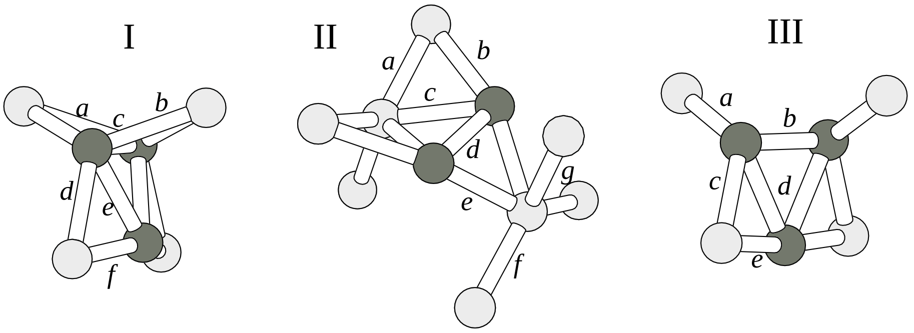

Figure 7.3: Schematics showing the structures of I_2 defects investigated. In each case the atoms lying close to their lattice sites are shaded dark gray.

I(Kim model [7]): The model proposed by Kim *et al* was optimised with symmetry constrained to C_{1h} in the neutral, positive and negative charge states. The relaxed structure of the neutral defect is depicted in Fig. 7.3 and the bondlengths at the defect core are given in Table 7.4. Most bonds in the core are longer than the ordinary bulk Si-Si bonds. This effect is consistent with the weakening of bonds resultant from overcoordination. One important consequence is that the defect does not possess local vibrational modes above the Raman frequency.

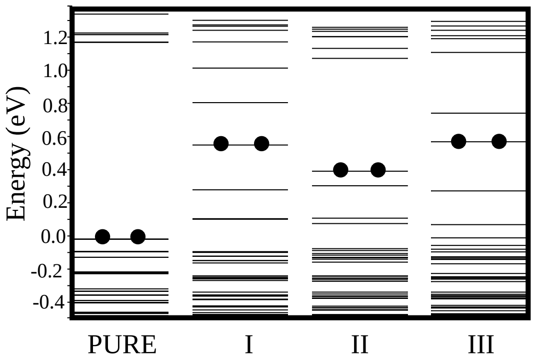

Figure 7.4: KS eigenvalue plot of di-interstitial defects and defect-free cluster (left) for comparison. The labels, I-III of the defects refers to Fig. 7.3.

The KS structure is shown in Fig. 7.4. A number of defect states lie in the band gap. Two are empty and three are fully occupied in the neutral charge state. The defect is calculated to possess both a deep donor and a deep acceptor level (see Table 7.3). The highest occupied wavefunction for the positive charge state has A' symmetry and is plotted in Fig. 7.5 (Left). As found by Kim *et al*, the highest occupied wavefunction is largely localised on the unique atom with some component on surrounding atoms. Mulliken analysis shows that 38% is localised upon the unique atom with the next largest component (3%) being localised upon each of the two other atoms at the defect core. The wavefunction at the unique atom is calculated to be 7% s like in character. These values compare quite well to those found for the P6 centre [6] (24%, 3.4%, 14% respectively).

Since the defect possesses an acceptor level we also show the wavefunction which would be occupied in the negative charge state. This wavefunction has A'' symmetry and is similar in character to the lowest unoccupied wavefunction of the single $\langle 110\rangle$ interstitial plotted in Fig. 6.5 (a). A total of 40 % of the wavefunction is localised upon the two equivalent atoms which is purely p-like in character.

II: The calculations revealed a new structure which also possesses C_{1h} symmetry. This

		Electrical levels (eV)	
Defect	Symmetry	(0/+)	(−/0)
I	C_{1h}	$E_v + 0.49$	$E_c - 0.12$
II	C_{1h}	$E_v + 0.22$	–
III	C_2	$E_v + 0.88$	$E_c - 0.16$

Table 7.3: Calculated electrical levels for I_2 defects, I–III.

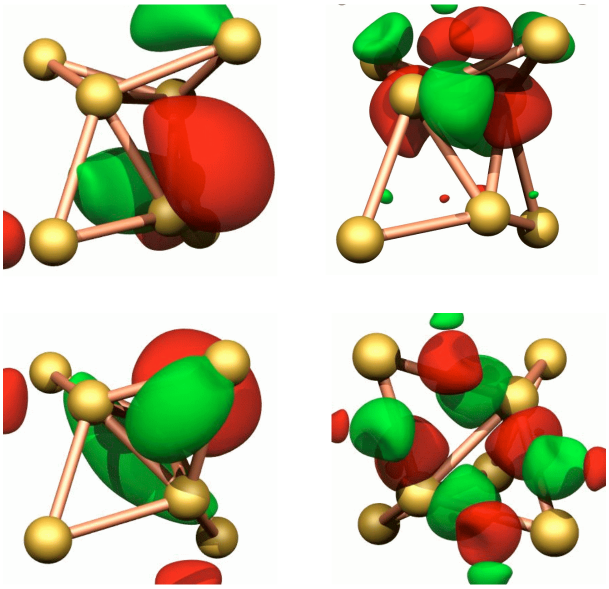

Figure 7.5: Isosurface plots of the highest occupied (Left) and lowest unoccupied (Right) wavefunctions of I_2^+ in the Kim configuration (I). The defect is shown viewed from roughly [010] in the upper figures and from the [001] direction in the lower figures.

defect can be described as a [110] dimer placed at a bond centred site and is shown in Fig. 7.3. In fact, the structure results from only a small movement of atoms from the Kim structure yet it constitutes a distinct defect with its own energy minimum. The Kohn Sham states are shown in Fig. 7.4. The electronic structure is similar to that for the Kim defect (I) but the empty states lie close to the conduction band and the filled states are lower in energy than those of the Kim defect. Calculation of the electrical level predicts a donor level at $E_v + 0.22$ eV but no acceptor level is found. The highest unoccupied level is plotted in Fig. 7.6. Mulliken analysis of this state shows that 18 % of the unpaired wavefunction is localised upon the two equivalent atoms at the defect core. 14 and 7 % is localised upon the two unique atoms which lie in the defect mirror plane.

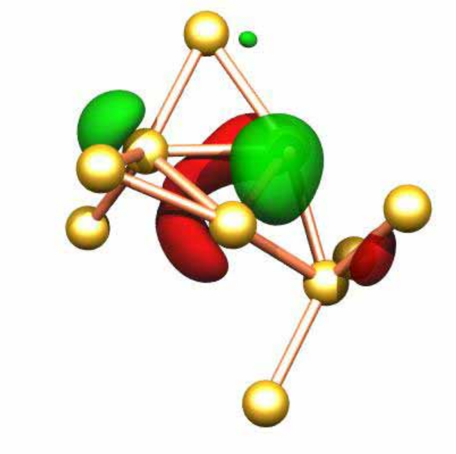

Figure 7.6: Isosurface plot of the highest occupied wavefunction of I_2^0 II.

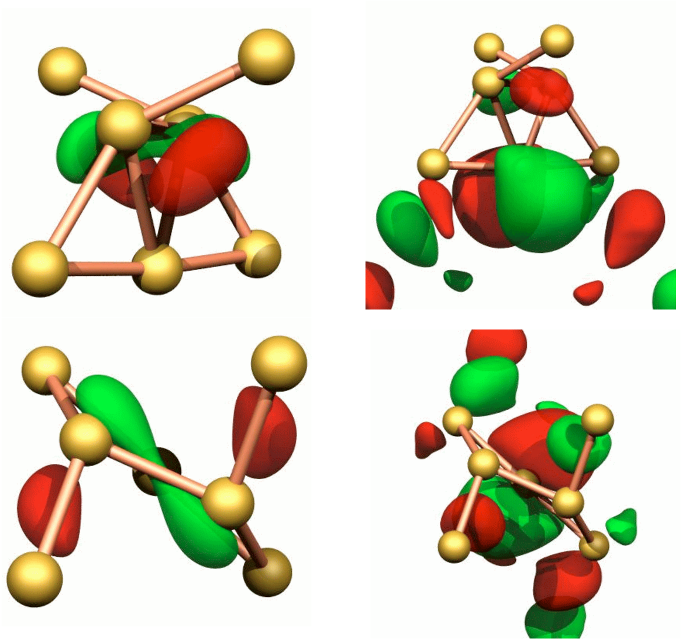

Figure 7.7: Isosurface plots of the highest occupied (Left) and lowest unoccupied wavefunction of I_2^0 III.

III: Structural optimisation of the defect originally proposed by Lee *et al* [4] was performed with the symmetry constrained to C_2. The relaxed defect in the neutral charge state is of the form shown in Fig. 7.3(III). The relaxation is considerable. Most notably, the two equivalent atoms which lie on the [001] axis rotate about C_2 so that they approach the [011] direction. Thus the optimised structure is closely related to the Kim structure but the defect symmetry is now in agreement with that of the P6 EPR centre.

	negative		neutral			positive			
bond	I	III	I	II	III	I	II	III	
a	2.43	2.26	2.45	2.37	2.26	2.47	2.38	2.35	
b	2.43	2.24	2.43	2.39	2.23	2.47	2.43	2.27	
c	2.30	2.39	2.25	2.33	2.36	2.27	2.36	2.36	
d	2.42	2.33	2.57	2.17	2.35	2.55	2.24	2.39	
e	2.35	2.33	2.37	2.34	2.34	2.37	2.33	2.37	
f	2.34	-	2.32	2.31	-	2.32	2.31	-	
g	-	-	-	2.33	-	-	2.43	-	-

Table 7.4: Bond lengths of I_2 defects. The bond labels $a-g$ (Å) are explained in Fig. 7.3.

The KS eigenvalues are shown in Fig. 7.4 and are similar to those of the Kim structure (I). The defect is calculated to possess a donor level and acceptor level at $E_v + 0.88$ and $E_c - 0.16$ eV respectively. The highest occupied wavefunction of the neutral defect is plotted in Fig. 7.7 (Left). Clearly the wavefunction is localised largely upon the two equivalent atoms at the defect core. Mulliken analysis places 18% of the wavefunction at each of these sites with less than 3% at the unique site. This is in contradiction to the hyperfine analysis results of P6 where the major part of the unpaired wavefunction is localised upon the unique atom. Thus although the defect symmetry and structure is consistent with P6, the unpaired wavefunction of the positive charge state is at odds with the hfs of P6.

In the negative charge state we would expect the unpaired wavefunction to be of the form shown in Fig. 7.7 (Right) which depicts the lowest unoccupied wavefunction of I_2^0 (III). This wavefunction corresponds very well to the observed data on the P6 centre. We find that 25 % of the wavefunction lies at the unique site and 3 % is localised upon the two equivalent sites which are connected to the unique site by bond e in Fig. 7.3.

The total energies of the di-interstitial defects are given in Table 7.5. In the positive and neutral charge states, structure II is calculated to be lowest in energy. Supercell results using AIMPRO [91] agrees with this result for the neutral charge state, finding structure II to be 0.08 eV lower than I and 0.98 eV lower than III. In the positive charge state, structure I becomes lowest in energy with structures II and III 0.19 and 1.1 eV higher in energy. Defect II was not optimised in the negative charge state because the calculations predict no acceptor level. The energy difference between structures I and

III was calculated to be 0.6 eV with structure I lowest in energy. This last result differs greatly from the cluster result. Furthermore, the structure of defect III is different from that calculated using the cluster method. The defect relaxes into C_{2v} symmetry. The discrepancies between the energies and structures calculated using the supercell and cluster codes are not usually so great and probably results from a rather flat energy surface for intraconversion between different interstitial structures. The energetics arising from the supercell method are generally the more reliable values.

7.5 Conclusions

Three low-energy di-interstitial defects were investigated. These structures were chosen because they relate closely to those suggested previously by both theorists and experimentalists. In each case the electrical levels were calculated and the character of the wavefunctions pertinent to the unpaired electron of relevant charge states was assessed. We can make several conclusions:

Charge state	I	II	III
-	+0.12	–	0.0
0	+0.75	0.0	+0.58
+	+0.27	0.0	+0.14

Table 7.5: Energies (eV) relative to the lowest energy defect of the charge states of the di-interstitial models in silicon I-III calculated using AIMPRO cluster code.

- There are *two* low energy di-interstitial structures which possess C_{1h} symmetry. Whilst the unpaired wavefunction of I_2^+ (I) is consistent with the P6 hyperfine data, the defect symmetry excludes it from being P6.
- The defect structures proposed by Lee and Corbett [6, 90] are not stable but one quite low energy defect with C_2 symmetry (defect III) results from the optimisation. The wavefunction of the positive charge state, however, is inconsistent with the hyperfine measurements of P6.
- The electrical level calculation shows that defects I and III can be negatively charged. Importantly, defect III has the correct symmetry and unpaired wavefunction localisation to explain P6.

Thus the only structure and charge state which can explain the low temperature symmetry and hyperfine character of P6 is defect III in the negative charge state. Whilst this result is encouraging there are still difficult issues unresolved. In particular, the defect model must explain the observed charge state and reorientation kinetics but also should be very low in energy compared with the other di-interstitial models.

Although the charge state of the P6 defect has been suggested to be positive, there appears to be no good reason for the assignment. The defect is observed in intrinsic (dopant concentration $< 10^{12}\mathrm{cm}^{-3}$), p-type ($1.1 \times 10^{16}\mathrm{cm}^{-3}$) and n-type ($1.6 \times 10^{16}\mathrm{cm}^{-3}$) neutron irradiated material [83]. In fact, the initial doping concentration has no observable effect on the resistivity of the neutron irradiated material and so the dopant level is no indicator of the Fermi-level position. Furthermore, the observation of two charge states of the divacancy in irradiated n-type Si has demonstrated that the Fermi-level varies from region to region within the crystal [11]. Thus the possibility that P6 arises from the negative charge state of the di-interstitial can be easily reconciled with the experimental observations. The calculation of the level positions of defect III however indicate that the acceptor level lies within 0.2 eV of the conduction band edge. Thus it seems unlikely that the defect would be observed in the negative charge state in p-type Si.

Chapter 8

The tri-interstitial

8.1 Introduction

Having looked at the low energy di-interstitial structures in the previous chapter we now turn to the tri-interstitial. The experimental evidence which is considered in relation to tri-interstitial will be two-fold (i) The P6 EPR centre : we have seen that the identification with a di-interstitial is not conclusive and there is a possibility that a tri-interstitial defect may satisfy the experimental observations. (ii) The W-optical line. The origin of this prominent centre is a subject of ongoing debate. Evidence arises from the calculations that a tri-interstitial defect may be linked to this centre.

8.2 Background

The W-centre is formed by electron [92], neutron [93], proton [94] or heavy ion [95] irradiation of Si containing a wide range of different impurities. The optical centre first appears following annealing at around room temperature and is stable up to about 320°C. Because of the general conditions under which the centre is formed, it is thought to be an intrinsic centre.

Vibronic band fine structure associated with the optical peak reveals that the defect has an LVM at 564 cm^{-1} (70.0 meV). Satellite bands arising from ^{29}Si and ^{30}Si are shifted by 8 and 16 cm^{-1} respectively from the ^{28}Si phonon replica. These shifts are surprisingly large and are close to the expected shifts (10 and 19 cm^{-1}) of the Raman line in Si, when *all* the ^{28}Si atoms are replaced by ^{29}Si or ^{30}Si. This led Davies [93] to suggest that the local mode was produced by a single atom vibrating against its neighbors.

There have been other suggestions that the W-centre is a vacancy related species such as the divacancy V_2 [96]. The assignment of the divacancy to the W-line resulted from an investigation of the binding energies of noble gases with V_2.

Implantation of Noble gas (NG) atoms into Si gives rise to photoluminescence centres which bear a close similarity to the W-line spectrum. The He, Ne, Ar, and Kr related spectra consist of a zero-phonon line shifted from the W-line energy by just a few meV. The zero-phonon lines are shifted to lower energy and lie at 1012 (He), 1014 (Ne), 1009 (Ar), 1004 (Kr) and 1001 (Xe) meV. The vibronic side bands are very similar in form to that of the W-line. Moreover, the symmetry of each of these centres has been found to be trigonal with the exception of the Xenon related defect which is said to have tetragonal symmetry.

The most likely explanation of these NG related defects is that the NG atoms lie close to the defect which is responsible for the W-line, thereby perturbing it by a small amount without being chemically bonded into the lattice. Although it has been suggested that NG-Si bonds are formed [97], arguments based purely on strain can approximately reproduce the observed zero phonon line shifts [93]. Given the inert nature of the NG atoms the strain argument appears favourable. Xe may be an exception as is known to form compounds with elements which have high electron affinities [96]. This difference in the propensity to form bonds explain the different symmetry of the Xe centre.

Experiments involving the implantation of Si using a NG ion beam has provided further valuable information concerning the NG related W-line defects [95]. Following ion beam etching, the samples require annealing before the appearance of the NG spectra. For the He case annealing at 150°C produces the spectrum whilst, following Ne, Ar or Kr implantation the spectra were not observed until a 250°C anneal was performed. The binding of the He atom to the W-line defect was shown to be weak as annealing at temperatures higher than 150°C resulted in the disappearance of the Ne line and corresponding growth of the W-line. This suggests that the He atom diffuses away from the W-centre with a thermal activation energy corresponding to $\sim 150°$C.

These experiments also demonstrated the existence of a threshold energy to the creation of the Ne, Ar and Kr defects. The energy required to creating a Frenkel pair has been approximated experimentally to be 25 eV [11]. From the threshold energies for creation, the number of vacancies or interstitials which are required for the formation of the Ar defect was found to be a maximum of four.

One curious finding of the ion-etching experiment was that some NG defects are found to lie more than $1\mu m$ below the ion beam etched surface. This is unusual because the estimated implantation depth of the Ar ions is only a few Å and the diffusion barrier of the large Ar atoms is calculated to be 3.51 eV [96]. Channeling of the atoms can also be excluded as as the surface region is amorphised. The diffusion coefficient required to explain the long range migration of the Ar atoms was determined to be $D \approx 5 \times 10^{-14}$cm^2/s [95]. This extremely high value indicates a complicated athermal diffusion mechanism.

Estreicher *et al* [96] has calculated the binding energies of the NG atoms to the centre of a divacancy. The binding energy is defined as the energy difference between an NG divacancy complex, and the isolated T_d interstitial NG and divacancy. The values were found to be approximately 2 (He), 3 (Ar), 16 (Ar) and 25 (Kr) eV respectively. These results led to the proposal that the W-line is due to the divacancy.

There are a number of problems with this assignment arising from the nature of the divacancy. The divacancy is a well characterised and complex defect. The experimental background and results of AIMPRO calculations is given here.

The divacancy in silicon in both the single positive (V_2^+) and negative (V_2^-) charge states has effective spin $S = 1/2$. This gives rise to a degenerate electronic ground state for the ideal defect thus forcing a Jahn-Teller symmetry-lowering distortion from D_{3d}. Electron paramagnetic resonance (EPR) studies [8] have confirmed the lower symmetry ground state (C_{2h}) for both paramagnetic charge states.

EPR studies [8] identified two spin 1/2 centres in *e*-irradiated silicon, labelled G6 and G7, with V_2^+ and V_2^- respectively. Both centres were found to possess C_{2h} symmetry below 40 K. Above this temperature the signals undergo motional broadening and narrowing effects resulting from thermally activated reorientations of the defect between three equivalent Jahn-Teller distortions. Above 110 K, the effective symmetry arising from the rapid reorientation was observed to be trigonal.

A relaxation of the ideal neutral divacancy in silicon resulted in an inward breathing motion of atoms. Structures are reported in Table 8.1. To simulate the distorted structures of V_2 in silicon, the initial configurations correspond to an inward distortions as indicated in Fig.8.2 (b). Stable inward distortions were located for all charge states of the divacancy in silicon investigated. Importantly, the distortion of the neutral divacancy is found to be strong. This distortion is fully expected as the e_u doublet level is occupied by two unpaired electrons again leading to a Jahn-Teller distortion. The significance of this result is that the W-line, observed at very-low temperatures possesses inherent trigonal symmetry and is therefore inconsistent with the symmetry of the divacancy. Only V_2^{++}

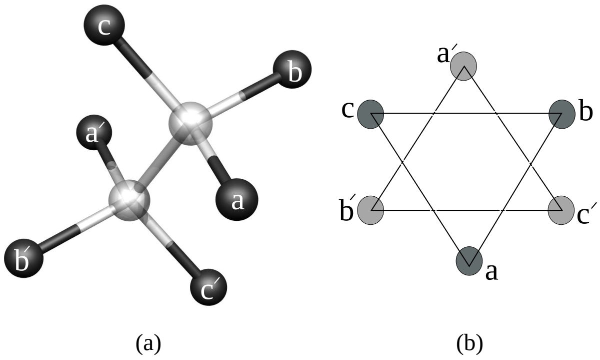

(a) (b)

Figure 8.1: (a) Schematic of the ideal divacancy in silicon. The atoms are labelled following the notation used by Watkins and Corbett[8]. (b) The structure of the divacancy is summarised with a view down the principal [111] axis.

Charge state	D_{3d}	C_{2h}	
		l_{ab}, l_{ac}	l_{bc}
-	3.66	3.71	2.76
0	3.71	3.78	2.92
+	3.77	3.92	2.94

Table 8.1: Distances (Å) between atoms surrounding the divacancy for the relaxed D_{3d} and C_{2h} structures in silicon and diamond. Distances are given with reference to Fig. 8.1.

and V_2^{--} could have D_{3d} symmetry as they possess non-degenerate ground states. The former charge species is unknown and the latter is only stable when E_f is greater than $E_c - 0.2$ eV. This charge state can be eliminated as the W-line defect can be detected in irradiated p-Si. There remains the possibility that the excitonic state of the divacancy possesses D_{3d} symmetry explaining the trigonal nature of the W-line. This explanation is not adequate however. The excitonic state either involves a positively charged defect trapping a weakly bound electron, or a negatively charge defect trapping a weakly bound hole. In both cases the e_u level is partially occupied supporting a distortion to lower symmetry.

On symmetry grounds then it is difficult to explain an identification of the divacancy with the W-line. Electronic structure considerations also make the assignment questionable. For any simple point defect there are two pictures which can be used to explain the optical transition shown in Fig. 8.3. Either the transition is due to the promotion of an electron or hole from one defect localised state to another (intradefect transition) or the

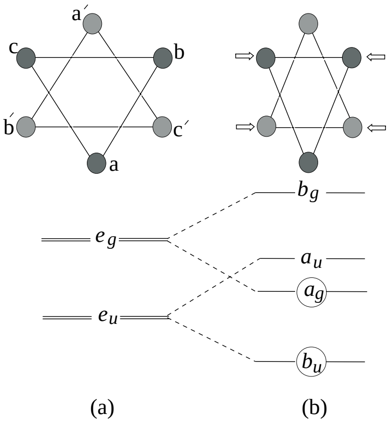

Figure 8.2: The effect of a symmetry lowering pairing distortion to C_{2h} on the one-electron levels of the ideal, D_{3d} divacancy. For clarity, circles indicate the orbitals with finite amplitude on the defect mirror plane (a) The D_{3d} structure. (b) The large pairing, distortion to C_{2h} symmetry. A bond is formed between the two atom pairs b, c, and b′, c′ such that the distances $l_{ac} = l_{ab} > l_{bc}$ and $l_{a'c'} = l_{a'b'} > l_{b'c'}$.

transition occurs between a localised defect state and a near band edge state (excitonic transition). In the latter case, an electron (hole) is promoted to the conduction band leaving a positively (negatively) charged defect. In this charge state a shallow level becomes existent. The conduction band electron (valence band hole) is then trapped by the shallow state and radiative recombination occurs subsequently. There are several cases of excitonic transitions, e.g. the carbon interstitial 856 meV line. In such cases the transition energy, minus the bandgap energy should be equal to the donor (acceptor) level plus a small correction, δ, due to the energy of the excitonic state. For the carbon interstitial we have $1.16 - 0.856 \sim 0.28 + \delta$. So here the binding energy of the exciton is $\sim$ 30 meV. In the case of an intradefect transition, the energy difference between the highest occupied level and lowest unoccupied level in the neutral charge state should approximate to the transition energy. The divacancy is calculated to possess four one-electron levels within the bandgap which give rise to the experimentally determined donor/acceptor levels[1]. Given the crowded nature of the band gap it is difficult to demonstrate how a transition with energy 1.018 eV could arise.

There is one other serious problem with the assignment of the W-line to the divacancy. The one-phonon replica corresponds to a local vibrational mode with frequency 564 cm^{-1}.

---

[1] The electrical levels of the divacancy have been determined to lie at (0/+): $E_v + 0.19$, (-/0): $E_c - 0.42$, (=/-): $E_c - 0.23$ [98, 99, 100]

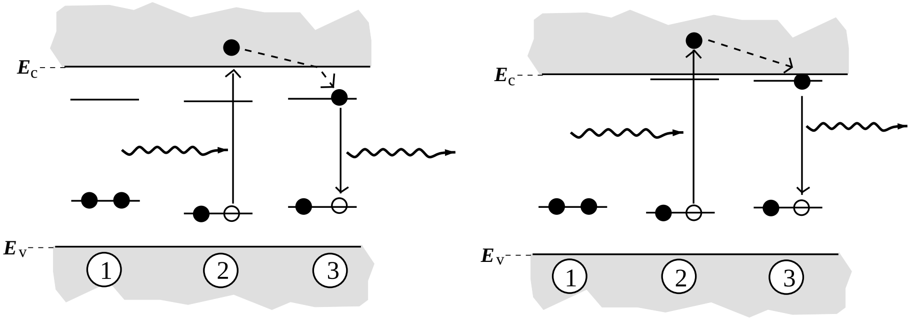

(a) intradefect transition

(b) excitonic transition

Figure 8.3: Possible mechanisms for optical transitions associated with point defects.

General considerations suggest that the broken bonds in all V_n defects will attempt to rebond in pairs and this reconstruction results in an inward movement of the core atoms. In turn, this leads to lengthened back bonds with reduced force constants. Such bonds cannot sustain a vibrational mode above the Raman frequency. The only V_n defect known to possess trigonal symmetry is V_6 but this has been connected with the 1.108 eV PL (J-line) [12]. Moreover, the stress response of V_2, and V_6 on one hand, and the W-centre on the other, are quite different.

We now consider the possibility that the W-line spectrum is due to self-interstitials. There are indications, see above, that the centre contains no more than 3 or 4 interstitials. To obtain a trigonal defect, either atoms are inserted along the [111] axis or at least three atoms are added off the axis. The I_1 model can be rejected from the high thermal stability of the centre and because the defect is first observed only after annealing at around $50 - 100°$ C. One possible model arises from placing three atoms at the centre of bonds parallel to the [111] axis as shown in Fig. 8.5. This structure can undergo a reconstruction which eliminates all dangling bonds and leads to a novel form of I_3.

Other models for the tri-interstitial are considered in this chapter. One model (Fig. 8.4 (II)) is studied as this structure has been identified conclusively with I_3 in diamond (see Chapter 10). Given the obvious similarities between the diamond and silicon systems it is appropriate to compare the energy and properties of this defect with other candidates. Moreover, this structure has C_2 symmetry, and is therefore a potential candidate for the P6 EPR centre discussed in the previous chapter.

Two other models are studied in detail. Both structures have resulted from molecular dynamics simulations and they are very similar in nature. The structures reported by Colombo [9] and Estreicher [96] are shown in Fig. 8.4 (III) and (IV) respectively. A surprisingly small movement of atoms converts one structure into the other.

8.3 Method

The wave-function basis consisted of independent s and p Gaussian orbitals with four different exponents, sited at each Si site. A fixed linear combination of two Gaussian orbitals was sited on the terminating H atoms. In addition, a Gaussian s and p orbital was placed at each Si–Si bond centre. The charge density was fitted with four independent Gaussian functions with different widths on each Si atom and three on the terminating H atoms. One extra Gaussian function was placed at each Si–Si bond centre. The positions of all bulk atoms were optimized. Electrical levels were calculated using the method described in Chapter 4. Cluster size dependence was checked by relaxing the I_3 (I) defect proposed here in three clusters with configurations $\mathrm{Si}_{81}\mathrm{H}_{70}$, $\mathrm{Si}_{187}\mathrm{H}_{116}$, $\mathrm{Si}_{289}\mathrm{H}_{144}$. Furthermore, two of the relaxed structures are compared with those found using a Si_{131} supercell. Bond lengths in the defect core were found to vary by less than 2% between all calculation methods.

8.4 Results

Four structures labelled I-IV were considered in the investigation of I_3 (see Fig. 8.4). We describe their geometries now: (I) Three atoms are placed at bond-centred positions surrounding a tetrahedral interstitial site, symmetry, C_{3v}.(II) Three [001] split-interstitial pairs placed at next nearest neighbor positions, symmetry, C_2. (III) A substitutional atom is replaced by four atoms, symmetry, T_d [101, 9]. (IV) Three atoms arranged as an equilateral triangle are placed surrounding a Si–Si bond centre, symmetry, C_{3v} [10].

I: Structure (I) has the remarkable property that all dangling bonds are eliminated although some bond angles are severely distorted. Although this defect is not the lowest energy, the fully bonded structure suggests that it lies within a substantial energy well, requiring a large energy for dissociation. We consider this structure as a candidate for the W-line. Calculated bondlengths are given in Table. 8.2 for the I_3 defect optimised using both cluster and supercell approaches. Similar structures are calculated in each case. In particular, three atoms are arranged in an equilateral triangle at the defect centre and so there are 60° angles between bonds. The charge density distribution in these bonds is, however, almost indistinguishable from that of an ordinary sp^3 bonding orbital. The

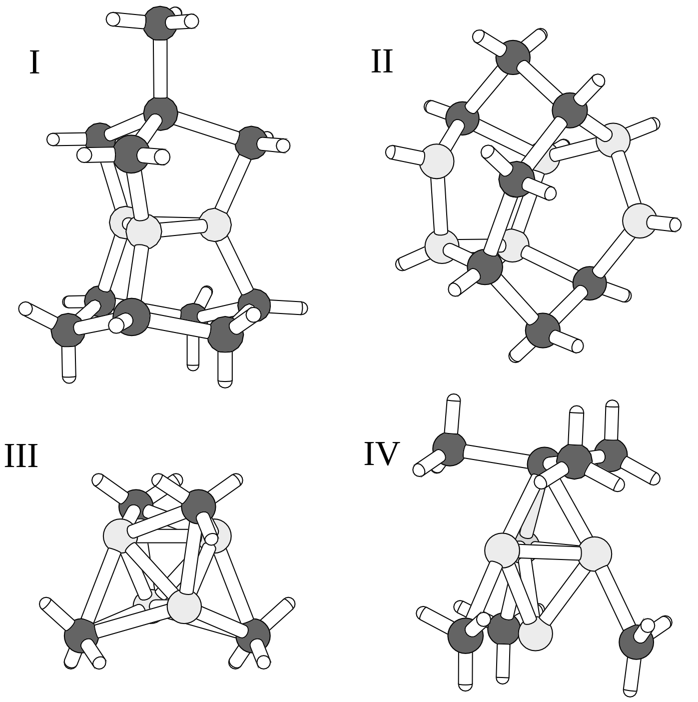

Figure 8.4: Structures of I_3 defects considered. In each case the atoms lying close to their lattice sites are shaded dark grey. I: Three atoms placed at bond centered positions surrounding a tetrahedral interstitial site (C_{3v} symmetry). II: Three [001] split-interstitial pairs placed at next nearest neighbor positions (C_2 symmetry). III: A substitutional atom replaced by four atoms (T_d symmetry) [9]. IV: Three atoms arranged as an equilateral triangle surrounding a Si–Si bond center (C_{3v} symmetry) [10].

bonds joining the inserted atoms are all compressed but, of particular interest, are the bonds of atom *ab* (Fig. 8.5) lying on the C_3 axis. These are compressed by 7 %. These short bonds lead to increased force constants giving rise to several local modes. These modes were evaluated by finding the energy second derivatives between the core atoms using both the cluster and supercell method. The frequencies were then found in the usual way, calculating explicitly the energy double derivatives of 17 core atoms. Now the observed one-phonon replica must have A_1 symmetry, and the highest three modes with this symmetry calculated using the cluster (supercell) methods lie at 633.2 (648.8) , 586.4 (561.3) and 572.0 (549.3) cm^{-1} . Although none of these modes is found to shift greatly upon the replacement of any unique atoms with ^{30}Si, another explanation for the apparent 16 cm^{-1} shift of the one-phonon replica of the W-line arises. We label the 586.4 (561.3) and 572.0 (549.3) cm^{-1} modes A and B respectively. Both modes arise from vibrations involving oscillations of bond *ab* (see Fig. 8.5) and the triangle of atoms at the defect centre labelled *d*. The higher mode (A) is due to an in-phase motion of the two oscillations whereas the lower mode (B) is due to their out-of-phase oscillation. The localization of these modes on these atoms is highly sensitive to the isotopic mass of atom *b* as shown in table 8.3. If the zero-phonon transition was particularly sensitive to oscillations localised on bond *ab* it is likely that this transition would couple to the mode which induces the largest amplitude on this bond. The calculations show that the localisation of modes A and B on *ab* is dependent on the mass of atom *w*. It is possible then that the apparent isotopic shift of a single one-phonon mode from 564 to 548 cm^{-1} may be due to the coupling of the zero phonon line to two different modes dependent upon isotopic mass. Alternatively, the large shift may result from the two modes interacting so that the large frequency shift of the observed mode has two causes; (i) directly from the change in mass of atom *a* and (ii) from the increased interaction with the nearby mode. The exact magnitude of the coupling of the two modes is not well modelled by the calculations.

The Kohn-Sham spectrum reveals a fully occupied *e*-doublet lying at $\sim E_v + 0.4$ eV with an a_1 singlet level lying slightly lower in energy. Transition state calculations of the many-body electrical levels predict that a donor level exist at $E_v + 0.09$ eV. No acceptor level is calculated within the band edges consistent with the luminescent energy of the W-line.

Viewing the structure of I_3 along $[1\bar{1}0]$, reveals that the defect is nothing more than a 3-membered chain of $[1\bar{1}0]$ interstitials. Such chains have a special significance in the

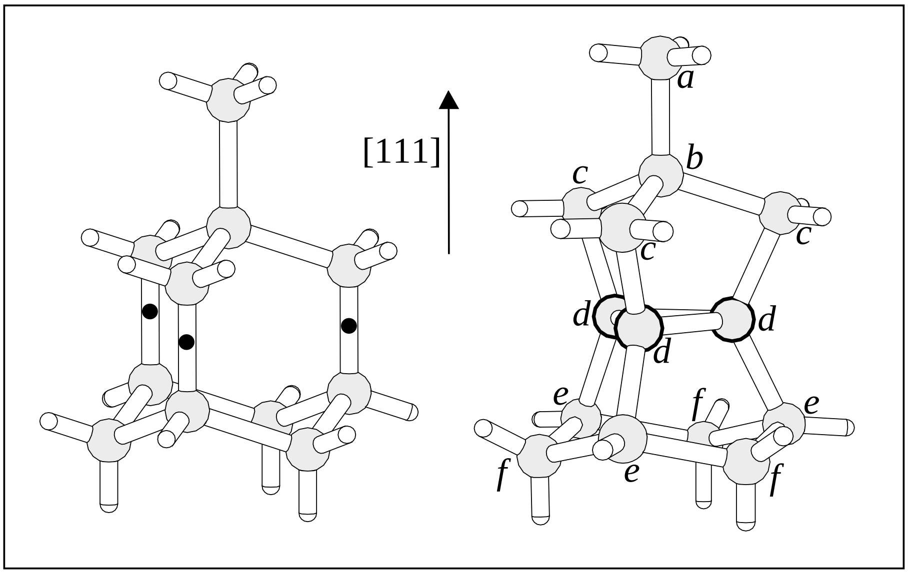

Figure 8.5: Schematic showing the structure of I_3 (I). **Left:** A section from the ideal silicon structure. To form I_3, three atoms are placed in bond centred positions indicated by the filled circles. **Right:** The fully optimised structure of I_3. For clarity, the three bond-centred interstitial atoms are shown in bold.

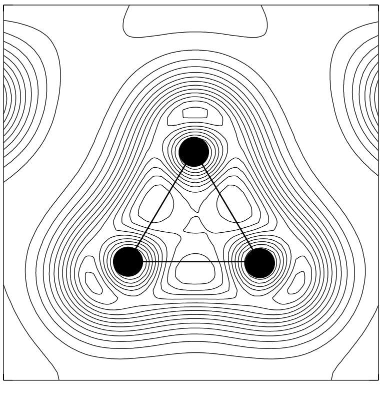

Figure 8.6: Contour plot of the charge density in a plane containing the three equivalent atoms at the defect core of the open form of I_3. The contours indicate that the bonds are close in character to the ideal Si-Si covalent bond.

	$Si_{88}H_{64}$	$Si_{188}H_{116}$	$Si_{290}H_{144}$	Si_{131} supercell
ab	2.17	2.17	2.18 (+2.9%)	2.19
bc	2.38	2.37	2.42 (−7.7%)	2.36
cd	2.15	2.17	2.17 (−3.4%)	2.17
dd	2.27	2.26	2.27 (−6.8%)	2.27
de	2.18	2.18	2.19 (−6.8%)	2.20
ef	2.35	2.32	2.33 (−0.9%)	2.31

Table 8.2: Calculated bondlengths of I_3 (I) showing convergence of the structure with system size and method employed. Bondlengths are given with reference to Fig. 8.5. For the largest cluster, variation of the bondlengths from the ideal Si–Si bondlength (2.35 Å) are given

understanding the structure of extended {311} interstitial defects. These are formed by irradiation of Si, followed by a heat treatment at around 500° C. High resolution transmission electron microscopy studies [102] have resulted in the construction of a comprehensive structural model of the defect. The principal structural unit in the defect is a chain of interstitials lying along [110]. This chain can be inserted so that no dangling bonds are produced except at the ends of the chains. Uniquely, in I_3, the two dangling bonds at the ends can be linked together creating a stable defect.

II: This defect was optimised in both a cluster and a supercell. The structure is produced by replacing three next-nearest neighbour atoms which lie in a {001} plane by ⟨001⟩ split interstitial pairs. Some reconstruction of the resulting dangling bonds can be made so that the relaxed structure possesses only two under-coordinated atoms. In both the cluster and supercell cases the atomic structure was found to be similar to that calculated in diamond (see Chapter 10) with the exception that the two three-fold coordinated atoms move towards the unique atom. This result is wholly expected. Carbon atoms have a propensity for sp^2 bonding (as in graphite) which involves three fully coordinated bonding orbitals which lie in a shared plane with the atom, and a p-orbital orthogonal to the plane. Thus, in diamond, we expect the three-fold coordinated atoms to lie co-planar with their bonded neighbours, as found. Silicon atoms do not share this propensity and, as seen in the vacancy and divacancy, the sp^3 bonding is maintained in under-coordinated defects with three tetrahedral bonding orbitals and a fourth 'dangling bond' orbital. This is the situation calculated for the C_2 defect (II).

Method	Isotope	Vibrational mode	
		A	*B*
$Si_{188}H_{116}$ cluster	(i)	586.4 (0.102)	572.0 (0.093)
	(ii)	582.4 (0.063)	565.7 (0.113)
Si_{131} supercell	(i)	561.3 (0.135)	549.3 (0.035)
	(ii)	553.2 (0.094)	547.4 (0.085)

Table 8.3: Isotopic behaviour of vibrational modes of I_3 in silicon calculated using cluster and supercell method. In each case the vibrational modes frequencies (cm^{-1}) are indicated when (i) all atoms are ^{28}Si and (ii) atom *b* (Fig. 8.5) is replaced by ^{30}Si. The localisation of each mode on atom *a* is given in braces.

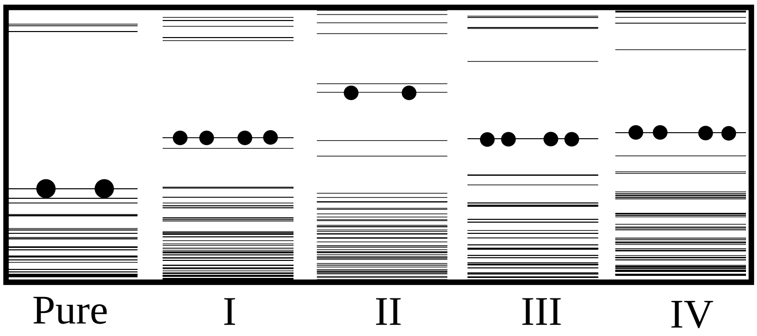

Figure 8.7: KS eigenvalue plots of I_3 defects in silicon. The pure cluster eigenvalues are shown for comparison. The labels I-IV refer to Fig. 8.4

One potential result is that the electrons occupying the dangling bond orbitals overlap substantially with the unique atom, explaining the hyperfine data observed for P6 i.e. high unpaired wavefunction amplitude on the unique atom, and a small fraction on two equivalent atoms.

Two calculations were performed which allow us to exclude defect II as a candidate for the P6 EPR centre: (i) Characterisation of the unpaired wavefunction of the positive charge state and (ii) Calculation of the reorientation barrier. The result of the former calculation is shown in Fig. 8.8. It is clear that the unpaired electronic wavefunction of the positive charge state is largely localised on the two equivalent atoms (the 3-fold coordinated atoms), with a small amplitude upon the unique atom (centre of Fig. 8.8), in contradiction with the P6 data. Mulliken analysis places just 5% on the unique site, with 38% localised over the two 3-fold coordinated atoms. The negative charge state can be

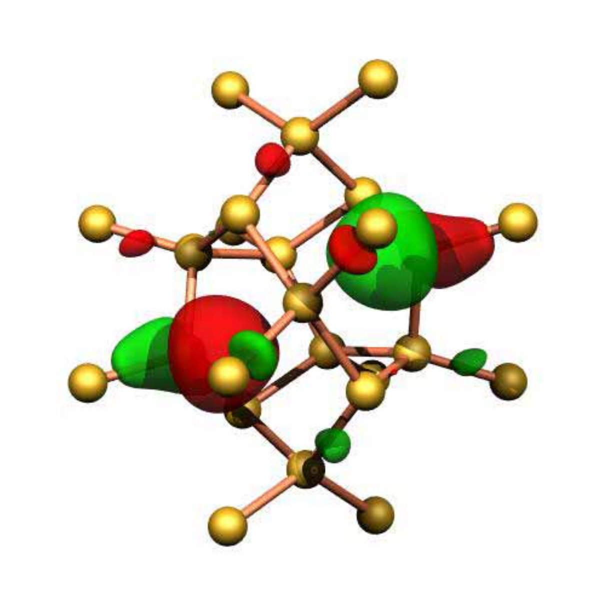

Figure 8.8: Isosurface plot of unpaired wavefunction of I_3^+ (II). The C_2 axis of the defect points directly out of the page.

excluded as this corresponds to the filling of the antibonding state of the dangling bond orbitals.

The reorientation barrier of the C_2 defect was also considered in relation to the low observed reorientation barrier (0.15 eV) of P6. Reorientation of the C_2 structure involves a mid-point structure with C_{1h} symmetry. Supercell calculations of the relative energies of the C_2 and C_{1h} structures show that the mid-point structure is *lower* in energy than the C_2 structure. Therefore it is unlikely that the C_2 structure would be even meta-stable as a lower energy defect exists which is very close geometrically.

III: Defect structure III, suggested by Colombo *et al* [9] possesses T_d symmetry and was optimised in two clusters. The bonds shown in Fig. 8.4 can be reduced to a set of just two inequivalent bonds. These are of length 2.38 and 2.49 Å in the optimised defect, substantially longer than the ideal Si-Si bond. It is unusual that the addition of three extra atoms to a single atomic site should result in a defect with bonds longer than bulk bondlength but this is resultant from the spreading of the charge density over the overcoordinated system. This defect would not be expected to support vibrations with frequency greater than the Raman frequency and this expectation has been confirmed by supercell calculations [91].

The KS electronic structure (shown in Fig. 8.7) of this defect is complex. The filled

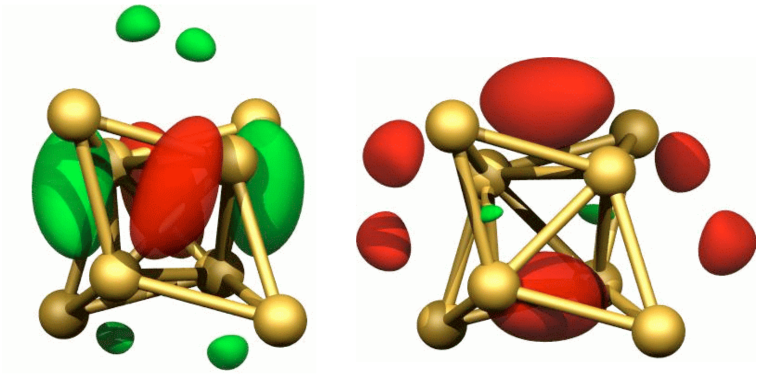

Figure 8.9: Isosurface plot of the highest occupied state of I_3 (III). The state is of e symmetry and the components of the wavefunction calculated by AIMPRO are shown. Negative and positive regions are shown in red and green respectively.

states of the neutral defect are of e, t_2 and a_1 symmetry in order of lowering energy and some possible defect related states lie around the valence band edge. An empty singlet state lies within the band gap. One consequence of this electronic structure is that the positive charge state of the defect would not possess T_d symmetry as a Jahn-Teller distortion would occur. The many-body acceptor and donor levels of this structure are expected to be similar to those of structure IV.

IV: This defect is very similar to defect III but has C_{3v} symmetry. The bondlengths are similar to structure III but some bonds are compressed at the defect core. Calculation of the vibrational modes of this defect show that one local mode lies 40 cm^{-1} above the Raman frequency. The mode is found to shift by less than 1 cm^{-1} when any atom in the defect core is replaced by ^{30}Si.

As for defect III, the highest occupied level in the neutral charge state is an electronic doublet. Since the highest occupied state is filled there is no propensity for a Jahn-Teller distortion. No acceptor or donor level were calculated to lie within the band edges.

The energetics of the defects is shown in Table 8.4. As found for the I_2 defects there is a substantial difference in the energetics of the cluster and supercell methods. The cluster energetics are considered less reliable because, due to their structural nature, the defects are centred at quite different positions within the cluster. This means that the defect-surface interaction may vary widely between two defects. The supercell results show structure I to be quite high in energy as compared with the compact model IV. Estreicher *et al* [103] have reached the same conclusion finding structure I to be 1.7 eV higher in energy than structure III

	Total energy (eV)		
Structure	$Si_{184}H_{116}$	Si_{64} supercell [91]	Si_{219} supercell [91]
I	0.03	1.47	1.54
II	1.26	–	–
III	0.00	0.0	0.0
IV	0.40	0.03	0.17

Table 8.4: Energies (eV) relative to the lowest energy defect of the charge states of the tri-interstitial models in silicon I-IV calculated using AIMPRO cluster and supercell codes.

8.5 Conclusions

Four forms of the tri-interstitial have been studied. The lowest energy defects calculated using the supercell method, structures III and IV are of compact form, with substantial overcoordination of atoms in the defect core. This overcoordination results in weak bonding and hence little local vibrational mode activity is expected for these structures. The IV defect is surprisingly, calculated to be electrically inactive, but states within ~ 0.1 eV of the band-edge are possible given the error of the calculation method. The bonding arrangements are similar to those found for the $\langle 110 \rangle$ split-interstitial discussed in Chapter 6. Given the low calculated reorientation barrier for the I_1 defect, the overcoordinated tri-interstitials can also be expected to reorient and migrate rapidly. This expectation has been confirmed by Estreicher *et al* [103].

The structure identified with the O3 EPR centre in diamond was optimised and found to be high in energy, with a close by, lower energy structure existing. We conclude that this defect is an unlikely candidate for the Si-P6 centre.

The final structure considered is not a very low energy defect according to supercell calculations but has properties which link it with the W-line. The experimental evidence [95] suggests that an unusual process precedes the formation of the NG related W-defects which involves a rapid diffusion mechanism. It is possible that the meta-stable form of the tri-interstitial defect (I) is formed as a by-product of this process. Molecular dynamics simulations have confirmed that I_3 (I) can form from separated $I + I_2$ despite its high energy [103].

One potential explanation of the rapid diffusion of Noble gases is that the Noble gases are trapped by self-interstitials. The self-interstitial defect diffuses rapidly through the lattice, and lowers the barrier to diffusion of the Noble gas atoms. This idea is partially supported by the recent calculations of Estreicher *et al* [103] who has shown that I_2 and I_3 (IV) can diffuse with very low barriers.

Structure I is an appropriate model for the W-centre. The fact that this defect is interstitial rather than vacancy related is favourable as experiments have suggested that interstitials are responsible for the W-line [104, 93]. Additionally, the full four-fold coordination of the structure implies that it is considerably less mobile than other models for I_2 and I_3 explaining the stability of the W-line. This idea has been confirmed by molecular dynamics studies which show that I_3(I) shows no tendency to diffuse even after 1000 K.

The vibrational character of the I_3 (I) defect can also be used to explain the observed one-phonon replica, and its isotopic shift. The large isotopic shift observed, however, is not reproduced directly by the calculations. To explain the shift, we must invoke an argument involving two interacting local vibrational modes.

The energy (1.018 eV) of the zero phonon transition is also explained by the I_3 (I) model. Calculation of the electrical levels shows that a single donor level lies at $\sim E_v + 0.1$ eV. An electronic transition from this state to a state close to the conduction band edge would have energy close to that observed.

In summary, a fully rebonded model for the tri-interstitial represents a strong candidate for the W-line although conclusive identification is lacking. Two compact models, III and IV are optimised and found to be lowest in energy. The weak bonds of these defects supports little local vibrational mode activity and implies low barriers to diffusion.

Chapter 9

The tetra-interstitial in silicon

9.1 Introduction

Recently, evidence has emerged that the structure of small self-interstitial aggregates is markedly different from that of the {311} extended defect. The transient supersaturation of a system undergoing Ostwald ripening has been exploited to estimate the formation energies of small interstitial aggregates [105]. These experiments demonstrated that magic numbers exist for interstitial aggregates in the early annealing stage. I_4 and I_8 are found to be particularly stable with a transition at $n \gtrsim 10$ to a broad range of defects with the characteristic energy of {311} condensates. Furthermore, optical studies [106] confirm this picture, indicating that a structural transformation from I clusters to {311} defects occurs at ~ 600°C.

9.2 Background

Deep level transient spectroscopy (DLTS) studies of Si ion implanted silicon has also provided information on the early stages of the ripening process [107]. Two donor (0/+) levels at $E_v + 0.29$ eV and $E_v + 0.48$ eV associated with small interstitial clusters are found to dominate the DLTS spectrum before the emergence of a different DLTS signal at $E_v + 0.50$ eV. The latter level exhibits carrier capture kinetics typical of extended defects and is associated with {311} condensates. The $E_v + 0.29$ eV level has been observed previously in carbon implanted silicon and was correlated with the EPR centre labelled B3 [76].

B3 is a prominent $S = \frac{1}{2}$ centre, observed in boron doped, neutron irradiated and heat-treated silicon [84, 108]. It is first observed upon annealing at around 200°C and

	g_1	g_2	g_3	θ
[108]	2.0159	2.0051	2.0051	90°
[84]	2.0166	2.0054	2.0054	90°

Table 9.1: Tabulation of g-values determined from the B3 spectrum in silicon.

completely anneals out at 500°C [108, 84]. B3 is one of only eight defect centres observed in irradiated silicon which have been reported to possess D_{2d} symmetry and its presence to high temperatures suggests a remarkably stable, simple secondary irradiation product. The centre is observed in very high concentrations (5×10^{16} cm^{-3}) under optimum conditions. Extensive studies of the B3 centre [84] showed that it exists in the positive and neutral charge states with $S = 1/2$ and $S = 0$ respectively and also that the symmetry is not resultant from Jahn-Teller distortion.

Since the concentration of the defect is much larger than the oxygen or carbon concentrations detected in the samples used, the defect is assumed to be intrinsic. Additionally, no hyperfine interaction due to impurity atoms could be detected. The defect is not thought to be vacancy related for two key reasons. Firstly, only V_1 and V_5 amongst the small vacancy aggregates could possess D_{2d} symmetry, but in conflict with the observation, these could only result from Jahn-Teller distortions. Secondly, vacancy defects possess hyperfine character which reflects the high electron localization on $\langle 111 \rangle$ dangling bonds whereas the B3 centre in no way reflects this degree of localisation.

Analysis of the hyperfine structure reveals further information about the defect structure: (i) the defect centre is probably vacant (ii) two equivalent Si atoms lie along the [001] axis. (iii) only 9% of the unpaired electron is localized on each of these two atoms and (iv) the electronic wavefunction is predominantly p-like with only 6% s character.

The structure for I_4 investigated here as a model for the B3 EPR centre was proposed previously, originally as a candidate building block for extended defects observed in irradiated diamond [109] and subsequently as a model for I_4 in silicon [110, 5]. The I_4 defect is constructed by replacing four next-nearest neighbour atoms which lie in a common $\{001\}$ plane with four $\langle 001 \rangle$ split interstitial pairs (Fig. 9.1). Optimization of the structure demonstrates that each atom pair forms bonds with the neighboring pairs, resulting in full four-fold coordination. The defect possesses symmetry operations which identify it with the D_{2d} point group (see Table 3.1, consistent with the symmetry assignment of the B3 EPR centre.

In the discussion section, the implications of the identification of the B3 EPR centre are analysed. In particular, the properties of I_4 are examined in relation to defect related spectra observed by DLTS, optical and infra-red spectroscopy.

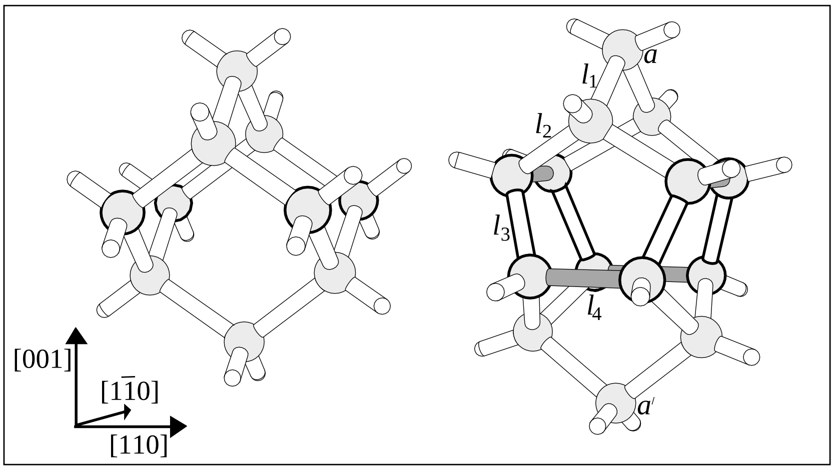

Figure 9.1: Schematics showing the structure of the tetra-interstitial in silicon. Left: A section of the silicon structure. To form the defect, four next-nearest neighbor atoms (shown in bold) are replaced by [001] orientated atom pairs. Right: The fully optimized structure of I_4 in silicon. For clarity, the four [001] split interstitial pairs which make up the defect are shown in bold. The reconstructed bonds which link the interstitial pairs are shaded.

9.3 Method

The interstitial defects are studied with both cluster and supercell methods. The wavefunction basis consisted of independent s and p Gaussian orbitals with four different exponents, sited at each Si site. A fixed linear combination of two Gaussian orbitals was sited on the terminating H atoms. In addition, a Gaussian s and p orbital was placed at each Si–Si bond centre. The charge density was fitted with four independent Gaussian functions with different widths on each Si atom and three on the terminating H atoms. One extra Gaussian function was placed at each Si–Si bond centre. The positions of all bulk atoms were optimized. Electrical levels were calculated using the method described in Chapter 4. Cluster size dependence was checked by relaxing the I_4 defect proposed here in three clusters with configurations $Si_{88}H_{64}$, $Si_{188}H_{120}$, $Si_{290}H_{144}$. Furthermore, the relaxed structures are compared with that found elsewhere using a Si_{196} supercell. Bond lengths in the defect core were found to vary by less than ∼ 2% between all calculation methods.

9.4 Results

The calculations show that I_4^0 possesses bond lengths and bond angles close to their ideal values (2.35 Å and 109.47° respectively), in agreement with previous *ab initio* calculations [5]. In particular, the bond angle distortions in the defect core of I_4 relaxed in the $Si_{290}H_{144}$ cluster were found to be within the range −0.9 to −11.8% of the ideal bond angle compared with −1.3 to −13.2% found using a 196 atom supercell [5]. The bond lengths of the neutral and positive charge states are given in Table 9.2. Also shown are the bond lengths of the defect relaxed in a 196 atom supercell [5]. All bondlengths are calculated to be within 5% of the bulk value (2.35 Å), supporting the assertion that this is a remarkably stable defect. Also note the good agreement between the cluster and supercell results.

Bond	$Si_{84+n}H_{64}$	$Si_{184+n}H_{120}$	$Si_{286+n}H_{144}$	Si_{196} supercell [5]
l_1	2.27	2.26	2.27 (−3.4 %)	(−2.7 %)
l_2	2.29	2.29	2.30 (−2.1 %)	(−1.7 %)
l_3	2.21	2.22	2.24 (−4.7 %)	(−3.2 %)
l_4	2.39	2.34	2.36 (+0.4 %)	(−0.3 %)

Table 9.2: Calculated bondlengths of I_4 in three cluster sizes compared with Si_{196} supercell [5] results. Bondlengths l_{1-4} are given with reference to Fig. 9.1. For the largest cluster used the deviation from the ideal Si–Si bondlength (2.35 Å) is given.

Since the defect possesses D_{2d} symmetry, it is a potential candidate for Jahn Teller distortion. Investigation of the Kohn Sham electronic levels of the relaxed defect (see Fig. 9.3), however, shows that the highest occupied level is an orbital singlet and thus the centre would not be Jahn Teller active for the 0, +, 2+ charge states. Two electronic levels lie in the lower half of the band gap. Possible shallow one-electron levels lie close to the conduction band edge. The calculated many-body electrical levels of the centre reveal that the defect possesses no acceptor level but a donor level does exist.

The position of the donor level of I_4 was found by comparing the ionisation energy of I_4 with that of the carbon-interstitial which has an experimentally determined donor level at $E_v + 0.28$ eV [31]. The calculations were performed in all three clusters and the I_4 ionisation energy was found to be $0.01 - 0.12$ eV higher than that of the carbon-interstitial placing the I_4 donor level between $E_v + 0.16$ and $E_v + 0.27$ eV (see Table 9.3). This result is consistent with the correlation of the $E_v + 0.29$ eV hole trap with the B3 centre [76]. No other electronic levels are calculated to lie within the band gap. This determination of an electrical level associated with I_4 is in contradiction with previous results [5] and is probably resultant from the more reliable electronic level calculation method employed here. The association of a donor level with this fully-coordinated structure may be expected as a result of the compressive strain in the defect core. The compression of bonds leads to increased interaction between sp^3 orbitals on next-nearest neighbors, increasing the valence band width and pushing states into the band-gap region. The donor activity then arises from these filled states displaced upwards from the valence band edge. The highest occupied wavefunction of the positive charge state is plotted in Fig. 9.2.

Defect	$Si_{88}H_{120}$	$Si_{188}H_{120}$	$Si_{290}H_{144}$
C_i	-4.9478	-4.7556	-4.6242
I_4	-5.0635 (E_v+0.16)	-4.7680 (E_v+0.27)	-4.7275 (E_v+0.18)

Table 9.3: Calculated ionisation energies of C_i and I_4 in clusters of different size. The values in brackets are the donor level positions resulting from each calculation.

The vibrational modes of the defect were calculated in the $Si_{188}H_{120}$ cluster. The energy double derivatives were calculated explicitly for the first 18 atoms at the defect core. Because of the high symmetry of the defect, and the large number of equivalent atoms at the centre of the defect it is not likely that any of the mode frequencies will be strongly affected by any individual atom being replaced by ^{30}Si or ^{29}Si.

9.5 Discussion

An important characteristic of an anisotropic defect is the stress or piezospectroscopic tensor [25]. The energy of a defect within a strained crystal is $\Delta E = Tr\mathbf{B} \cdot \epsilon$ where $\mathbf{B}$ is a traceless stress tensor. In the absence of any imposed stress, one third of the I_4 defects are aligned along each $\langle 100 \rangle$ axis. Imposing a tensile stress along [001] lowers the energy of those I_4 centres with this orientation and, if the defect can reorientate, leads to a decrease in the numbers of defect aligned along [100] and [010]. Experiment [84] shows

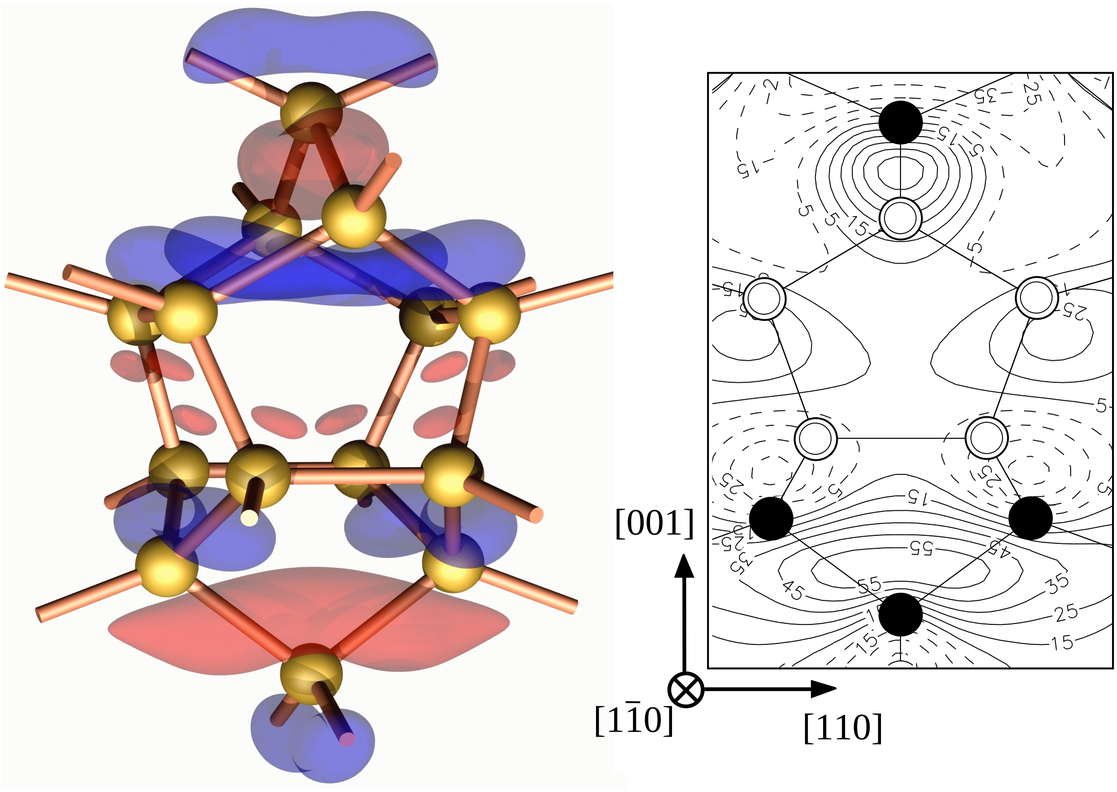

Figure 9.2: Schematics showing the unpaired wavefunction of I_4^+. Left: A 3-dimensional schematic of an isosurface of the wavefunction. Dark (light) surfaces indicate positive (negative) regions of the wavefunction. Right: Contour plot of the unpaired wavefunction on the $(1\bar{1}0)$ plane. Contours representing positive (negative) regions are shown by solid (dashed) lines. Atoms lying in the plane are shown as black circles. Double circles indicate that two atoms lie equidistant from the plane along $[1\bar{1}0]$ and $[\bar{1}10]$.

that a stress of 180 MPa at 350°C along $[\bar{1}10]$, leads to twice the number of B3 centres aligned along [001] as along [100] or [010] [1]. This gives a stress tensor whose principal directions coincide with the cube axes and whose principal values are $B_1 = B_2 = -B_3/2$ with $B_3 = -28$ eV. This tensor was calculated by first relaxing the volume of a 100 atom unit cell containing the defect and then imposing a strain along the cube axes (as described in Chapter 4). The results give $B_1 = B_2 = -B_3/2$ with $B_3 = -33$ eV. The negative value to B_3 means the defect exerts a considerable compressive stress along the principal axis.

---

[1] The intensity of the B3 EPR lines are related to the number of B3 centres orientated parallel (n_A) or orthogonal (n_B) to [001] by $I_A/(I_A + I_B) = 0.7n_A/(0.7n_A + n_B)$. This takes into account the dependence of the transition matrix element on direction of magnetic field

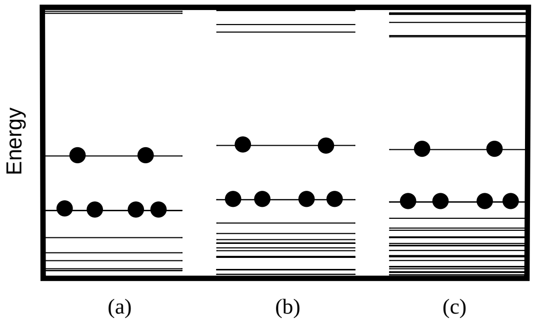

Figure 9.3: The Kohn-Sham electronic levels of the tetra-interstitial in silicon. The levels are shown for the optimised defect in three different (tetrahedral interstitial site centred) clusters: (a) $Si_{88}H_{64}$ (b) $Si_{188}H_{120}$ (c) $Si_{290}H_{144}$

Calc. frequency (cm^{-1})	Symmetry	Localisation	IR active
576.9	e	2.7	Y
574.3	b1	2.6	N
574.0	a1	2.8	N
557.1	b2	2.0	Y
556.5	e	2.1	Y
556.5	a1	2.2	N
553.5	a2	1.2	N
551.4	e	1.5	Y

Table 9.4: Calculated vibrational modes and symmetries for I_4 in silicon. The localisation of the vibrational mode is estimated by calculating the total amplitude squared of the mode on the 14 core atoms as a percentage of the sum of the squares of all the atomic vibrational amplitudes in the cluster.

The formation energy of the I_4 defect, $E_f(I_4)$, relative to four bulk atoms was calculated using the supercell method to be 8.7 eV. Experimental determination of this energy gives a value of around $E_f(I_1) + 3.4$ eV [105]. The formation energy of the isolated $\langle 110 \rangle$ orientated interstitial was calculated $E_f(I_1)$, to be 3.9 eV. This brings the calculated formation energy of I_4 to $E_f(I_1) + 4.8$ eV, in reasonable agreement with the experimental value [105]. The binding energy of I_4 relative to four separated [110] orientated interstitial atoms is calculated to be 6.9 eV.

The high thermal stability of B3 is explained by the low formation energy calculated for I_4. This result is expected from the I_4 model because of the near ideal bonding arrangements of all atoms. The model also explains the finding that I_8 also possesses remarkably low formation energy [105]. Clearly, eight [001] split-interstitial pairs can be sited on a (001) plane resulting in the formation of two neighboring I_4 defects. It is likely that this $(I_4)_2$ defect will possess a lower formation energy per interstitial than two separated I_4 units due to the mutual strain relief interaction between the units. The large increases observed in the formation energies of the defects I_5, I_6, I_7 relative to I_4 and I_8 is also consequent from this model as these intermediate defects are unable to achieve full coordination.

The correlation of I_4 to experimental spectra may possibly be extended to observations in photoluminescence (PL) and absorption. The 1039.8 meV zero phonon line (labelled I_3 or X) is produced by neutron, proton or ion implantation between 230 and 530°C independently of carbon or oxygen doping [111] and has been classified as an intrinsic centre [112]. As with the B3 EPR centre, the X-centre is suggested to have inherent D_{2d} symmetry from stress measurements and consideration of the vibronic bandshape [111]. For the reasons discussed above this symmetry point group is inconsistent with the defect being a small vacancy cluster. The D_{2d} symmetry assignment is however uncertain, as the measurement may have been dominated by the stress response of the conduction band. If this is the case, it would imply that a considerable stress is induced by the defect roughly along [001] but does not identify the defect symmetry.

Isochronal annealing experiments show the 1039.8 meV zero phonon line intensity appears to increase at the expense of another zero phonon line labelled W [113]. The W-optical spectrum is also classified as an intrinsic centre and experiments suggest that is an interstitial rather than a vacancy aggregate [93, 104] (see Chapter 8). This supports the identification of the X-centre with I_4 and suggests that the W-centre is a smaller aggregate, I_2 or I_3 which is the precursor to the I_4 defect.

Calculation of the matrix elements for dipole transitions between the defect states in the band gap region was performed. A number of transitions are allowed between near band edge states with radiative lifetimes around 1–5μs. The fastest of these transitions occurs between states of b_2 and a_1 symmetry. The large $\langle 001 \rangle$ stress response indicates that the X-line transition involves a shallow excited conduction band state, and assuming that the PL arises from a bound exciton, the donor level is placed around $E_v + 0.1$ again consistent with the calculation (~ 0.20 eV but in conflict with the DLTS assignment to B3 [76].

The compressed bonds in the defect core result in increased force constants which are expected to give rise to vibrational modes with frequencies above the maximum lattice frequency (523 cm^{-1}). Infra-red studies [114] of neutron damaged silicon show that two local mode peaks are indeed observed at 530 and 550 cm^{-1} which are attributed to intrinsic defects. These modes are observed following irradiation at 130°C and survive up to ~ 550°C. These annealing temperatures are in reasonable agreement with those of the B3 EPR centre. The local vibrational modes of the optimized I_4 defect were calculated using the cluster method. A series of local modes were calculated to lie within 30 cm^{-1} of the calculated maximum lattice frequency (536 cm^{-1}). The two highest infra-red active modes possess frequencies 577 and 557 cm^{-1} (see Table 9.4).

The calculated electronic and structural properties all support the identification of I_4 with B3 EPR centre. The defect symmetry, D_{2d} matches that of the B3 EPR centre. The defect structure is wholly consistent with the interpretation of the nuclear hyperfine interaction data on B3 [84], having no atom present at the defect centre and two equivalent atoms (labelled a in Fig. 9.1) lying along the principal $\langle 001 \rangle$ axis. The wavefunction occupied by the unpaired electron of I_4^+ is shown in Fig. 9.2. Clearly the unpaired wavefunction is spread over a number of atoms, whilst the largest amplitude lie near atom sites labelled a. Mulliken analysis shows that 6% of the unpaired wavefunction is localized near atom a in excellent agreement with the value obtained from ^{29}Si hyperfine measurements (9%). The unpaired electronic wavefunction is found to be strongly p-like in character consistent with the 94% anisotropic component observed. Hyperfine splitting due to interaction with other nuclei is also observed in the B3 spectrum. These were not resolved and therefore no further detailed information regarding other nearby nuclei could be ascertained. The Mulliken analysis, however, shows that around 3% of the unpaired wavefunction is localized upon each site labelled b and another 3% is localized near the sites labelled c. It is probable that the unresolved hyperfine splitting is a result of interaction with nuclei at sites *b* or at *c*.

9.6 Conclusion

The results of the calculation allow the identification of I_4^+ with the B3 EPR centre observed in irradiated *p*-type silicon. Its formation circumstances, symmetry, structure, electronic character and stress response strongly support this assignment.

The calculated electrical activity is consistent with the correlation of the B3 EPR centre with the 0.29 eV DLTS signal. The calculations support a tentative link of the X-optical centre with the B3 EPR centre and the optical properties of the I_4 defect are calculated to be in reasonable agreement with this assignment. However, it is unlikely that *both* the DLTS assignment and the optical assignment are correct as they appear contradictory: If the X optical centre (transition energy, $E = 1.039$ eV) is due to I_4 then, for this to be an hole-excitonic transition there must exist a donor level at around $E_v + 0.12$ eV. This value is substantially lower than the DLTS level energy of $E_v + 0.29$ eV. Thus further experimental study of these defect spectra is required.

The vibrational properties of I_4^0 were calculated showing that the defect gives rise to a series of local modes lying close to the Raman edge. The highest infra-red active vibrational frequencies lie at 577 and 557 cm^{-1} and could conceivably be identified with two defect modes observed in irradiated Si [114].

The structure of the I_4 centre clearly excludes it as an embryo for aggregation of the $\{311\}$ defects. This marked structural difference between small aggregates and extended interstitial defects, however, is supported by optical, DLTS and transient supersaturation experiments.

Chapter 10

Self-interstitial aggregation in diamond

10.1 Introduction

Diamonds are categorised in terms of their impurity content and in what form the impurities exists. The method of classification was originally developed to assess the gem quality of natural stones and uses the presence, or absence of optical absorption centers. Diamonds containing detectable concentrations of nitrogen are “type I” diamonds whilst nitrogen-free diamonds are termed “type II”. Type I diamonds are further classified depending whether the nitrogen exists as a substitutional defect (type Ib) or as a nitrogen aggregate of some kind (type Ia). Type II diamonds are either very pure (type IIa) or contain detectable concentrations of substitutional boron (type IIb).

The understanding of the behaviour of self-interstitials in diamond is of increasing relevance to industry. This has resulted from the discovery of new potential applications for diamond for use in electronic devices such as particle detectors. One key advantage of diamond-based material for these devices lies with its radiation hardness. Thus, used as a particle detector, the working life could be extended dramatically in comparison with Si-based detectors. Another advantage of diamond over silicon is the high thermal conductivity which may favour its use in high power devices. For such devices, intrinsic defects may be introduced during processing stages such as dopant introduction by ion implantation as well as during operation.

In diamond, the current state of knowledge about self-interstitials is quite different to that in silicon. Although the extended interstitial defect known as the platelet has received much attention from experimentalists [115, 116, 109, 117, 118] the structure, and even composition, of the defect is still the subject of debate. On the other hand, the structures of both the single self-interstitial (I) and a form of the di-interstitial (I_2) have been identified with electron paramagnetic resonance (EPR) centers [119, 120].

10.2 Background

Early theoretical investigations [121] first suggested that I_1 in diamond is a $\langle 001\rangle$ split-interstitial, as shown in Fig. 10.1. All atoms are fully coordinated in this structure apart from the two equivalent central atoms. These atoms each make three bonds, so that they lie co-planar with their neighbours. This sp^2 bonding arrangement also gives rise to p-orbitals on each atom, directed perpendicular to the plane of the bonding orbitals. These degenerate non-bonding orbitals lie along [110] and [1$\bar{1}$0] and were later calculated by Briddon *et al* [122] to be separated by 1.26 Å and to give rise to an half-filled e-doublet in the upper half of the Kohn-Sham eigen-spectrum of I_1. The ground state of the I_1 defect has been calculated to be $S = 0$. It was suggested that the $S = 0$ defect undergoes a weak pseudo–Jahn-Teller distortion, effected by a small twist about [001] [122]. This distortion introduces an element of π-bonding between the p-orbitals and leads to the splitting of the electronic e-level and to a structure with D_2 point group symmetry.

The conclusion that the lowest energy structure for I_1 is of the $\langle 001\rangle$-split form has now been corroborated by experiment. The R2 EPR centre is observed in type IIa diamond following electron, neutron or gamma irradiation [123, 119]. R2 has spin 1 and D_{2d} symmetry. Measurements taken at 80, 200 and 295 K revealed that the observed R2 center does actually corresponds to an excited state as predicted by theory. The energy difference between the paramagnetic and diamagnetic states is found to be just 39 meV [124] substantially smaller than the computed value. R2 is highly stable and disappears only following annealing at around 600 K.

Hyperfine measurements show that there are two equivalent atoms upon which most of the unpaired wavefunction is localized. Since the defect has spin 1, the Hamiltonian fitted to the EPR spectrum contains the term $\mathbf{S} \cdot \mathbf{D} \cdot \mathbf{S}$ taking account of the spin-spin interaction as described in Chapter 3. The application of the point-dipole approximation to the measured D-tensor assumes two things: (i) The tensor arises entirely from the spin-spin dipole interaction (i.e. spin-orbit and other possible components are negligible) and (ii) the unpaired spin orbitals can be assumed to be point-like. Evidently, the latter

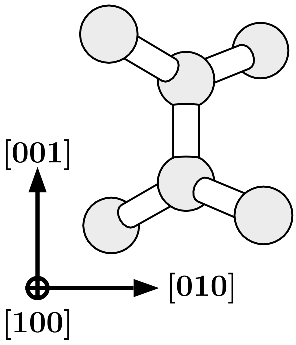

Figure 10.1: The optimised structure of the isolated [001] self-interstitial in diamond.

assumption is quite severe and the former could also be in serious error. Using the point-dipole approximation leads to an inter-radical separation for R2 of 2.5 Å. This is in conflict with the ⟨001⟩-split model because it is a much larger value than the calculated separation (1.27 Å) of the two C-radicals. Using the computed separation to estimate the magnitude of the D-tensor within the point dipole approximation gives D_3 eight times larger than the observed value. Although the point-dipole approximation may be crude, this discrepancy has cast some doubt on the assignment of the R2 center to a single interstitial.

Another EPR centre has been identified with an interstitial defect. The R1 EPR spectrum is formed, along with R2 EPR centre, by room temperature e-irradiation of chemically pure type IIa diamond [123, 125]. The R1 spectrum arises from a spin-one defect having C_{2h} symmetry. The defect has a magnetic signature characterised by one of the principal axes of the electron-electron dipole tensor D making an angle of 17° with [110] and lying in the $(1\bar{1}0)$ plane.

Irradiated type IIa diamonds absorb light strongly at 1.673 eV. This optical center, labelled GR1, is assigned to the neutral vacancy [126]. Other absorption lines at 1.685 and 1.859 eV are correlated with the R2 center and anneal out at 700K [127]. The closeness of these lines to the GR1 band suggested to Lowther and Mainwood [128, 129, 130] that the R1 and R2 centres are perturbed vacancy defects. However, this suggestion has been superseded by subsequent experimental work [125]. These detailed investigations [125] employed type IIa synthetic diamond which was enriched with 5% ^{13}C. The concentrations of the R1 and R2 EPR centers in this diamond are around 10^{16} cm^{-3} and are comparable with the concentration of neutral vacancies as estimated from the intensity of the GR1 optical absorption band. The R1 defect anneals out between 600-700K and before the vacancy begins to migrate (around 900K [93]) suggesting that it is a primitive interstitial

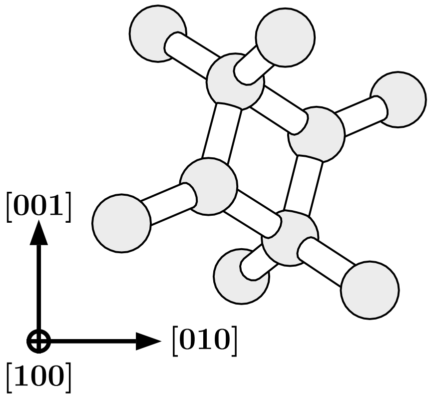

Figure 10.2: The optimised structure of the nearest neighbour form of the di-[001] interstitial in diamond.

defect.

Twitchen *et al.* [125] analysed the EPR transitions when the magnetic field is rotated from [001] in the (110) plane with a spin-Hamiltonian that included the dipole term. The g and D tensors were found by a fit to the data in which the g_1 and D_1 principal values were constrained to lie along $[1\bar{1}0]$. From the mirror symmetry of the defect, one principal axis must lie along this direction. The other principal values and directions of the D tensor are given in Table 10.3. The values, and the fact that this $S = 1$ defect has C_{2h} symmetry suggests that two C radicals inhabit a $(1\bar{1}0)$ plane with their p-orbitals, each containing one electron, pointing along $[1\bar{1}0]$. According to Twitchen *et al*, 70% of the spin-density resides on the C radicals. The R1 defect was proposed to arise from the neutral charge state of a pair of [100] split-interstitials lying at nearest neighbour (NN) positions [125] (see Fig. 10.2).

The D_1 and D_3 principal values for the R1 centre are found to be 1.408 and 1.397 GHz and their near degeneracy suggests that the defect possesses axial symmetry. This can be understood if the spin-density is localised on the radicals and does not overlap neighbouring atoms. This model suggests that a point-dipole model for D would be applicable but using the point-dipole approximation the separation is estimated to be 2.65 Å. This distance is larger than the separation of second shell atoms in the crystal (2.51 Å) and is therefore incompatible with the NN di-interstitial model. One motivation for the study of the electron-electron dipole interaction is to assess the applicability of the point dipole approximation.

One other spin-one defect labelled O3 has been reported recently [131]. During the annealing-out stage of R1 and R2 this centre appears, or its signal is significantly strengthened. Annealing at around 50 K higher results in the disappearance of the centre. O3 is been classified as a monoclinic II centre nd therefore possesses C_2 point group symmetry. The intensity ratios of the hyperfine satellite lines are used to indicate how many sites are involved, and the occupancy values, η^2 are determined.

The formation and character of the extended defects observed in diamond, termed platelets, is now briefly discussed. Platelets lie on an {001} plane. They are observed microscopically in type Ia diamonds following annealing at around $\sim 2000°$C. Much argument has centred on whether the platelet is comprised primarily of self-interstitials or nitrogen atoms [109]. The question has arisen because platelets are formed in the annealing stage of A centres (N_s-N_s). It is known that the A centers migrate, and subsequently form B centres (VN$_4$), ejecting a self-interstitial in the process:

$$\mathrm{N}_2 + \mathrm{N}_2 \rightarrow V\mathrm{N}_4 + I$$

The nitrogen-rich models for the platelet have received support because platelets have not been produced in nitrogen-free diamond, even after irradiation (producing self-interstitials) and high temperature annealing. When such experiments are performed, a random pattern characteristic of the early stages of amorphisation is observed by TEM. This condition is termed 'Black Death' [132].

TEM studies [133] have shown that the platelet leads to a displacement of {100} planes by 0.4 a_0 although displacements as low as 0.33 a_0 have been reported for smaller platelets [134]. Electron energy loss spectroscopy (EELS) studies [118] have demonstrated that the platelets contain between 0.08 and 0.47 monolayers of nitrogen. This finding gives strong evidence that nitrogen is not an essential constituent of the platelet. Infra-red absorption studies [135] show two vibrational modes associated with platelets which lie at 328 and 1358-1373 cm^{-1} (labelled B$'$). No dependence on nitrogen isotopes is observed for B$'$ mode further supporting the nitrogen-free model for the platelet.

Given that the evidence that the platelet is primarily composed of self-interstitial atoms, there are two important questions to answer (i) What is the structure of the platelet? and (ii) What is the formation mechanism? In this chapter the former question is addressed in relation to the structure of small interstitial aggregates.

10.3 Method

Both AIMPRO cluster and supercell methods were used to investigate the isolated self-interstitial and its aggregates. Clusters of composition $C_{98+n}H_{76}$ and $C_{165+n}H_{100}$, where n is the number of interstitial atoms, were employed. The wave-function basis consisted of independent s and p Gaussian orbitals with four different exponents, sited at each C site. A fixed linear combination of two Gaussian orbitals was sited on the terminating H atoms. In addition, a Gaussian s and p orbital was placed at each C–C bond center. The charge density was fitted with four independent Gaussian functions with different widths on each C atom and three on the terminating H atoms. One extra Gaussian function was placed at each C–C bond center. The positions of all bulk atoms were optimized using a conjugate gradient method. The convergence of the defect structures and D-tensors was tested with respect to both cluster size and surface treatment. Relaxation of the terminating hydrogens of the cluster containing the largest defect, I_4 gave rise to shifts of less than 3% in the bond lengths. Similarly, the magnitudes of the D-tensor of I_3 were found to vary by less than 2% with surface relaxation. Increasing the cluster size from $C_{72}H_{60}$ to $C_{185}H_{120}$ resulted in variations in the bond lengths of I_1 of under 1%.

The comparison of first-principles, theoretically derived results with EPR data is usually limited to symmetry and energetics which rarely allows for conclusive identification. In diamond, the first three interstitial defects (labelled I_1 to I_3) have ground or low-lying excited spin-triplet states. Thus they possess an associated spin-spin tensor, D, which uniquely characterizes them. This quantity is evaluated for I_1 to I_3.

The dipole contribution to the spin-spin interaction tensor is given by:

$$D_{ij} = \frac{\mu_0 g^2 \beta_e^2}{8\pi} \int d\mathbf{r}_1\, d\mathbf{r}_2\, \rho(\mathbf{r}_1, \mathbf{r}_2) \left\{ \delta_{ij} - 3\frac{(r_{1i} - r_{2i})(r_{1j} - r_{2j})}{|\mathbf{r}_1 - \mathbf{r}_2|^2} \right\} |\mathbf{r}_1 - \mathbf{r}_2|^{-3}. \tag{10.1}$$

Here β_e is the Bohr magneton, g the electron Landé factor, and ρ is the probability of locating spins at points $\mathbf{r}_1$ and $\mathbf{r}_2$. We shall assume that ρ is determined from the two electrons occupying the two highest spin-up Kohn-Sham orbitals λ, μ. The expression for ρ is then

$$\begin{aligned} \rho(\mathbf{r}_1, \mathbf{r}_2) &= \Psi(\mathbf{r}_1, \mathbf{r}_2)^2 & (10.2) \\ \Psi(\mathbf{r}_1, \mathbf{r}_2) &= \frac{1}{\sqrt{2}} \{\psi_\lambda(\mathbf{r}_1)\psi_\mu(\mathbf{r}_2) - \psi_\lambda(\mathbf{r}_2)\psi_\mu(\mathbf{r}_1)\} & (10.3) \end{aligned}$$

Consider the case, relevant here, that μ and λ are localized on two C radicals with separation $\mathbf{R}$. When R is much larger than the localization length for each orbital, then the exchange term can be ignored and the point dipole expression for D becomes

$$D^a_{ij} = \frac{\mu_o g^2 \beta_e^2}{8\pi} \left\{ \delta_{ij} - 3\frac{R_i R_j}{R^2} \right\} / R^3. \tag{10.4}$$

The matrix D^a has three principal values

$$D^a_1 = D^a_2 = -D^a_3/2 = \frac{\mu_o g^2 \beta_e^2}{8\pi R^3}.$$

The principal direction of D^a_3 is associated with the line joining the radicals. This formula has often been used but seriously overestimates R, as the distributed nature of the spin–density is ignored. Here, we compute the integral in Eq. (10.1) using the wave-functions obtained from AIMPRO. The orbitals $\psi(\mathbf{r})$ were expressed as linear combinations of Gaussian s, p functions and hence the integrals in Eq. (10.1) can be found either analytically or numerically.

10.4 Results

10.4.1 I_1

The structure of I_1^0 is shown in Fig. 10.1. The two core atoms are separated by 1.27 Å compared with 1.42 Å for the C-C bond in graphite.

The Kohn-Sham e-orbitals are substituted into Eq. 10.3 to generate the D-tensor (Eq. 10.1). The principal values and directions of the D-tensor are given in Table 10.3. The magnitudes of the D-tensor elements are within $\sim$ 30% of those of the R2 EPR center [120, 123].

The migration path for I_1 involves the re-orientation of the split-interstitial from [001] to [010]. The barrier to migration of the single-self-interstitial was previously calculated from this to be 1.7 eV [122]. This value is in good agreement with the experimental barrier of 1.6-1.7 eV determined from the loss of vacancies at around 700 K, presumably through interstitial-vacancy recombination [136, 137].

10.4.2 I_2

We now consider the di-interstitial, I_2. Three structures were optimised in both spin $S = 0$ and $S = 1$. The simplest structure is the nearest-neighbour form (NN) where the two split-interstitial pairs form strong bonds. This is the defect identified with the $S = 1$ EPR center labelled R1 [125]. The other structures investigated were the next-nearest-neighbour forms where the split-interstitial pairs either lay parallel ($2NN_{||}$) or

Spin	Structure		
	NN	$2NN_{\|\|}$	$2NN_{\perp}$
0	-0.0010	-0.394	$+0.704$
1	0.0	-0.059	$+0.63$

Table 10.1: Total energies (eV) of di-interstitial defects calculated using the cluster code.

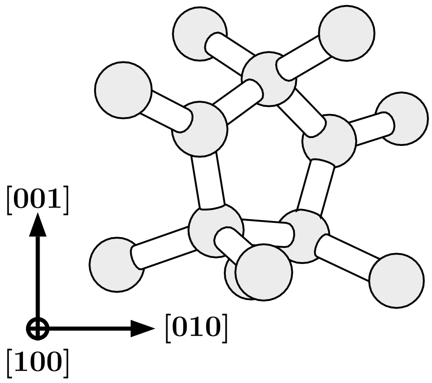

Figure 10.3: The optimised structure of the next-nearest neighbour form of the di-[001] interstitial in diamond.

perpendicular ($2NN_{\perp}$) to each other. The optimised structure for the nearest neighbour di-split interstitial is shown in Fig. 10.2.

The NN split-interstitial, in the absence of symmetry constraints, has C_{2h} symmetry in agreement with experimental symmetry for R1 and the spin $S = 1$ configuration was found to lie 0.2 eV lower in energy than $S = 0$. This defect has an inter-radical separation of 1.7 Å. The calculated principal directions of the D-tensor are in excellent agreement with the measured ones (Table 10.3) and the principal values are in fair agreement.

Placing two single [001] split-interstitials at next-nearest-neighbor ($2NN$) positions results in a structure with C_{2v} symmetry (Fig. 10.3). As for the NN case, a reconstruction of dangling bonds of the two split-interstitials results from this structure giving a defect with two non-bonding p-orbitals. The energy difference between the NN and $2NN$ is negligible for $S = 1$ (see Table 10.1). However, the $S = 0$, $2NN$ structure was calculated to be 0.4 eV lower in energy than the $S = 1$, NN defect. This raises the possibility that, although the NN di-interstitial is observed by EPR, another, more stable, di-interstitial exists in a diamagnetic state.

The migration barrier of the di-interstitial has also been calculated. The diffusion

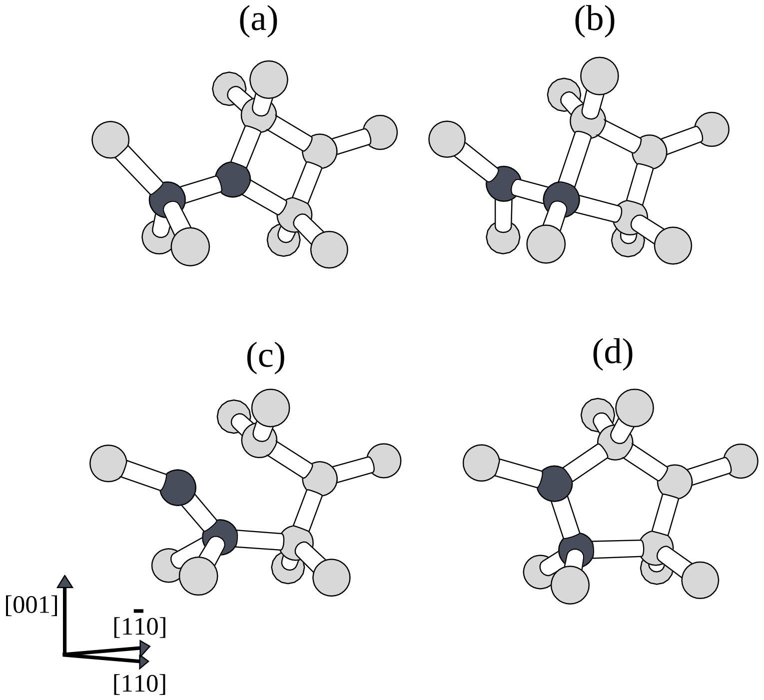

Figure 10.4: Calculated diffusion mechanism for the [001] orientated di-interstitial in diamond. The defect migrates through interconversion between the nearest neighbour structure, (a) and the next nearest neighbour structure (d) via structures (b) and (c). The two atoms which move the most during the diffusion step shown are shaded dark grey to aid the eye.

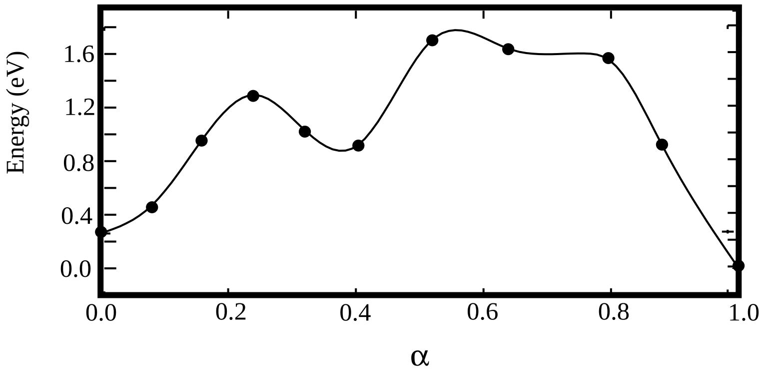

Figure 10.5: Calculated diffusion barrier for the [001] orientated di-interstitial in diamond. $\alpha = 0$ corresponds to Fig. 10.4 (a) and $\alpha = 1.0$ corresponds to Fig. 10.4 (d).

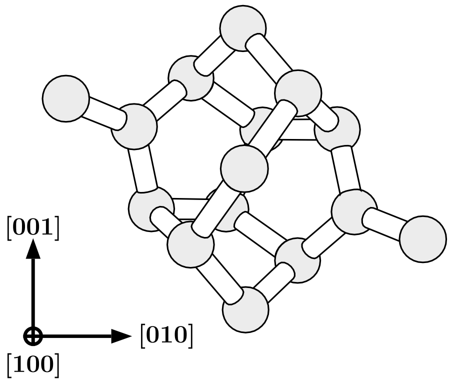

Figure 10.6: The optimised structure of the of the tri-[001] interstitial in diamond.

method allows constrained structural optimization from various transition-state configurations which lie along a vector connecting the initial structure to the final structure. The initial and final structures were chosen to be the NN optimized structure and the $2NN$ optimized structure. The barrier to this process was calculated to be 1.8 eV (see Fig 10.5). Thus the calculated barriers to diffusion of I_1 and I_2 are roughly equal and this results explains why R1 and R2 anneal out at the same temperature, $\sim$ 600 K.

10.4.3 I_3

A tri-interstitial structure was constructed by placing three [001] split-interstitials at next-nearest-neighbor positions as indicated in Fig. 10.6. Structural optimization results in bond reconstruction so that two 3-fold coordinated atoms remain. Thus the number of dangling bonds is reduced by four relative to three isolated interstitials, hence accounting for the defect's stability. The relaxed structure has C_2 symmetry. A unique atom lies

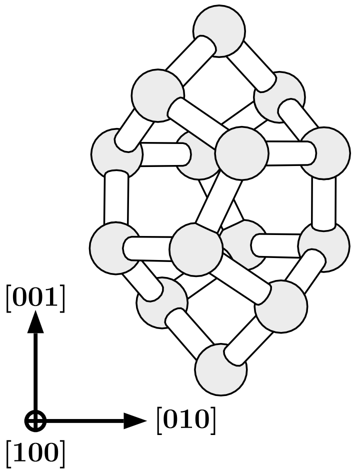

Figure 10.7: The optimised structure of the of the tetra-[001] interstitial in diamond.

between the two radicals. Both the magnitudes of the calculated D-tensor elements are in good agreement (within $\sim$ 15%) with those of the O3 EPR center [131] (Table 10.3) and the directions are in excellent agreement.

10.4.4 I_4

Given the strength of evidence supplied by the calculated parameters, the identification of O3 with the tri-interstitial is conclusive. The existence of a tri-interstitial with this structure provides strong evidence for the structure of the I_4 defect. The addition of one further [001] split-interstitial to I_3 results in the defect shown in Fig. 10.7. This form for I_4 was shown in Chapter 9 to exist in Si. The structure is found to be similar to that calculated in Si with all atoms become four-fold coordinated and furthermore, all bond lengths and angles are close to ideal. The KS eigenvalue structure shows just two singlet states which lie close to the valence band edge. The calculated formation energy per interstitial of the I_4 defect is found to be less than half of that of I_1 demonstrating its remarkable stability.

10.4.5 Trends

The interstitial defects discussed share the common feature of [001] orientation. To clarify the close relation between the structures they are shown in schematic form in Fig. 10.8. One important structural trend is the length of the 'split-interstitial pair bond'. For the single interstitial this length is found to be 1.28 Å. As further interstitials are added,

Structure	[001] bondlength(s)	Inter-radical spacing	Energy per interstitial
I_1	1.28	1.28	12.3
I_2 (NN)	1.33	1.86	9.3
I_2 $(2NN)$	1.32	2.35	9.0
I_3	1.38, 1.33	3.6	7.8
I_4	1.47	–	5.5

Table 10.2: Structural and energetical parameters for self-interstitial aggregates in diamond calculated using the supercell method. Bondlengths are given in Å and energies in eV.

	D_1	D_2	D_3	n_1	n_2	n_3
I_1: Calc.	0.91	0.91	−1.82	$[1\ \bar{1}\ 0]$	[1 1 0]	[0 0 1]
R2: Expt. [138]	±1.39	±1.39	∓2.78	$[1\ \bar{1}\ 0]$	[1 1 0]	[0 0 1]
I_2 NN: Calc.	1.19	0.78	−1.97	$[1\ \bar{1}\ 0]$	[0.21 0.21 0.95]	[0.67 0.67 −0.30]
R1: Expt. [125]	1.41	1.40	−2.81	$[1\ \bar{1}\ 0]$	[0.21 0.21 0.95]	[0.67 0.67 −0.30]
I_3: Calc.	0.40	0.29	−0.69	[1 0 0]	[0.0 0.31 0.95]	[0.0 0.95 −0.31]
O3: Expt. [131]	0.46	0.35	−0.81	[1 0 0]	[0.0 0.31 0.95]	[0.0 0.95 −0.31]

Table 10.3: The calculated and experimental principal values (GHz), in descending order, and principal directions, $[n_1 n_2 n_3]$, for the spin–spin tensor, D. In each case n_3 is almost parallel to the vector joining the radicals.

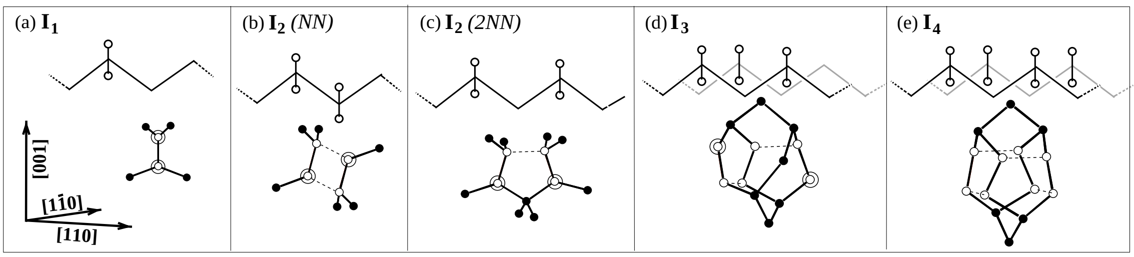

Figure 10.8: (a)–(e) Interstitial aggregates in diamond. NN denotes nearest-neighbour form, $2NN$ denotes next-nearest-neighbor form. Each interstitial center is summarised in two ways. Upper figure : Schematic indicating the positions of the constituent [001]-split-interstitial pairs on a [110] chain of atoms in the diamond lattice (represented by the jagged line). Lower figure: The relaxed structures of each defect. The open circles represent the interstitial atoms shown in the upper figure and the ringed atoms are those which are three-fold coordinated and possess non-bonding orbitals. Reconstructed bonds are shown by dashed lines.

there is a mutual strain relief so that we expect this bond length to increase. The values for all the defects calculated are given in Table 10.2. For I_4 this bondlength has increased to 1.47 Å. The main consequence of this mutual strain relief concomitant with the addition of interstitial atoms is that we expect the maximum local vibrational mode frequencies supported by each defect to decrease as the number of interstitials in the aggregate increases.

Energetically there is another clear trend. Table 10.2 shows the calculated formation energies for all the defects. The chief source of the reduction in formation energy as the number of interstitials increases is the reduction in the number of dangling bonds per interstitial. Calculating the binding energy of each I_n aggregate relative to n isolated interstitials shows that between 2.5-4.5 eV is saved through the saving of each dangling bond.

The electronic structures of the defects I_1 to I_3 are very similar. Each defect possesses just two p-orbitals which each give rise to a state above mid-gap. The splitting of the two sates depends upon the interaction between the electronic orbitals but is less than 1.0 eV in each case. It is the presence of these two states close in energy which enable the spin 1 states of the defects to be observed by EPR. In the case of I_4 there are no mid-gap states as the defect is fully coordinated.

10.4.6 Platelets

The structure of I_4 suggests a link with the platelet. There have been many models proposed for the platelet extending over more than 40 years [118, 109, 139], but the most recent favor a condensation of carbon interstitials onto a {001} plane [118]. As all bonds are saturated, an array of I_4 units, as suggested by Humble [109], and shown schematically in Fig. 10.9(Squares), is expected to have particularly low energy. However, it is possible to switch the bond reconstruction from one I_4 unit to a neighboring one with the requirement that each reconstructed bond lies perpendicular to its neighboring reconstructed bonds. Thus one of the reconstructed bonds in Fig. 10.7 is broken and the atoms with dangling bonds form bonds with neighboring I_4 units. This leads to a plethora of possible models, the most simple of which are shown in Fig. 10.9.

Recent transmission electron microscopy (TEM) studies [118] show that the [110] and $[1\bar{1}0]$ projections are inequivalent. This property is shared by just three of the reconstructions shown; the ‘staggered squares’ and the ‘[110] chain’ models. Recent calculations using supercell AIMPRO [140] show that the ‘staggered squares’ model is the lowest energy model, although in practise it is likely that a combination of all the topologies might occur [118].

10.4.7 Conclusions

In summary, the *ab initio* modeling and the evaluation of the spin-spin dipole tensor has confirmed models for I_1 and I_2. For these defects the calculated magnitude of the dipole-dipole interaction underestimates the observed D-tensor values by up to 30%. It is likely that the underestimate results from the omission of spin-orbit interaction in the calculation. Despite this, the calculated directions of the tensor for I_2 (NN) are in excellent agreement with experiment (for I_1 the directions are necessarily correct as they are constrained by symmetry along the cubic axes). The calculated diffusion barrier of 1.8 eV supports the identification of I_2 with R1 nd explains the similar annealing temperature of R2 and R1.

The calculated symmetry and structure of I_3 is in good agreement with the EPR data. Conclusive proof of the identification of I_3 with the O3 EPR centre is however provided by the D-tensor calculation. In this case the magnitudes are within $\sim 15\%$ of experiment and the directions are in excellent agreement. The assignment of the O3 EPR center to I_3, a precursor to I_4, is then particularly valuable as it has given us a glimpse of the

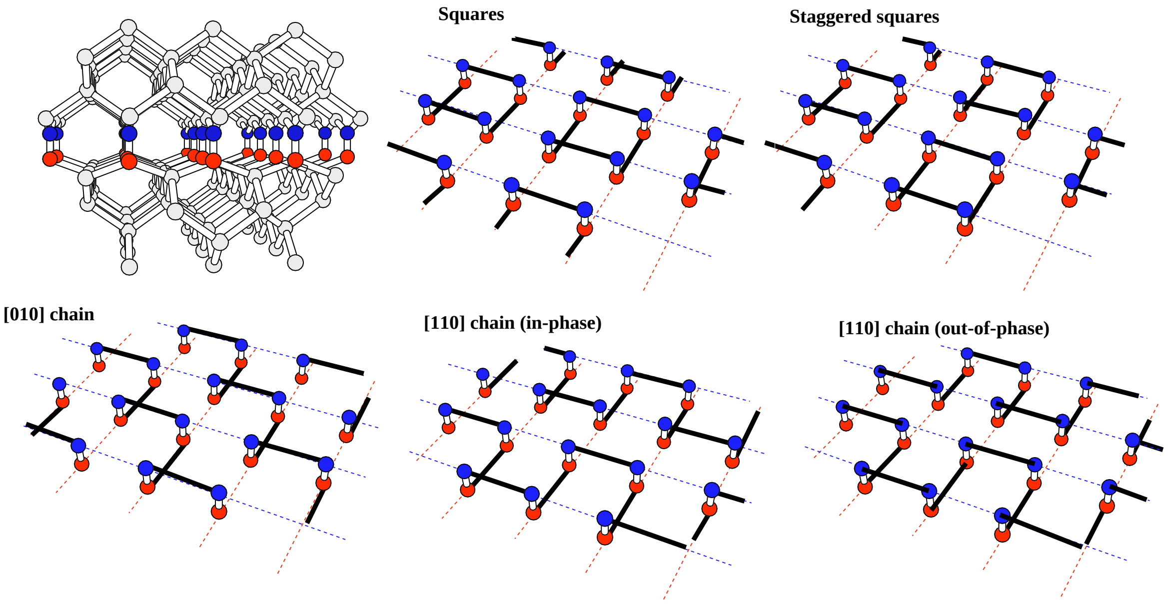

Squares

Staggered squares

[010] chain

[110] chain (in-phase)

[110] chain (out-of-phase)

Figure 10.9: Pure self-interstitial platelet models. Replacing every atom on a {001} plane by a [001] split-interstitial pair (top left), there are a number of ways of producing a fully reconstructed platelet. Five different simple reconstructions are depicted. IN each case the surrounding lattice has been removed for clarity. Each atom is colored depending on whether it lies in the upper or lower plane to aid the eye.

pathway leading to aggregation of self-interstitial defects resulting in the formation of the platelet in diamond.

Chapter 11

Conclusions

In this chapter the main conclusions of this thesis are discussed. Areas where possible weaknesses lie and topics for further investigation are considered.

In Chapter 5 the properties of vacancy-hydrogen defects in germanium were investigated using the cluster version of AIMPRO. Th vibrational properties were found to be in reasonable agreement with the experimental values and the symmetry lowering distortions, where applicable, were accounted for.

Chapters 6–9 contain an investigation into the self-interstitial defects in silicon, I_1 to I_4. The main conclusions of Chapter 6 were (i) the electronic structure and 'over-coordinated' bonding of the $\langle 110\rangle$ self-interstitial can be explained simply through an LCAO picture (ii) the $\langle 110\rangle$ can undergo extremely rapid reorientation and (iii) the properties of the charged self-interstitial at the tetrahedral site were calculated to generally support the assignments of the E1 and AA12 spectra to this defect although the identification is far from conclusive. One possible area for further theoretical work would be to probe the nature of the Jahn-Teller distortion of the self-interstitial from the T_d site in the positive charge state.

In Chapter 7 the properties of di-interstitials were calculated and compared with the experimental data on the P6 EPR center. One important conclusion is that the previous proposal of a C_{1h} structure cannot be fully correct. Three models were considered, and there properties fully investigated. One defect was found to possess the correct electron localisation and symmetry to explain the P6 centre but questions remain concerning energetics and electronic levels.

Consideration of the tri-interstitial in Chapter 8 covered four defect structures. Two of these were resultant from molecular dynamics calculations and were found to have closely related geometrical, electrical and vibrational characters. A model with C_2 symmetry was studied resulting in its exclusion as a candidate for the P6 EPR centre. A trigonal, fully reconstructed model was considered as a model for the W-optical centre observed in irradiated and annealed Si. The conclusion was drawn that this defect structure constitutes a good model for the W-centre. Further experimental work is required to fully establish the formation mechanism of this defect.

In Chapter 9 a structural model for I_4 was proposed to explain the B3 EPR centre. The structure, symmetry, electrical character and B-tensor were all found to support the assignment. It is as yet unclear, however, if the DLTS level at $E_v + 0.29$ eV, vibrational modes observed just above the Raman edge, or the X optical centre can also be attributed to this defect.

The final chapter contains the results of a number of calculations on self-interstitials in diamond. Calculations of the dipole-dipole tensor for the spin-one centres gives strong corroboration for the assignments of I_1 and I_2 to the R2 and R1 EPR centres respectively. Moreover this calculation allows conclusive identification of I_3 with the O3 EPR centre. The structure of I_3 in diamond provides gives very strong indirect evidence that the structure of I_4 is the same as that in silicon. This latter statement has consequences for the models considered for platelets in diamond and these are discussed.

In conclusion, the properties of several defects in all three elemental semiconductors have been investigated. All the calculations presented in this thesis, where possible, have been performed in close collaboration or contact with experimental groups. The strongest results of this thesis relate to the nature of the self-interstitial – a curiously elusive beast – and the identification of I_4 in silicon.

Bibliography

[1] R. B. Capaz, J. A Dal Pino, and J. D. Joannopoulos, Phys. Rev. B **50**, 7439 (1994).

[2] P. W. Leary, Ph.D. thesis, Physics, University of Exeter, 1997.

[3] A. Mainwood, Mater. Sci. Forum **196-201**, 1589 (1995).

[4] Y. H. Lee, Appl. Phys. Lett. **73**, 1119 (1998).

[5] M. Kohyama and S. Takeda, Phys. Rev. B **60**, 8075 (1999).

[6] Y.-H. Lee, N. N. Gerasimenko, and J. W. Corbett, Phys. Rev. B **14**, 4506 (1976).

[7] J. Kim *et al.*, Phys. Rev. Lett. **83**, 1990 (1999).

[8] G. D. Watkins and J. W. Corbett, Phys. Rev. **138**, A543 (1965).

[9] L. Colombo, Physica B **273**, 458 (1999).

[10] S. K. Estreicher, J. L. Hastings, and P. A. Fedders, in *Materials Science Forum* (Trans Tech Publications, Switzerland, in press).

[11] G. D. Watkins and J. W. Corbett, Phys. Rev. **138**, A543 (1965).

[12] B. Hourahine *et al.*, Phys. Rev. B **61**, 12594 (2000).

[13] D. M. Ceperley and B. J. Alder, Phys. Rev. Lett. **45**, 566 (1980).

[14] J. C. Slater, Adv. Quantum Chem. **6**, 1 (1972).

[15] D. Vanderbilt, Phys. Rev. B **41**, 7892 (1990).

[16] G. B. Bachelet, D. R. Hamman, and M. Sclüter, Phys. Rev. B **26**, 4199 (1982).

[17] F. H. Stillinger and T. A. Weber, Phys. Rev. B **31**, 5262 (1985).

[18] G. M. S. Lister and R. Jones, 1995 (unpublished).

[19] H. J. Monkhorst and J. D. Pack, Phys. Rev. B **13**, (1976).

[20] J. P. Perdew and Y. Wang, Phys. Rev. B **45**, 13244 (1992).

[21] J. P. Perdew and A. Zunger, Phys. Rev. B **23**, 548 (1981).

[22] S. Ögut, H. Kim, and J. R. Chelikowsky, Phys. Rev. B **56**, R11353 (1997).

[23] A. Resende, Ph.D. thesis, University of Exeter, 1999.

[24] M. Saito and A. Oshiyama, Phys. Rev. Lett. **73**, 866 (1994).

[25] A. A. Kaplyanski, Opt. Spectrosc. **16**, 329 (1964).

[26] R. C. Newman and J. B. Willis, J. Phys. and Chem. Solids **26**, 373 (1965).

[27] R. C. Newman and J. B. Willis, J. Phys. and Chem. Solids **30**, 1943 (1969).

[28] A. R. Bean and R. C. Newmann, ssc **8**, 175 (19870).

[29] G. D. Watkins and K. L. Brower, Phys. Rev. Lett. **36**, 1329 (1976).

[30] L. C. Kimerling, P. Blood, and W. M. Gibson, in *DRES*, *46*, IOP, edited by J. H. Albany (IOP, London, 1979), p. 273.

[31] L. W. Song and G. D. Watkins, Phys. Rev. Lett. **42**, 5759 (1990).

[32] R. Wooley, E. C. Lightowlers, A. K. Tipping, and M. C. abd R C Newman, Mat. Sci. Forum **10-12**, 929 (1986).

[33] K. Thonke, A. Teschner, and R. Sauer, Solid State Commun. **61**, 241 (1987).

[34] J. F. Zheng, M. Stavola, and G. D. Watkins, in *The Physics of Semiconductors*, edited by D. J. Lockwood (World Scientific, Singapore, 1994), Chap. 5, p. 2363.

[35] R. Jones and P. R. Briddon, in *Identification of defects in semiconductors*, Vol. 51A of *Semiconductors and semimetals*, edited by M. Stavola (Academic press, Boston, 1998), Chap. 6.

[36] J. P. Coutinho, private communication (unpublished).

[37] M. J. P. Musgrave and J. A. Pople, Proc. Roy. Soc. **1268**, 474 (1962).

[38] R. Newman and R. Jones, in *Oxygen in Silicon*, *Semiconductors and Semimetals*, edited by F. Shimura (Academic Press, Boston, 1993), Chap. VI – Diffusion of Oxygen in Silicon.

[39] J. Coutinho, R. Jones, P. R. Briddon, and S. Öberg, Phys. Rev. B accepted for publication (2000).

[40] A. Resende, R. Jones, S. Öberg, and P. R. Briddon, Phys. Rev. Lett. (1999).

[41] C. B. Collins, R. D. Carlson, and C. J. Gallagher, Phys. Rev. **105**, 1168 (1957).

[42] A. F. Tasch and C. T. Sah, Phys. Rev. B **1**, 800 (1970).

[43] A. Mesli, E. Courcelle, T. Zundel, and P. Siffert, Phys. Rev. B **36**, 8049 (1987).

[44] S. J. Pearton, J. W. Corbett, and T. S. Shi, Appl. Phys. A **43**, 153 (1987).

[45] C. T. Sah, Y. C. Sun, and J. T. Tzou, Appl. Phys. Lett. **43**, 204 (1983).

[46] J. I. Pankove, D. E. Carlson, J. E. Berkeyheiser, and R. O. Wance, Phys. Rev. Lett. **54**, 2224 (1983).

[47] E. E. Haller, in *Hydrogen in Semiconductors, Semiconductors and Semimetals*, edited by J. I. Pankove and N. M. Johnson (Academic Press, San Diego, 1991), Vol. 34, Chap. 11.

[48] M. A. Roberson and S. K. Estreicher, Phys. Rev. B **49**, 17040 (1994).

[49] C. G. V. der Walle, Phys. Rev. B **49**, 4579 (1994).

[50] B. B. Nielsen, L. Hoffman, and M. Budde, Mat. Sci. & Eng. B **36**, 259 (1996).

[51] W. M. Chen, O. O. Awadelkarim, and B. Monemar, Phys. Rev. Lett. **64**, 3042 (1990).

[52] B. B. Nielsen, P. Johannesen, P. Stallinga, and K. B. Nielsen, Phys. Rev. Lett. **79**, 1507 (1997).

[53] P. Stallinga *et al.*, Phys. Rev. B **58**, 3842 (1998).

[54] L. M. Xie, M. W. Qi, and J. M. Chen, J. Phys.: Condens. Matter **3**, 8519 (1991).

[55] M. Budde *et al.*, Phys. Rev. B **54**, 5485 (1996).

[56] M. Budde, Ph.D. thesis, Aarhus Center for Atomic Physics, University of Aarhus, Denmark, 1998.

[57] B. B. Nielsen *et al.*, in *Defects in Semiconductors 18*, edited by M. Suezawa and H. Katyama-Yoshida (Trans Tech, Aedermannsdork, 1995), Vol. 196-201, p. 933.

[58] B. B. Nielsen, L. Hoffman, and M. Budde, Mat. Sci. & Eng. B **36**, 259 (1996).

[59] S. Herstrom, Ph.D. thesis, Aarhus center for Atomic Physics, University of AArhus, 1998.

[60] S. Herstrøm, Master's thesis, Institute of Physics and Astronomy, University of Aarhus, 1998.

[61] A. N. Nazarov, V. M. Pinchuk, and T. V. Yanchuk, Modell. Simul. Mater. Sci. Eng. **4**, 323 (1996).

[62] H. Xu, Phys. Rev. B **46**, 1403 (1992).

[63] Y. K. Park, S. K. Estreicher, and C. W. Myles, Phys. Rev. B **52**, 1718 (1995).

[64] B. B. Nielsen *et al.*, in *Materials Science Forum* (Trans Tech Publications, Switzerland, 1995), Vol. 196–201, pp. 933–938.

[65] *Handbook of Chemistry and Physics*, 73 ed. (CRC Press Inc., Boca Raton, 1992).

[66] C. Kittel, *Introduction to Solid State Physics* (Wiley, New York, 1986).

[67] B. J. Coomer *et al.*, Mater. Sci. Engr. B **58**, 36 (1999).

[68] R. Jones, J. Goss, C. Ewels, and S. Öberg, Phys. Rev. B **50**, 8378 (1994).

[69] H. H. Woodbury and W. W. Tyler, Physical Review **105**, 84 (1957).

[70] M. M. D. Souza, C. K. Ngw, M. Shishkin, and E. M. S. Narayanan, Phys. Rev. Lett. **83**, 1799 (1999).

[71] D. J. Chadi, Phys. Rev. B **53**, (1992).

[72] C. G. V. de Walle and J. Neugenbauer, Phys. Rev. B **52**, (1995).

[73] S. J. Clark and G. J. Ackland, Phys. Rev. B **56**, 47 (1997).

[74] B. N. Mukashev, K. A. Abdullin, Y. V. Gorelkinski, and S. Z. Tokmoldin, Mat. Sci. & Eng. B **58**, 171 (1999).

[75] J. L. Mozos and R. M. Nieminen, 1999 (unpublished).

[76] B. N. Mukashev, A. V. Spitsyn, N. Fukuoka, and H. Saito, Jpn. J. Appl. Phys. **21**, 399 (1982).

[77] G. D. Watkins, in *Radiation damage in semiconductors*, edited by DUNOD (Academic, New York, 1965).

[78] A. B. V. Oosten and C. A. J. Ammerlaan, Phys. Rev. B **38**, 13291 (1988).

[79] Y.-H. Lee and J. W. Corbett, Phys. Rev. B **8**, 2810 (1973).

[80] M. Reiche, Phys. Stat. Sol. **138**, 409 (1993).

[81] P. M. Fahey, P. B. Griddin, and J. D. Plummer, Rev. Mod. Phys. **61**, 289 (1989).

[82] Y.-H. Lee and J. W. Corbett, **15**, 1781 (1974).

[83] Y.-H. Lee, Y. M. Kim, and J. W. Corbett, Radiat. Eff. **15**, 77 (1972).

[84] K. L. Brower, Phys. Rev. B **14**, 872 (1976).

[85] P. Stallinga, T. Gregorkiewicz, and C. A. J. Ammerlaan, **90**, 401 (1994).

[86] B. J. Coomer *et al.*, Physica B **274**, 505 (1999).

[87] J. Kim, J. W. Wilkins, F. S. Khan, and A. Canning, Phys. Rev. B **55**, 16186 (1997).

[88] B. J. Coomer *et al.*, submitted to Semic. Sci. Tech. (2000).

[89] Y.-H. Lee, , and J. W. Corbett, Phys. Rev. B **13**, 2653 (1976).

[90] Y.-H. Lee, Appl. Phys. Lett. **73**, 1119 (1998).

[91] N. Pinho *et al.*, ENDEASD conference proceedings (2000).

[92] C. G. Kirkpatrick, D. R. Myers, and B. G. Streetman, Radiation. Eff. **31**, 175 (1977).

[93] G. Davies, E. C. Lightowlers, and Z. E. Ciechanowskia, J. Phys. C:Solid State Phys. **20**, 191 (1987).

[94] H. Feick and E. R. Weber, Physica B **273**, 497 (1999).

[95] J. Weber, Physica B **170**, 201 (1991).

[96] S. K. Estreicher, J. Weber, A. Derecskei-Kovacs, and D. S. Marynick, Phys. Rev. B **55**, 5037 (1997).

[97] V. D. Tkachev, A. V. Mudryi, and N. S. Minaev, Phys. Stat. Solidi A **81**, 313 (1984).

[98] O. O. Awadelkarim, H. Weyman, B. G. Svenson, and J. L. Lindström, J. Appl. Phys. **60**, 1974 (1986).

[99] L. C. Kimerling, in *Radiation Effects in Semiconductors*, edited by N. B. Urli and J. W. Corbett (Institute of Physics, Bristol, 1977), No. 31, p. 221.

[100] A. O. Evwaraye and E. Sun, J. Appl. Phys. **47**, 3776 (1976).

[101] A. Bongiorno *et al.*, ICPS-21 conference proceedings, 1998.

[102] N. Aria and S. Takeda, Phys. Rev. Lett. **78**, 4265 (1997).

[103] M. Gharaibeh, S. K. Estreicher, P. A. Fedders, and P. Ordejon, Phys. Rev. Lett. (2000).

[104] M. Nakamura, S. Nagia, Y. Aoki, and H. Naramoto, Appl. Phys. Lett. **72**, 1347 (1998).

[105] N. E. B. Cowern, G. Mannino, P. A. Stolk, and F. Roozeboom, Phys. Rev. Lett. **82**, 1990 (1999).

[106] S. Coffa, S. Libertino, and C. Spinella, Appl. Phys. Lett. **76**, 321 (2000).

[107] J. L. Benton *et al.*, J. Appl. Phys. **82**, 120 (1997).

[108] D. F. Daly, J. Appl. Phys. **42**, (1971).

[109] P. Humble, Proc. R. Soc. Lond. A **381**, 65 (1982).

[110] N. Aria, S. Takeda, and M. Kohyama, Phys. Rev. Lett. **78**, 4265 (1997).

[111] Z. Ciechanowska and G. Davies, Solid State Comm. **49**, 427 (1984).

[112] O. O. Awadelkarim, Phys. Rev. B **42**, 5635 (1990).

[113] K. Terashima, T. Ikarashi, M. Watanabe, and T. Kitano, Mat. Sci. For. **258-263**, 587 (1997).

[114] R. C. Newman and D. H. J. Totterdell, J. Phys. C: Solid State Phys. **8**, 3944 (1975).

[115] F. C. Frank, Proc. R. Soc. Lond. A **237**, 168 (1956).

[116] T. Evans and C. Phaal, Proc. R. Soc. Lond. A **270**, 538 (1962).

[117] J. C. Barry, Phil. Mag. A **64**, 111 (1991).

[118] P. J. Fallon and L. M. Brown, Phil. Mag. A **64**, 21 (1995).

[119] D. C. Hunt *et al.*, Phys. Rev. B **61**, 3863 (2000).

[120] D. J. Twitchen *et al.*, Physica B **in press**, (1999).

[121] A. Mainwood, F. P. Larkins, and A. M. Stoneham, Solid-State Electronics (1978).

[122] S. J. Breuer and P. R. Briddon, Phys. Rev. B **51**, 6984 (1995).

[123] E. A. Faulkner and J. N. Lomer, Phil. Mag. B **7**, 1995 (1962).

[124] J. Owen, in *Physical properties of Diamond*, edited by B. Berman (Oxford University Press, Oxford, 1965), Chap. 10, p. 274.

[125] D. J. Twitchen *et al.*, Phys. Rev. B **54**, 6988 (1996).

[126] G. Davies *et al.*, Phys. Rev. B **46**, 13157 (1992).

[127] J. Walker, J. Phys. C:Solid State Phys. **10**, 3867 (1977).

[128] J. E. Lowther, Phys. Rev. B **48**, 11592 (1993).

[129] A. Mainwood, J. E. Lowther, and J. A. V. Wyk, J. Phys. C: Condens. Matter **5**, 7929 (1993).

[130] J. E. Lowther and A. Mainwood, J. Phys. C: Condens. Matter (1994).

[131] D. C. Hunt, D. J. Twitchen, M. E. Newton, and J. M. Baker (unpublished).

[132] L. M. Brown, Diamond under the electron microscope, Diamond conference proceedings, 2000.

[133] D. Cherns, K. Kaneko, A. Hovsepian, and A. Lang, Phil. Mag.A **75**, 1553 (1997).

[134] J. C. Barry, L. A. Bursill, and J. L. Hutchison, Phil. Mag. A **41**, 15 (1985).

[135] G. S. Woods, Phil. Mag. B **67**, 651 (1993).

[136] D. W. Palmer, Ph.D. thesis, University of Reading, 1961.

[137] L. Allers, A. S. Howard, J. F. Hassard, and A. Mainwood, Diamond Relat. Matt. **6**, 353A (1997).

[138] M. E. Newton, Chapter 5.2 in *Properties and Growth of Diamond* edited by G Davies, INSPEC, 1994.

[139] A. R. Lang, Proc. Phys. Soc. **84**, 871 (1964).

[140] J. P. Goss *et al.*, Models for platelets in diamond, The 51st Diamond conference proceedings, 2000.